

Enhanced Detection of Small Targets in Ocean Clutter for High Frequency Surface Wave Radar

by

Xiaoli Lu

B.S., Anhui Normal University, 1997

MA.Sc., University of Victoria, 2002

A Dissertation Submitted in Partial Fulfillment
of the Requirements for the Degree of

Doctor of Philosophy

in the Department of Electrical and Computer Engineering

© Xiaoli Lu, 2009
University of Victoria

All rights reserved. This thesis may not be reproduced in whole or in part, by photocopy or other means, without the permission of the author.

Supervisory Committee

Enhanced Detection of Small Targets in Ocean Clutter for High Frequency Surface Wave Radar

by

Xiaoli Lu

B.S., Anhui Normal University, 1997

MA.Sc., University of Victoria, 2002

Supervisory Committee

Dr. R. L. Kirlin, (Department of Electrical and Computer Engineering)
Co-Supervisor

Dr. A. Zielinski, (Department of Electrical and Computer Engineering)
Co-Supervisor

Dr. P. Agathoklis, (Department of Electrical and Computer Engineering)
Departmental Member

Dr. J. Zhou, (Department of Mathematics and Statistics)
Outside Member

Supervisory Committee

Dr. R. L. Kirlin, (Department of Electrical and Computer Engineering)
Co-Supervisor

Dr. A. Zielinski, (Department of Electrical and Computer Engineering)
Co-Supervisor

Dr. P. Agathoklis, (Department of Electrical and Computer Engineering)
Departmental Member

Dr. J. Zhou, (Department of Mathematics and Statistics)
Outside Member

Abstract

The small target detection in High Frequency Surface Wave Radar is limited by the presence of various clutter and interference. Several novel signal processing techniques are developed to improve the system detection performance.

As an external interference due to local lightning, impulsive noise increases the broadband noise level and then precludes the targets from detection. A new excision approach is proposed with modified linear predictions as the reconstruction solution. The system performance is further improved by de-noising the estimated covariance matrix through signal property mapping method.

The existence of non-stationary sea clutter and ionospheric clutter can result in excessive false alarm rate through the high sidelobe level in adaptive beamforming. The

optimum threshold discrete quadratic inequality constraints method is proposed to guarantee the sidelobe-controlling problem consistently feasible and optimal. This constrained optimization problem can be formulated into a second order cone problem with efficient mathematical solution. Both simulation and experimental results validate the improved performance and feasibility of our method.

Based on the special noise characteristics of High Frequency radar, an adaptive switching Constant False Alarm Rate detector is proposed for targets detection in the beamformed range-Doppler map. The switching rule and adaptive footprint are applied to provide the optimum background noise estimation. For this new method about 14% probability of detection improvement has been verified by experimental data, and meanwhile the false alarm rate is reduced significantly compared to the original CFAR.

The conventional Doppler processing has difficulty to recognize a target if its frequency is close to a Bragg line. One detector is proposed to solve this co-located co-channel resolvability problem under the assumption that target/clutter have different phase modulation. Moreover with the pre-whitening processing, the Reversible Jump Markov Chain Monte Carlo method can provide target number and Direction-of-Arrival estimation with lower detection threshold compared to beamforming and subspace methods. RJMCMC is able to convergent to the optimal resolution for a data set that is small compared with information theoretic criteria.

Table of Content

Supervisory Committee	ii
Abstract.....	iii
Table of Content.....	v
List of Tables	ix
List of Figures.....	x
Acronyms	xii
Acknowledgments	xiv
Dedication	xv
Chapter 1 - Introduction and Thesis Outline.....	1
1.1 Introduction.....	1
1.2 Outline and Contents.....	5
1.3 Main Contributions	7
Chapter 2 - Impulsive Noise Excision	10
2.1 Introduction.....	10
2.2 Linear Prediction and Its Modifications	14
2.2.1 Basic Principle	14
2.2.2 Forward-Backward Linear Prediction.....	15
2.2.3 Block Linear Prediction	16
2.2.4 Excision Algorithm.....	18
2.2.5 Experimental Results	19
2.3 Performance Analysis	23
2.4 Further Interpolation and Improvement.....	32

2.4.1 Signal Enhancement.....	32
2.4.2 Theoretical Extension	36
2.5 Section Conclusion	40
Chapter 3 - Sidelobe Control in Adaptive Beamforming.....	42
3.1 Introduction.....	42
3.2 Array Signal Model and Adaptive Beamforming	44
3.2.1 Array Snapshot Model	45
3.2.2 Conventional Adaptive Beamforming (MVDR)	46
3.3 Sidelobe Control in Adaptive Beamforming	48
3.3.1 Diagonal Loading.....	48
3.3.2 Penalty Function Method.....	50
3.3.3 MVDR with Quadratic Inequality Constraints	52
3.3.4 Optimum Threshold for PT-DQC.....	53
3.4 SOC and Unification of Sidelobe Control Methods	55
3.4.1 SOC Formulation of PT-DQC	56
3.4.2 SOC Formulation of OT-DQC.....	56
3.4.3 SOC Formulation of Diagonal Loading.....	57
3.4.4 SOC Formulation of PF Methods	57
3.5 Simulations and Experiments	58
3.6 Summary	63
Chapter 4 - Constant False Alarm Rate Detectors	65
4.1 Introduction.....	65
4.2 State of the Art.....	67

4.2.1 CA-CFAR and Its Variants	69
4.2.2 Ordered Statistics CFAR.....	72
4.2.3 Clutter Map CFAR.....	74
4.3 Hybrid CFAR Algorithm for HF Radar.....	77
4.3.1 Range-Doppler Map Analysis.....	77
4.3.2 Adaptive Switching CFAR	79
4.4 Performance Analysis	86
4.4.1 Homogeneous Background.....	86
4.4.2 Non-homogeneous Background.....	89
4.5 Experiments	91
4.6 Summary	97
Chapter 5 - Bayesian Methods for Target Detection.....	99
5.1 Sea Clutter Model Analysis	101
5.1.1 Microwave Radar Sea Clutter Models Review.....	101
5.1.2 HF Radar Sea Clutter Models Review.....	103
5.2 Signal Detection Based on Phase Tracking	108
5.2.1 Signal Model and Formulation	108
5.2.2 Simulation.....	111
5.2.3 Summary	115
5.3 Pre-whitened RJMCMC for DOA Estimation.....	115
5.3.1 GSC-extended Pre-whitening	116
5.3.2 Reversible Jump MCMC	119
5.3.3 Simulation and Experiments	121

5.3.4 Discussion and Summary.....	125
5.4 Particle Filter.....	125
5.4.1 Basic Principle of the Particle Filter	126
5.4.2 Target Detection in White Noise	128
5.4.3 Further Discussion	137
Chapter 6 – Conclusions and Future Research.....	139
6.1 Summary	139
6.2 Suggestion for Future Work.....	141
Bibliography	143

List of Tables

Table 4-1 The duration and position of all tracks for OS-CFAR and AS-CFAR.....	97
Table 5-1 The Mean Squared Error of the estimated DOA versus SNR for RJMCMC.	124

List of Figures

Figure 1-1 Block diagram for Signal Processing in HFSWR radar system.....	5
Figure 2-1 The range-pulse map for one CIT without impulsive noise.....	11
Figure 2-2 The range-pulse map for the next CIT with impulsive noise.....	11
Figure 2-3 Forward and Backward Weight Function	16
Figure 2-4 The range-Doppler map for the original data with impulsive noise.....	21
Figure 2-5 The range-Doppler map by blanking the impulsive noise	21
Figure 2-6 The range-Doppler map using the forward-backward linear prediction	22
Figure 2-7 The range-Doppler map using the block linear prediction.....	22
Figure 2-8 The amplitude of one CIT record with impulsive noise at range=42 km.....	23
Figure 2-9 Normalized Minimum Variance of three linear predictions	30
Figure 2-10 Normalized Minimum Variance of three linear predictions	31
Figure 2-11 Normalized Minimum Variance of three linear predictions	31
Figure 2-12 The signal enhancements performance comparison for forward linear	35
Figure 3-1 Beampatterns before and after diagonal loading; DLF means diagonal loading factor or value δ ; the sole desired signal is at 0° ; the sole interference is at 54°	50
Figure 3-2 Performance comparison among different PF methods; dashed trace: soft constrained PF; dash-dot trace: original PF; dotted trace: quiescent beampattern	52
Figure 3-3 (a) Beampatterns of PT-DQC for sidelobes less than -30 dB and -40 dB; (b) Beampatterns of OT-DQC for α equal to 15, 40 and 100.....	54
Figure 3-4 SINR and the optimal threshold ε^2 variation versus the weight α	59
Figure 3-5 The beampattern of the sidelobe control algorithms, 32 snapshots; (a) Diagonal loading ; (b) PF with weighting factor $\mu = 15$; (c) PT-DQC with $\varepsilon^2 = 0.001$, (d) OT-DQC with weighting factor $\alpha = 15$	61
Figure 3-6 The output average SINR (300 trials) vs. number of snapshots.....	62
Figure 3-7 The beampattern of the sidelobe control algorithms.	63
Figure 4-1 Illustration of the Neyman-Pearson rule. Blue trace (PDF of noise only); green trace (PDF of target + noise); red line (threshold).	69
Figure 4-2 The Block Diagram of Excision CFAR detector.....	71
Figure 4-3 Block diagram for MOS-CFAR detector	73
Figure 4-4 Block diagram of the CML-CFAR detector.....	74

Figure 4-5 Block diagram of scan by scan averaging CFAR.....	75
Figure 4-6 Block diagram for PDF transformed CM-CFAR	76
Figure 4-7 Sampled range-Doppler map from HF radar.....	78
Figure 4-8 The standard deviation variation of range-Doppler map.....	83
Figure 4-9 The division solution from BIC (blue means only one class and the red means more than one classes).....	83
Figure 4-10 Block diagram of adaptive switching CFAR detector.....	86
Figure 4-11 The detection probability of CA- and OS-CFAR vs SNR	89
Figure 4-12 Tracking results for Teleost.....	92
Figure 4-13 Spectrum of Teleost near the ionospheric clutter	93
Figure 4-14 Tracking results after OS-CFAR detection	94
Figure 4-15 Tracking results after AS-CFAR detection	94
Figure 4-16 Power spectrum of the target near the ionospheric clutter	95
Figure 4-17 Tracking results after OS-CFAR detection	96
Figure 4-18 Tracking results after AS-CFAR detection	96
Figure 5-1 Measured HF radar sea clutter at 3.1 MHz transmitted carrier frequency. The zero Doppler frequency position corresponds to the carrier frequency. Bragg lines show at frequencies ± 0.18 Hz.	105
Figure 5-2 Doppler frequencies vs. time; means are [-0.1787 -0.0137 0.0795 0.1814 0.2879] Hz.	107
Figure 5-3 Doppler spectrum after suppressing the first order Bragg lines.....	107
Figure 5-4 Phase modulation tracking; dashed traces represent estimation, and solid traces represent actual phase.....	112
Figure 5-5 Amplitude tracking; true amplitude is 0.9 for each signal.	113
Figure 5-6 Phase modulation tracking; dashed traces represent estimation, and solid trace represents actual simulated target phase.....	114
Figure 5-7 Amplitude tracking; simulated target has an amplitude equal to sea clutter.	114
Figure 5-8 (a) The structure of generalized sidelobe canceller. (b) Extended GSC.	118
Figure 5-9 Beamformed Doppler spectrum at DOA -50 and range 126 km.	122
Figure 5-10 Histograms of the number of targets and DOA for 10000 iterations for real data with sea clutter after pre-whitening. Estimated DOA is -50 degrees... ..	123
Figure 5-11 Traditional beamforming spatial spectrums with 16.2651 dB (solid trace) and 12.3547 dB (dashed trace).....	124
Figure 5-12 Particle Filter Estimated DOAs for simulation one.....	136
Figure 5-13 Particle Filter Estimated DOAs for simulation two	137

Acronyms

AS-CFAR	Adaptive Switching Constant False Alarm Rate
BIC	Bayesian Information Criterion
CA-CFAR	Cell Averaging Constant False Alarm Rate
CFAR	Constant False Alarm Rate
CGO-CFAR	Censored Greater Of Constant False Alarm Rate
CIT	Coherent Integration Time
CM-CFAR	Clutter Map Constant False Alarm Rate
CML-CFAR	Censored Mean-Level Constant False Alarm Rate
CODAR	Coastal Ocean Dynamics Applications Radar
DOA	Direction of Arrival
EEZ	Exclusive Economic Zone
GO-CFAR	Greatest Of Constant False Alarm Rate
GSC	Generalized Sidelobe Canceller
HF	High Frequency
HFSWR	High Frequency Surface Wave Radar
IID	Independent and Identically Distributed
K-L	Kullback-Leibler
LCMP	Linearly Constrained Minimum Power
LMS	Least Mean Square
LP	Linear Prediction
MCMC	Markov Chain Monte Carlo
MH	Metropolis-Hasting
MMSE	Minimum Mean Squared Error
MOS-CFAR	Moving Order Statistic Constant False Alarm Rate

MV	Minimum Variance
MVDR	Minimum Variance Distortionless Response
OS-CFAR	Ordered Statistics Constant False Alarm Rate
OSCR	Ocean Surface Current Radar
OSP	One-Sided Prediction
OT-DQC	Optimum Threshold Discrete Quadratic Constrained Optimization
PDF	Probability Density Function
PEF	Prediction Error Filter
PF	Penalty Function
PT-DQC	Preset Threshold Discrete Quadratic Constrained Optimization
RD	Range-Doppler
RJMCMC	Reversible Jump Markov Chain Monte Carlo
SINR	Signal to Interference and Noise Ratio
SIS	Sequential Important Sampling
SMC	Sequential Monte Carlo
SNR	Signal-to-Noise-Ratio
SOC	Second Order Cone
SO-CFAR	Smallest Of Constant False Alarm Rate
SVD	Singular Value Decomposition
TSP	Two-Sided Prediction
ULA	Uniform Linear Array

Acknowledgments

First of all I would like to thank my supervisor, Professor R. Lynn Kirlin, for his financial support and research guidance, for his continuous encouragement and trust, for his inspiring discussion and larruping thoughts. He brought me into radar signal processing area, from which I start my career. His endless research enthusiasm and fascinated personality are the constant source of encouragement for my advancement.

I would like to express my deepest gratitude to my co-supervisor, Professor Zielinski for his tremendous help and critical suggestions. Also I would like to thank Professor P. Agathoklis and Professor J. Zhou for their constructive comments and precious time in serving on my Ph.D supervision committee. Many thanks to Mrs. Vicky Smith since her help and advice keep me on the right track of graduation. I would like to share this happiness with my friends, Xingming Wang, Zhiwei Mao, Huanhuan Liang, Hui Lei, Zhou Li, to mention but a few. Their presence and generous help make this journal more colorful and unforgettable.

I am truly indebted to Dr. A. M. Ponsford for his research insights and industrial experience, for his broad knowledge and technical leadership. I really appreciate the experience to work on HFSWR system development under his supervision. Sincere thanks go to my colleagues at the former R&D group in Raytheon Canada Ltd, Dr. Jack Ding, Rick McKerracher, Dr. Reza Dizaji, for their generous help and inspiring discussions. The continuous support from my current and former bosses, Bradley Fournier and Peter Scarllet, encourages me to finish this doctoral degree in countable time. Many thanks for those colleagues and friends who keep encouraging me during the difficult time, especially to Tony Chan, Jamie Gerecke, Victor Lau and Jim Thiessen.

The last but never the least, I owe the foremost gratitude to my parents and my husband, for their unselfish and endless support, love, patience and understanding during this long journey. I would like to thank my daughter, from whom I learn responsibility and courage.

To my mom, dad, Jian & Grace

Chapter 1 - Introduction and Thesis Outline

1.1 Introduction

High Frequency (HF) radar (3-30MHz, decametric wave radar) has been proposed and applied in some specific fields such as surveillance over the sea due to the unique property that its EM radiation can propagate beyond the horizon. This is achieved either by a surface wave diffraction around the curvature of the earth, (ground or surface wave radar) [1] [2] or by sky wave refracted by the ionosphere layers (skywave radar) [3]. By this means the HF radar can sense far beyond the line of sight, and typically the range of surface wave HF radar can be extended to the order of 400 km, and sky wave radar to 4000 km or more. In this thesis our primary focus is to improve the target detection performance for HF surface wave radar (HFSWR).

HFSWR has been applied to monitor ships and aircraft within the 200 nm Exclusive Economic Zone (EEZ). In addition some ocean scientists have begun to apply HF radar for remote observation of the ocean states (surface current, wind speed, wind direction,

significant wave height and directional spectrum of the ocean surface). Examples of this kind HF radar include Coastal Ocean Dynamics Applications Radar (CODAR), Ocean Surface Current Radar (OSCR) and so on, largely because this technique is land based and can be used in all weather conditions [4].

The performance of an HFSWR is ultimately limited by external noise, interference and clutter. External noise, the sum of the galactic, atmospheric and man-made noise, is usually distributed as band-limited white Gaussian noise. There are several principal forms of interferences affecting HFSWR, which can be identified as: external interference from other users in HF band, impulsive noise (resulting from either natural lightning or man-made sources), and Meteor echoes. Spectrum monitoring (the whole HF band is continuously monitored and the unoccupied bands are automatically detected within the radar operating range), frequency agility (using the system frequency auto-hop option to achieve better detecting performance) and waveform/bandwidth control are the possible options to avoid the external interferences. Some receiver beam sidelobe control and noise suppression methods are also utilized to control interferences. Clutter is the term used by radar engineers to denote unwanted echoes received from the natural environment. Ionospheric clutter resulting from the overhead reflection of the transmit signal from an ionospheric layer or from the radar signal propagating as a skywave and reflecting from either the ocean surface or land is another kind of clutter which magnificently increases the noise level at night due to the change in ionospheric conditions. Sea clutter or sea echo can be defined as the backscattered returns from a patch of sea surface illuminated by a transmitted radar signal. It has been analyzed to include the first order and high order components [5][6][7][8]. The first-order scattering

consists of two strong spectral lines known as Bragg lines, and the high-order sea clutter consists of a continuum and a few relatively strong discrete components. The Bragg lines are due to a resonant scattering of the transmitted radar signal by ocean waves that have a wavelength equal to one half of the radar wavelength. Shearman [9] summarizes three reasonable physical models for second order scattering: 1) The sea waves are not sinusoidal but trochoidal (sharp crest and broad trough) caused by the circular motion of water particles, which can be decomposed as a fundamental sinusoid with its harmonics traveling at the same velocity. Therefore the second order scattering will take place at $\sqrt{n} \cdot f_b$, where $n=2, 3, \dots$ and f_b is the Doppler frequency of the first order Bragg lines. 2) Radar waves are scattered from two sea waves traveling at a right angle difference in direction (perpendicular to each other); this phenomenon will generally form a spectral peak at $2^{3/4} \cdot f_b$. 3) Sea waves interact with each other and result in a wave with the exactly half wavelength of the radar wave, which contributes to the continuum second order spectrum. Shearman also points out that the first mechanism could be viewed as a special case of this mechanism when the wave is interacting with itself.

The data and experiments in this thesis are gracefully provided by Raytheon Canada from their Canadian East Coast HFSWR. The East Coast HFSWR [1][2] demonstration programme has been a collaborative, cost shared, project between the Canadian Department of National Defense and Raytheon Canada Limited to develop and demonstrate the performance of HFSWR for monitoring activity within the 200 nm EEZ. As a result, this program has evolved into one of Raytheon's products: SWR-503. The basic signal data processor in the receiver includes the following blocks: pulse compression and matched filtering, interference suppression, Doppler processing,

beamforming, Constant False Alarm Rate (CFAR) detector, plot extraction and tracker as shown in Figure 1-1. The backscattered pulses including target and clutter returns are received by a linear phased array, which are fed into the pulse compression and matched filtering block firstly. The pulse compression tends to compress the radiated long pulses on transmitter (in order to obtain efficient use of power capability) into the short pulses on receiver (in order to obtain good range resolution) while maximizing signal-to-noise-ratio (SNR). Moreover the interferences are detected and suppressed from the resultant IQ data (In phase channel and Quadrature phase channel baseband signals). Impulsive noise excision is one processing option in this block that we will study in the later chapter. In Doppler processing, the fast Fourier transform or similar technique has been implemented to improve the SNR by coherent integrating along with the pulse dimension of the range gated signal. After integration, the beamforming process forms individual beams to cover the interested area and adaptive sidelobe control methods may be included to improve the following target detection performance. The output of the beamforming process is fed into the CFAR detector for target detection. The plot extractor associates all detections corresponding to one target into one cluster and feeds its output information (range, Doppler, power and bearing) into the tracker for association and display.

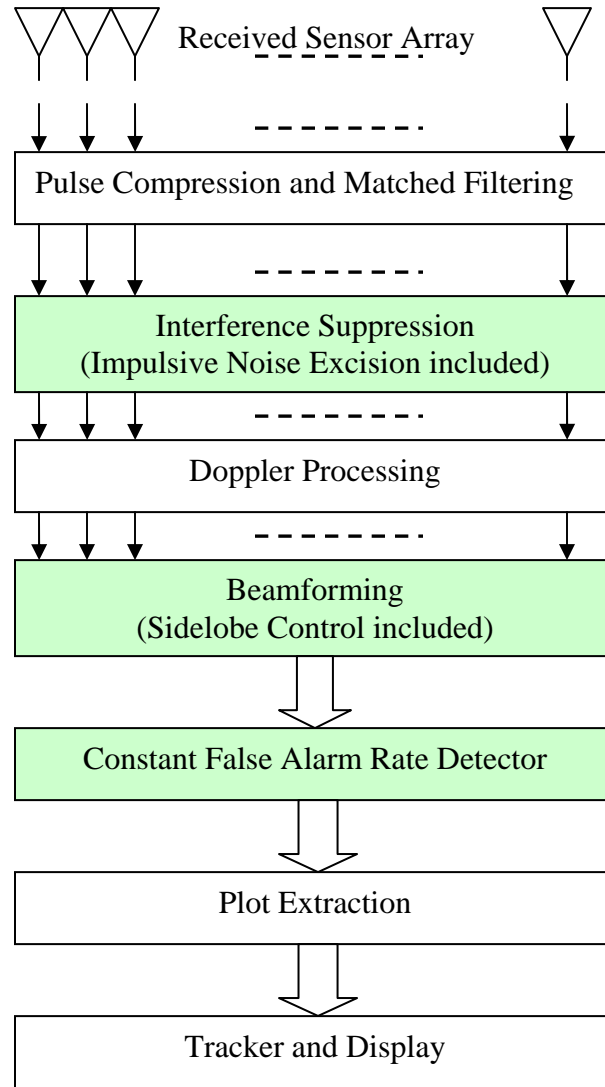


Figure 1-1 Block diagram for Signal Processing in HFSWR radar system

1.2 Outline and Contents

In this thesis we study several processing modules in the HFSWR system to propose and then implement the enhanced algorithms for those modules in order to improve the system's overall detection and tracking performance.

The temporal impulsive noise is an external interference caused by local lightning discharge or man-made noise which can dramatically increase the total system broadband background noise level and thus preclude the target detection. In chapter two, we review the approaches proposed in the references and discuss the disadvantages to directly apply those approaches to HF radar. Then the new excision approach is proposed and implemented to improve the detection and estimation in the impulses without unexpected frequency leakage. Two modified linear prediction methods are proposed to correct the impulsive noise-corrupted data. The corresponding performances are compared with both real data experiments and theoretical analysis.

The existence of non-stationary sea clutter and ionospheric clutter can result in excessive false alarm rate through the high sidelobe level in adaptive beamforming. The existing approaches such as diagonal loading and penalty function can not provide the optimal solution due to their methodology limitation. In chapter three, multiple discrete quadratic inequality constraints outside the main beam are set up to guarantee the sidelobe-controlling problem consistently feasible and optimal. The efficiency and advantage of the proposed algorithm are demonstrated with both simulation and experiments.

CFAR is the common technique to detect targets in the noisy background. In chapter four, the overview of various CFAR algorithms and the advantage/disadvantage of each one are provided. Based on the specific characteristic of the HFSWR system, we propose an adaptive switching CFAR to enhance targets detection in the beamformed range-Doppler map. The switching rule is implemented to adaptively discriminate homogeneous background from non-homogeneous background and then proper CFAR

algorithm is applied in each specific noise background. Moreover the adaptive reference window footprint is adopted to decrease the false alarm around clutter edge. This novel approach has been tested in the real system extensively, and the results have consistently verified the significant improvement in both probability of detection and reduction of false detections due to clutter.

Besides the general CFAR detection in Doppler¹ (frequency) dimension, we also study the potential methods to detect targets with the pulse (time) domain characteristics in chapter five. When a target has a Doppler frequency similar to a Bragg line, conventional Doppler processing fails to discriminate it since the detection features, amplitude and frequency are similar from target to the Bragg lines. With extra phase modulation information, the detector proposed in Chapter 5 can solve this kind of co-located co-channel resolvability issue. Moreover with the pre-whitening processing, the Markov Chain Monte Carlo method is another option for target number and Direction-of-Arrival estimation.

Finally the thesis is summarized and concluded in chapter six. All the chapters are basically self-contained and independent to each other. The alphabet and signs are defined within each chapter.

1.3 Main Contributions

The main contributions of this thesis are:

- The impulsive noise excision algorithm is proposed to remove the unwanted impulsive noise without introducing frequency leakage (due to potential

¹ Note: Doppler and pulse are well accepted terms in radar field. Doppler dimension is equivalent to frequency dimension and pulse dimension is equivalent to time dimension.

discontinuity of the reconstructed signal) over the whole signal band. Forward-backward linear prediction and block linear prediction are introduced for corrupted signal reconstruction, whose theoretical performances are analyzed and compared to the conventionally forward linear prediction. Signal property mapping has been applied on the estimated covariance matrix to further improve the prediction performance especially for weak signal. A novel interpretation of the performance is presented based on Gaussian multiple mixture model.

- The optimum threshold discrete quadratic constrained method is proposed to provide the optimal and feasible solution for sidelobe control in adaptive beamforming. The idea behind this novel algorithm is to search for the optimal solution that trades off the interference null depth, the mainlobe width and the sidelobe level automatically. Both simulation and experimental results validate the improved performance and feasibility of our method against the conventional methods such as diagonal loading, penalty function and MVDR with Quadratic Inequality Constraints. All the sidelobe approaches are formulated into second order cone problem, which can be solved efficiently via primal-dual interior point methods.
- The novel hybrid CFAR method with adaptive footprint is proposed and implemented which is applicable for the complex clutter and noise situation in HF radar detection. For this new method about 14% probability of detection improvement has been verified by the data collected from experiments, and meanwhile the false alarm rate is reduced significantly compared to the original CFAR.

- A detector is proposed to resolve co-located targets or target with interference with similar frequencies based on their distinct phase modulation. Simulated data with real sea clutter has verified the effectiveness of the proposed algorithm.
- The pre-whitened Reversible Jump Markov Chain Monte Carlo method is applied to detect targets in sea clutter background. The pre-whitened RJMCMC has much lower detection threshold compared to beamforming and subspace methods. RJMCMC is able to convergent to the optimal resolution for a data set that is small compared with information theoretic criteria.

Chapter 2 - Impulsive Noise Excision

2.1 Introduction

One of the external interferences presenting in the HFSWR is impulsive noise. Large impulsive noise which is well above the normal background level will appear occasionally due to regional lightning discharges or local man-made sources. These large spikes have a short duration and affect only a few received pulses for all ranges. Moreover there is unpredictable frequency distortion on sea clutter during the impulsive noise period, which is partially caused by the non-linear amplifier response. HFSWR is a pulse Doppler radar where the basic data processing includes spectral analysis with Fourier transform. If not being removed, the impulsive noise can dramatically increase the total system broadband noise energy, which may preclude the potential targets detecting and tracking at all Dopplers. Hereafter the impulsive noise excision is important in practical operation. The range-pulse maps for two continuous Coherent Integration Times (CITs) are presented in Figure 2-1 and Figure 2-2 respectively. There is no

impulsive noise in the first CIT while there are impulsive noise at all ranges in the second CIT for certain period of time.

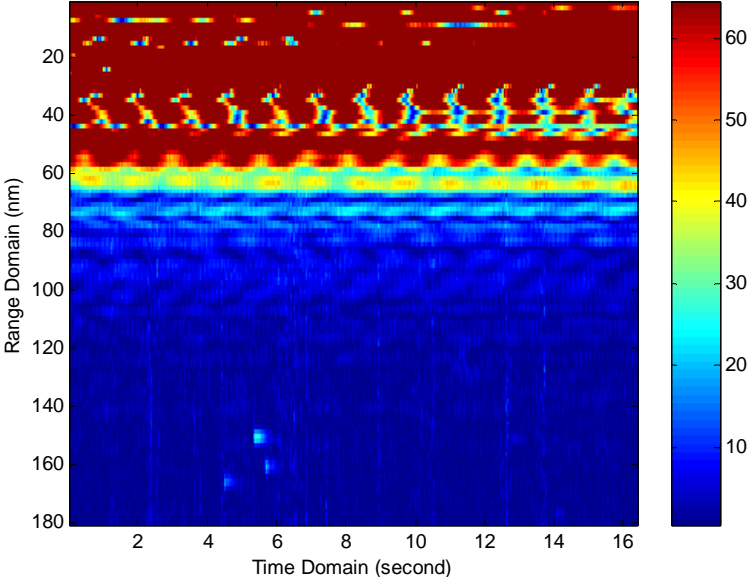


Figure 2-1 The range-pulse map for one CIT without impulsive noise

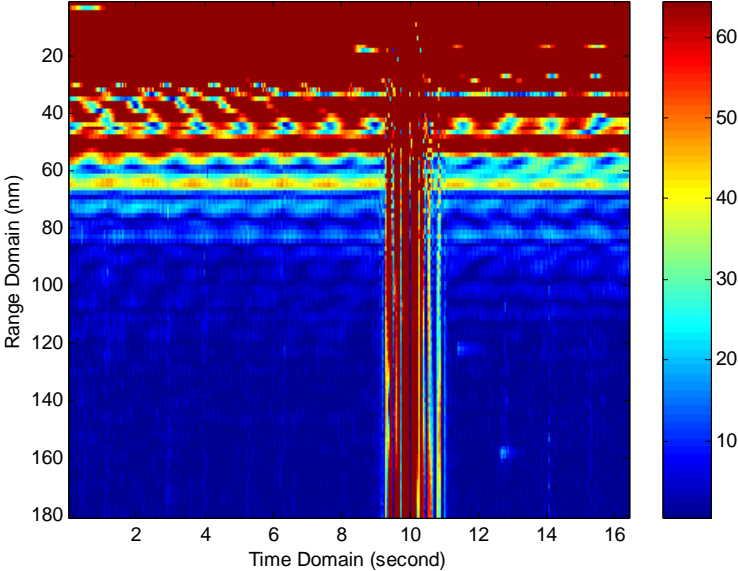


Figure 2-2 The range-pulse map for the next CIT with impulsive noise

In order to improve the system detection and tracking performance, the impulsive noise is generally eliminated in two continuous steps: firstly the segments of time-domain data corrupted by the impulsive burst are detected; secondly those corrupted segments are reconstructed by the appropriate sample estimates. Several existing impulsive noise excision methods for HF radar are summarized in the following paragraph.

For over-the-horizon radar, Barnum and Simpson [10] present the “3-FFT method” to detect and remove the impulsive spikes, wherein the clutter is removed prior to spike removal threshold decision. The narrow clutter spectrum surrounding zero Doppler is masked (i.e. removed and saved), and the rest high frequency samples whose amplitudes are above the threshold are considered to be impulsive noise and are then eliminated. The threshold is set at 5 times of the median absolute noise background that is estimated using the bottom 15 percentile of magnitude samples and assumes Rayleigh statistics. The remaining samples after impulsive noise excision are transformed back to the Doppler domain, after which the clutter spectra are replaced. Yu et al. [11] present a similar principle to suppress impulsive disturbance while determining the threshold using the $k\sigma$ criterion. After canceling the first-order Bragg peaks, the signal echo mainly consists of the Gaussian distributed noise, the target returns (whose strength is neglectable compared with that of the noise) and impulsive noise. The signal echo is assumed to be complex Gaussian distribution when impulsive noise does not exist. The $k\sigma$ criterion is used to judge whether the signal is distributed normal where the parameter k is the relevant wild-value-elimination threshold and the parameter σ is the standard deviation of the Gaussian distribution. However there are several issues for the practical application of these methods to the HFSWR system directly.

One of the challenging problems in HFSWR is to detect a weak low-speed ship echo located between the first-order Bragg peaks in the Doppler spectrum. The Bragg lines are typically two low Doppler frequency spectral peaks caused by normal sea conditions: waves moving at half the radar wavelength away from and toward the radar. No high-pass filter can mask the Bragg-line while retain the target at the same time. In addition, simply blanking the impulsive burst introduces unnecessary high-frequency components in the Doppler dimension due to the signal discontinuity around the blanking zone. Finally the optimum impulsive noise detection threshold is critical but difficult to determine for an arbitrary sea state situation if the corrupted segments are only replaced by the zeros as in the existing implementation. The appropriate reconstruction of the impulsive noise corrupted data with smoothing transition can solve these problems. Certain signal models are utilized to develop interpolation methods for the reconstruction of the corrupted data.

Linear prediction is an effective way to estimate or predict the missing/bad data segments in time series analysis. In section 2.2, we present the basic principle of the algorithm and develop the corresponding specific modifications applied in the impulsive noise excision based on the noise characteristic in the HFSWR system. Experimental results are presented to verify the effectiveness of our algorithms. The performance analysis based on the minimum variance criterion is presented in section 2.3. In section 2.4 we interpolate and explain the estimation performance based on multiple Gaussian mixture model. Further improvements are also discussed based on signal enhancement.

2.2 Linear Prediction and Its Modifications

2.2.1 Basic Principle

Predicting a future value of a stationary discrete-time stochastic process given a set of existing samples of the process is a key problem in time series analysis. Linear prediction [13] is one approach to solve this problem by linear combination of the past samples. Specifically we can estimate the value of x_n given $x_{n-1}, x_{n-2}, \dots, x_{n-M}$ where M is defined as the order of the linear prediction. This form is also referred as forward linear prediction with the following formula:

$$\hat{x}_n = \sum_{i=1}^M a_i x_{n-i} \quad (2.1)$$

The tap-weight vector $\mathbf{a} = [a_1, a_2, \dots, a_M]^T$ is estimated from the Wiener-Hopf equation through minimizing the prediction root mean square error as

$$\mathbf{a} = \mathbf{R}^{-1} \mathbf{r} \quad (2.2)$$

where the autocorrelation matrix of the tap inputs is

$$\begin{aligned} \mathbf{R} &= E \left\{ \begin{bmatrix} x_{n-1} & x_{n-2} & \dots & x_{n-M} \end{bmatrix} \begin{bmatrix} x_{n-1} & x_{n-2} & \dots & x_{n-M} \end{bmatrix}^H \right\} \\ &= \begin{bmatrix} r(0) & r(1) & \dots & r(M-1) \\ r(-1) & r(0) & \dots & r(M-2) \\ \vdots & \vdots & \ddots & \vdots \\ r(1-M) & r(2-M) & \dots & r(0) \end{bmatrix} \end{aligned}$$

and the cross-correlation vector between the tap inputs and the desired response x_n is

$$\begin{aligned} \mathbf{r} &= E \left\{ \begin{bmatrix} x_{n-1} & x_{n-2} & \dots & x_{n-M} \end{bmatrix}^H \bullet x_n \right\} \\ &= [r(-1) \quad r(-2) \quad \dots \quad r(-M)]^T \end{aligned}$$

where $[\bullet]^T, [\bullet]^*, [\bullet]^H$ mean the transpose, complex conjugate and conjugate transpose of the matrix or vector respectively.

If we use the samples $x_n, x_{n-1}, \dots, x_{n-M+1}$ to make a prediction of the past sample x_{n-M} , this form is referred as backward linear prediction as

$$\hat{x}_{n-M} = \sum_{i=1}^M b_i x_{n-M+i} \quad (2.3)$$

The tap-weight vector $\mathbf{b} = [b_1, b_2, \dots, b_M]^T$ is also estimated from the Wiener-Hopf equation and is the same as the complex conjugate of the weight vector in the forward linear prediction when considering the same stochastic stationary process

$$\mathbf{b} = \mathbf{a}^*$$

2.2.2 Forward-Backward Linear Prediction

In general the linear prediction algorithm is the optimal solution for one sample prediction based on the mean square error criterion in stationary signal processing. However it is obvious that the prediction error will grow as the prediction length increases for both the forward and backward directions. Especially the frequency change in the corrupted segments in HFSWR system makes the processing non-stationary. Hereafter we propose to combine the forward and backward prediction results to reduce the prediction error. The combination weights should depend on prediction length and be limited between zero and unity such as hyperbolic tangent function, cosine function or simple step function. First of all, the coefficients in the forward prediction are estimated from the good samples in the data set. Then the samples in the corrupted segments are replaced by a weighted combination of the forward and backward linear prediction as

$$\hat{x}_n = w_t \cdot \sum_{i=1}^M a_i x_{n-i} + (1 - w_t) \cdot \sum_{i=1}^M a_i^* x_{n+i} \quad (2.4)$$

where the weight function w_t is chosen to be the hyperbolic tangent function (scalar L is the number of the predicted values) with t being the variable to indicate the relative position within the estimated data window,

$$w_t = \frac{1}{e^{\frac{(2t-L) \times 10}{L}} + 1}$$

which is shown in Figure 2-3.

Through including the nonlinear weights in the combined algorithm, the total prediction error has been decreased and also the smoothed transition has been built among the corrupted segments and the neighboring good samples.

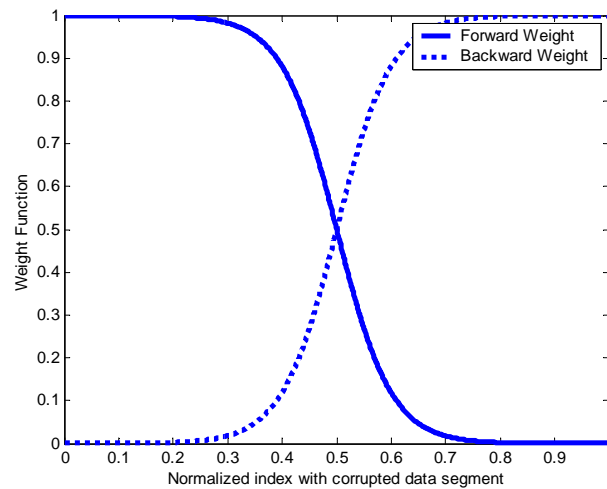


Figure 2-3 Forward and Backward Weight Function

2.2.3 Block Linear Prediction

A better estimate of a sample is expected if we predict the present sample based on both the past and future samples; this motivates the utilization of two-sided prediction (TSP). TSP is an extension of one-sided prediction (OSP) such as forward or backward

predictions in that the present value is evaluated by the symmetrical combination of the past and future values as

$$\hat{x}_n = \sum_{i=1}^M c_i (x_{n-i} + x_{n+i}) \quad (2.5)$$

Since the forward and backward parameters are identical, it means the process is stationary and $r(i) = r(-i)$. Multiply both sides of equation (2.5) by x_{n-i} for $i = 1, 2, \dots, M$ and then take expectation. The resultant M equations can be written in the following Toeplitz-plus-Hankel matrix [130]

$$(\mathbf{R} + \mathbf{R}_h) \mathbf{c} = \mathbf{r} \quad (2.6)$$

where \mathbf{R} is a Toeplitz (auto-correlation) matrix:

$$\mathbf{R} = \begin{bmatrix} r(0) & r(1) & \dots & r(M-1) \\ r(1) & r(0) & \dots & r(M-2) \\ \vdots & \vdots & \ddots & \vdots \\ r(M-1) & r(M-1) & \dots & r(0) \end{bmatrix}$$

and \mathbf{R}_h is a Hankel matrix:

$$\mathbf{R}_h = \begin{bmatrix} r(2) & r(3) & \dots & r(M+1) \\ r(3) & r(4) & \dots & r(M+2) \\ \vdots & \vdots & \ddots & \vdots \\ r(M+1) & r(M+2) & \dots & r(2M) \end{bmatrix}$$

and $\mathbf{c} = [c_1 \ c_2 \ \dots \ c_M]^T$.

The covariance TSP [14] is a practical algorithm to solve equation (2.6). Moreover TSP should have a smaller variance residual than that of OSP, and in theory one block linear prediction to reconstruct a block of destroyed points based on TSP will have better performance than the general forward or backward prediction method [12].

The corresponding reconstructed values are obtained by solving the following Toeplitz system

$$\mathbf{C}\hat{\mathbf{x}} = \mathbf{f}_x + \mathbf{b}_x$$

where vector $\hat{\mathbf{x}}$ is reconstructed points $[\hat{x}_k \cdots \hat{x}_{k+L}]^T$ and \mathbf{C} is a $(L+1) \times (L+1)$ symmetrical Toeplitz matrix (assuming $L > 2M$) as:

$$\mathbf{C} = \begin{bmatrix} 1 & -c_1 & \cdots & -c_M & 0 & \cdots & 0 \\ -c_1 & 1 & -c_1 & \cdots & -c_M & 0 & \vdots \\ \vdots & \vdots & \vdots & \vdots & \vdots & \vdots & \vdots \\ -c_M & \cdots & -c_1 & 1 & -c_1 & \cdots & 0 \\ \vdots & \vdots & \vdots & \vdots & \vdots & \vdots & \vdots \\ 0 & \cdots & 0 & -c_M & \cdots & -c_1 & 1 \end{bmatrix}$$

Vectors \mathbf{f}_x and \mathbf{b}_x contain the combined former and latter signal points' information respectively as

$$\mathbf{f}_x = \begin{bmatrix} c_M & c_{M-1} & \cdots & c_1 \\ 0 & c_M & \cdots & c_2 \\ \vdots & \vdots & \vdots & \vdots \\ 0 & \cdots & 0 & c_M \\ \vdots & \vdots & \vdots & \vdots \\ 0 & \cdots & \cdots & 0 \end{bmatrix}_{(L+1) \times M} \times \begin{bmatrix} x_{k-M} \\ \vdots \\ x_{k-1} \end{bmatrix}$$

$$\mathbf{b}_x = \begin{bmatrix} 0 & 0 & \cdots & 0 \\ 0 & 0 & \cdots & 0 \\ \vdots & \vdots & \vdots & \vdots \\ 0 & \cdots & 0 & c_1 \\ \vdots & \vdots & \vdots & \vdots \\ c_1 & c_2 & \cdots & c_M \end{bmatrix}_{(L+1) \times M} \times \begin{bmatrix} x_{k+L+1} \\ \vdots \\ x_{k+L+M} \end{bmatrix}$$

2.2.4 Excision Algorithm

The proposed excision algorithm is composed of two parts: 1) detection and 2) reconstruction. The first step, locating those potential impulsive noise points, is realized

by comparing the amplitude of each point with a pre-set threshold. The threshold is set according to [5]. This threshold is in no way optimal because of the complexity of the non-Gaussian background noises. In order to eliminate the sea clutter impaction, one notch filter is applied to bandpass the Doppler spectrum of the radar echo around Bragg line frequencies before impulsive noise detection. Traditionally the detected impulses are blanked (zeroed). However we propose modified linear prediction methods to recover these data corrupted by impulsive noise. The direct benefit is the increased robustness in that even the points that are falsely detected as impulsive noise remain as estimated values very close to original true ones.

2.2.5 Experimental Results

In this section we compare the performances of our two excision methods with that of the conventional blanking process by using the real data recorded from the HF radar at Bahamas on June 6, 2002. Raytheon Canada Limited has graciously provided the data set to test our algorithms. The radar with a carrier frequency of 14.5 MHz utilizes a 7 element monopole log periodic transmitting antenna and an 8 sensor uniform linear array on receive to cover 120 degree sector over the area of interests. The data set is collected, at pulse repetition frequency of 500 Hz and decimated to 31.25 Hz. The coherent integration time is about 16 seconds. The received signals are matched filtered and then downsampled to baseband with IQ (In-phase and Quadrature-phase) channels. The detection range is from 13.5 km to 192 km with 1.5 km resolution. The parameters of the linear model are estimated from the former CIT time series without impulsive noise. The range-Doppler map has 512-by-120 pixels. In order to test the probability of signal

detection, we inject a simulated weak target (~ 10 dB SNR) with Doppler frequency of 10 Hz (speed about 103 m/s) at range 42 km.

Figure 2-4 shows the raw data range-Doppler spectrum map. It is obvious that the simulated target and other unknown targets are totally masked in this map for all ranges and Doppler bins due to the impulsive noise. The two straight lines around zero frequency are first-order Bragg lines. The Doppler spectrum after detecting the impulsive noise and blanking to zero is shown in Figure 2-5. We can see the impulsive noise removal for far ranges is much better than that for near ranges because the radar echo for range greater than 100 km at 14.5 MHz carrier frequency is weak enough to be considered nearly background noise. There is minimum spectrum leakage due to blanking for these far ranges. But the simulated target is still undetectable, since simple blanking will raise the power of the high frequency spectrum (similar as adding a smaller pseudo impulsive noise) in near ranges. However we can clearly observe several target candidates and the simulated target (marked by the circle) directly in Figures 2-6 and 2-7, which present the spectrum map from forward-backward and block predictions respectively.

In order to understand the pulse-domain property, we show the CIT time series (In-phase channel data) at range 42 km in Figure 2-8, where the preset threshold for impulsive noise detection is a little low, resulting in misclassification of some noise-free points as impulses. However the forward-backward and block predictions retain those false detected spikes with the correct values and do not contaminate the final spectrum. By this means we have reconstructed the pixels that were falsely detected as impulsive noise due to the non-optimal threshold and have enhanced the robustness of the algorithm.

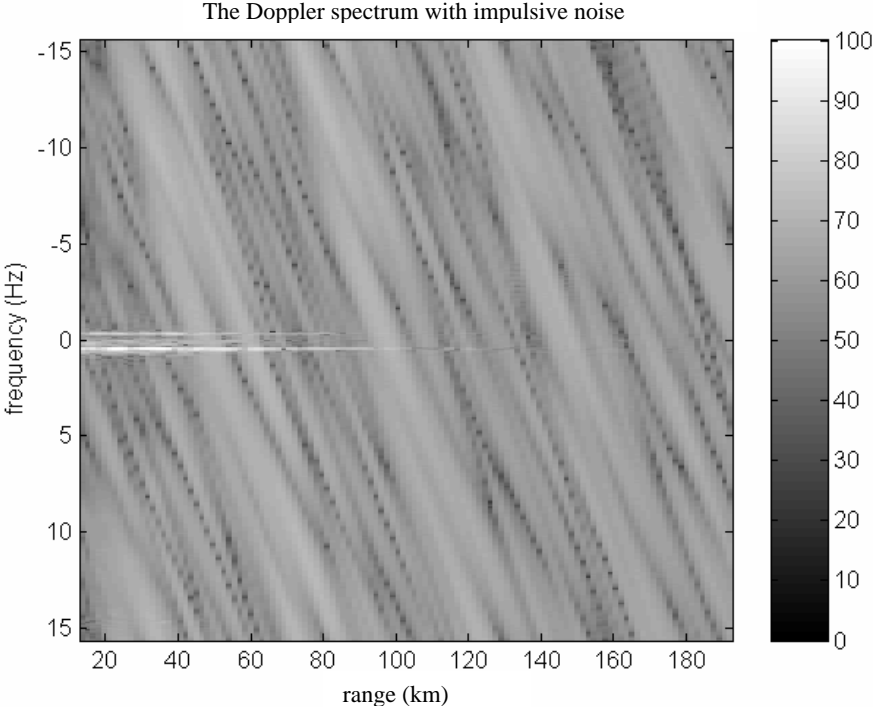


Figure 2-4 The range-Doppler map for the original data with impulsive noise

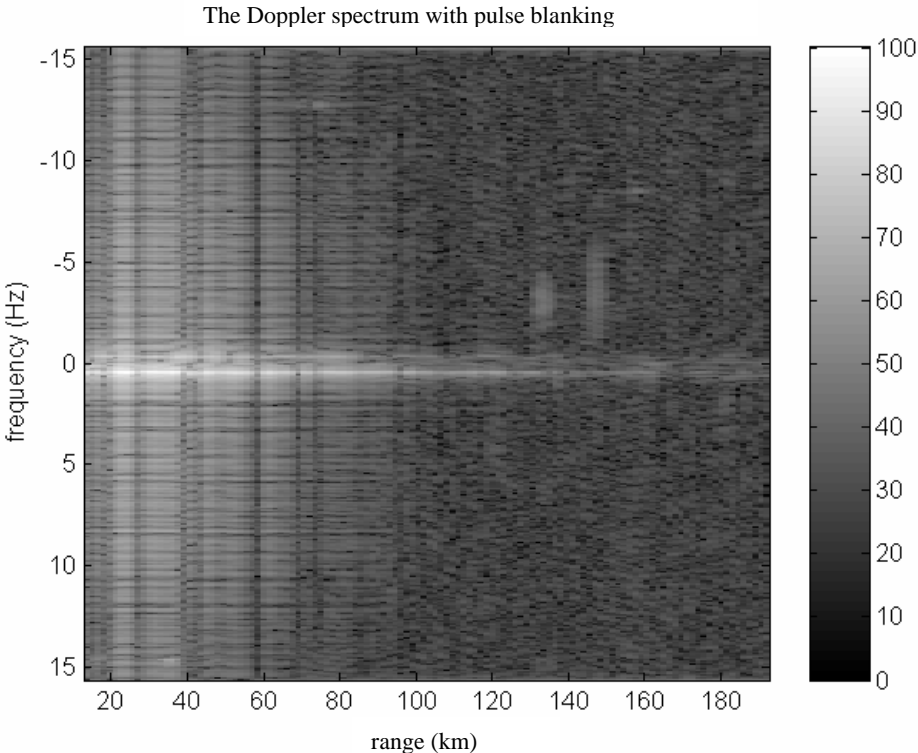


Figure 2-5 The range-Doppler map by blanking the impulsive noise

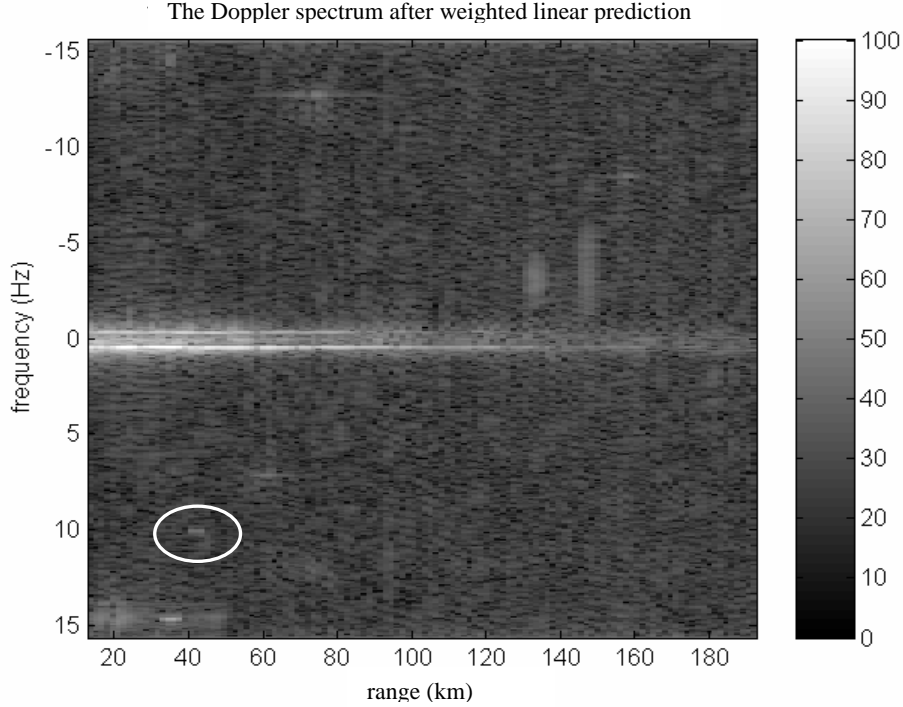


Figure 2-6 The range-Doppler map using the forward-backward linear prediction

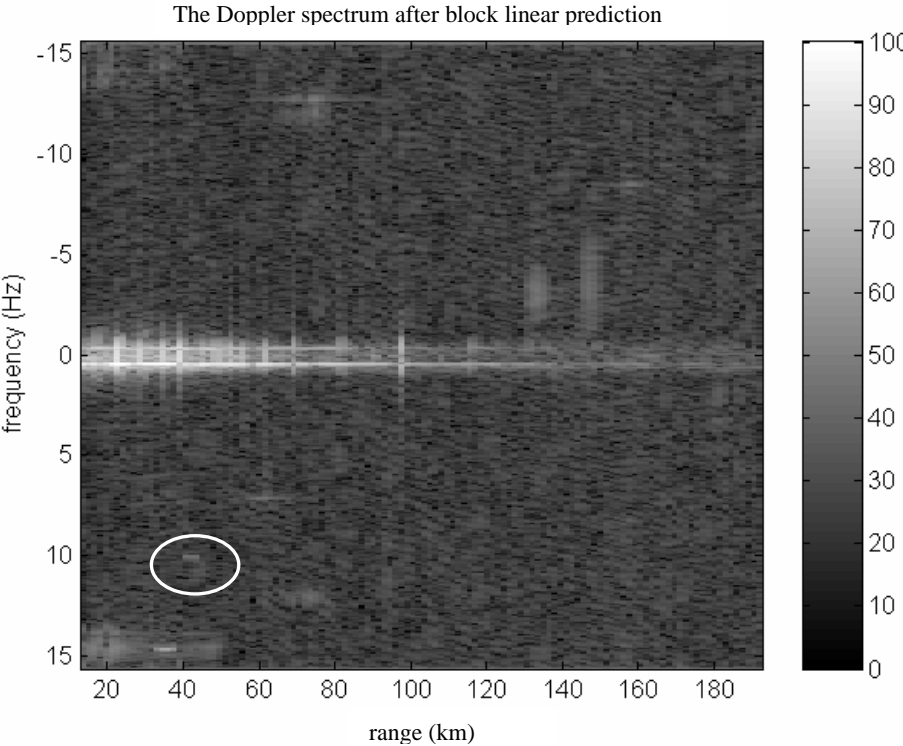


Figure 2-7 The range-Doppler map using the block linear prediction

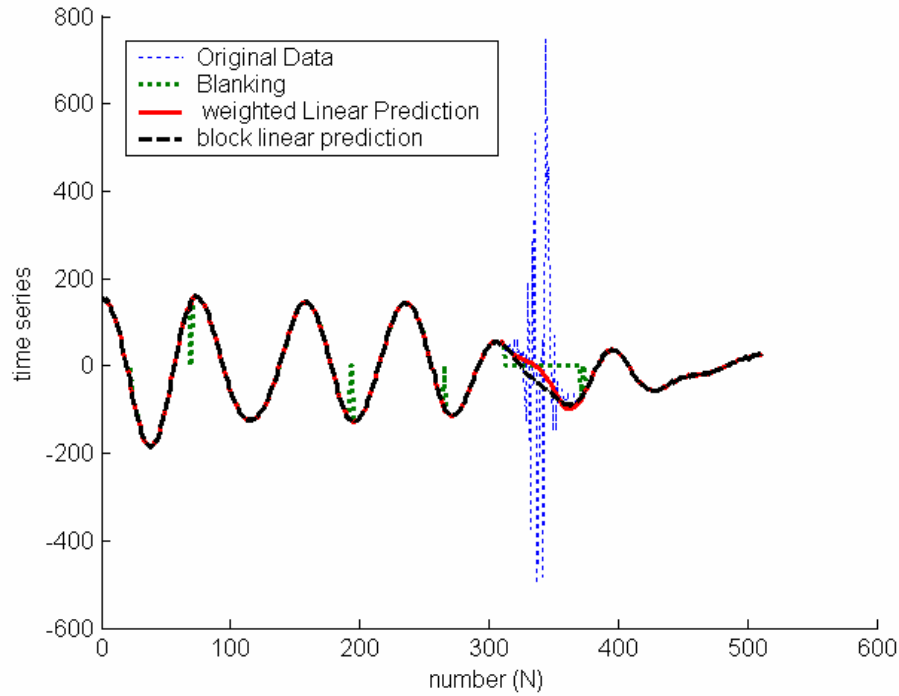


Figure 2-8 The amplitude of one CIT record with impulsive noise at range=42 km

2.3 Performance Analysis

We have introduced the basic forward linear prediction and two modified versions: forward-backward prediction and block linear prediction for impulsive noise excision. The experiment results have been presented to demonstrate the improvements in detection of weak targets in impulsive noise using these prediction algorithms.

In this section we analyze and compare the performances of linear prediction methods proposed in this chapter for our specific data estimation problem. Compared with Minimum Mean Squared Error (MMSE), mostly defined for optimal parameter estimation, Minimum Variance (MV) is a more practical performance measurement. MV uses the variance of estimation error as standard criteria in which both parameter estimation and missing/corrupted data reconstruction are considered [116]. Assuming d_n

is the exact or expected data value at time n , and \hat{d}_n is its estimation; the minimum variance is defined as

$$\min\{V\} = \min \left\{ E \left[\left(d_n - \hat{d}_n \right)^2 \right] \right\} \quad (2.7)$$

MV Formalization

With \hat{d}_n as the forward linear prediction estimation equation (2.7) becomes

$$\min\{V_1\} = \min_{a_i} \left\{ E \left[\left(d_n - \sum_{i=1}^M a_i x_{n-i} \right)^2 \right] \right\} = \min\{\varepsilon_1^2\} \quad (2.8)$$

where ε_1^2 is the mean square error (MSE) for forward linear prediction. Equation (2.8)

indicates that the MV and MMSE are consistent for forward linear prediction.

For forward-backward linear prediction \hat{d}_n is the weighted combination of forward and backward estimations. Both forward and backward prediction error minimizations yield the same optimum weight vector, and equation (2.7) becomes

$$\begin{aligned} \min\{V_2\} &= \min_{a_i} \left\{ E \left[\left(d_n - \left(w_t \cdot \sum_{i=1}^M a_i x_{n-i} + (1-w_t) \cdot \sum_{i=1}^M a_i^* x_{n+i} \right) \right)^2 \right] \right\} \\ &= \min_{a_i} \left\{ \left(w_t^2 + (1-w_t)^2 \right) \varepsilon_1^2 + 2w_t(1-w_t) \cdot E \left[\left(d_n - \sum_{i=1}^M a_i x_{n-i} \right) \left(d_n - \sum_{i=1}^M a_i^* x_{n+i} \right) \right] \right\} \end{aligned} \quad (2.9)$$

For simplicity the varied tap-weights $\{w_t\}$ are assumed to be constant 0.5, and equation

(2.9) accordingly leads to

$$\min\{V_2\} = \min_{a_i} \left\{ \frac{\varepsilon_1^2}{2} + 0.5 \cdot E \left[\left(d_n - \sum_{i=1}^M a_i x_{n-i} \right) \left(d_n - \sum_{i=1}^M a_i^* x_{n+i} \right) \right] \right\} \quad (2.10)$$

where the MV of forward-backward linear prediction is different from its MMSE.

With block linear prediction \hat{d}_n combines information from not only past and future data but also their cross-correlations, and equation (2.7) becomes

$$\min \{V_3\} = \min_{a_i} \left\{ E \left[\left(d_n - \sum_{i=1}^M a_i (x_{n-i} + x_{n+i}) \right)^2 \right] \right\} = \min \{ \varepsilon_3^2 \} \quad (2.11)$$

where the MV of block prediction is the same as its MMSE, $\min \{ \varepsilon_3^2 \}$. It is emphasized that the MMSE of forward prediction is different from that of block prediction due to the consideration of the extra cross-coupled terms in the latter.

From the upper equations it is indicated that the MV estimations are fully or partially related to MMSE for various linear predictions. In order to minimize the MSEs, taking the derivative of ε_i^2 ($i = 1, 3$) with respect to the weights $\{a_i\}$ and setting the result to zero lead to a set of M normal equations:

$$\sum_{i=1}^M a_i E[x_{n-i} x_{n-k}] = E[d_n x_{n-k}] \quad 1 \leq k \leq M \quad (2.12)$$

$$\sum_{i=1}^M a_i E[(x_{n-i} + x_{n+i})(x_{n-k} + x_{n+k})] = E[d_n (x_{n-k} + x_{n+k})] \quad 1 \leq k \leq M \quad (2.13)$$

Special Case Study

For our impulsive noise estimation the input signal is assumed to consist of first-order Bragg lines, wideband impulsive noise and white noise. Without loss of generality, we can examine only the real part of the complex signal for further analysis. Based on the assumption, the input signal is described as

$$x_n = A_1 \cos(n\Omega_1 + \theta_1) + A_2 \cos(n\Omega_2 + \theta_2) + b_n + \eta_n \quad (2.14)$$

where b_n and η_n are the wideband impulsive noise and white noise at time n respectively, and the Bragg lines are represented as the mixture of two strong sinusoidal signals with frequencies $\{\Omega_1, \Omega_2\}$ and initial phases $\{\theta_1, \theta_2\}$. Assuming that all the signals and noise are wide-sense stationary and statistically uncorrelated with each other, we obtain the expectation of the autocorrelation function as

$$E[x_n x_{n-k}] = \frac{A_1^2}{2} \cos(k\Omega_1) + \frac{A_2^2}{2} \cos(k\Omega_2) + E[b_n^2] \delta(k) + \sigma_\eta^2 \delta(k) \quad (2.15)$$

The undetermined coefficients method discussed in [115] provides a particular solution for optimal weight $\{a_i\}$ in terms of unknown constants and substitutes this assumed solution into M normal equations in (2.12) and (2.13) for estimating the unknown constant in the formation. For our problem the assumed solution takes the form of four weighted sinusoids

$$a_k = \sum_{l=1}^4 P_l e^{j\Omega_l k} \quad (1 \leq k \leq M) \quad (2.16)$$

where for notational convenience Ω_{l+N} are defined as $-\Omega_l$ ($l = 1, 2; N = 2$); the Ω_{l+N} are thus the negative frequency components of the input sinusoids. Substituting (2.15) and (2.16) into (2.12), the left and right sides of the equation are separately described as follows:

$$\begin{aligned}
Left &= \sum_{i=1}^M \sum_{l=1}^4 P_l e^{j\Omega_l i} \left(\frac{A_1^2}{2} \cos((k-i)\Omega_1) + \frac{A_2^2}{2} \cos((k-i)\Omega_2) + E[b_n^2] \delta(k-i) + \sigma_\eta^2 \delta(k-i) \right) \\
&= \sum_{l=1}^4 \sum_{m=1}^2 \frac{A_m^2 P_l}{2} \sum_{i=1}^M \cos((k-i)\Omega_m) e^{j\Omega_l i} + \sum_{l=1}^4 P_l e^{j\Omega_l k} (E[b_n^2] + \sigma_\eta^2) \\
&= \sum_{l=1}^4 \sum_{m=1}^2 \frac{A_m^2 P_l}{4} \sum_{i=1}^M (e^{j(k-i)\Omega_m} + e^{-j(k-i)\Omega_m}) e^{j\Omega_l i} + \sum_{l=1}^4 P_l e^{j\Omega_l k} (E[b_n^2] + \sigma_\eta^2) \\
&= \sum_{l=1}^4 \sum_{m=1}^2 \frac{A_m^2 P_l}{4} \sum_{i=1}^M e^{j(k-i)\Omega_m} e^{j\Omega_l i} + \sum_{l=1}^4 P_l e^{j\Omega_l k} (E[b_n^2] + \sigma_\eta^2) \\
&= \sum_{l=1}^4 \sum_{m=1}^2 \frac{A_m^2 P_l}{4} e^{jk\Omega_m} \sum_{i=1}^M e^{j(\Omega_l - \Omega_m)i} + \sum_{l=1}^4 P_l e^{j\Omega_l k} (E[b_n^2] + \sigma_\eta^2) \\
&= \sum_{l=1}^4 \frac{A_l^2 P_l}{4} e^{jk\Omega_l} \cdot M + \sum_{l=1}^4 \sum_{\substack{m=1 \\ m \neq l}}^2 \frac{A_l^2 P_m}{4} e^{jk\Omega_l} \frac{e^{j(\Omega_m - \Omega_l)M} - 1}{1 - e^{-j(\Omega_m - \Omega_l)}} + \sum_{l=1}^4 P_l e^{j\Omega_l k} (E[b_n^2] + \sigma_\eta^2) \\
&= \sum_{l=1}^4 \frac{e^{jk\Omega_l}}{4} \left(A_l^2 P_l M + \sum_{\substack{m=1 \\ m \neq l}}^2 A_l^2 P_m \frac{e^{j(\Omega_m - \Omega_l)M} - 1}{1 - e^{-j(\Omega_m - \Omega_l)}} + 4P_l (E[b_n^2] + \sigma_\eta^2) \right) \\
&= \sum_{l=1}^4 \frac{e^{jk\Omega_l}}{4} \left((A_l^2 M + 4E[b_n^2] + 4\sigma_\eta^2) P_l + \sum_{\substack{m=1 \\ m \neq l}}^2 A_l^2 P_m \frac{e^{j(\Omega_m - \Omega_l)M} - 1}{1 - e^{-j(\Omega_m - \Omega_l)}} \right)
\end{aligned}$$

$$\begin{aligned}
Right &= \frac{A_1^2}{2} \cos(k\Omega_1) + \frac{A_2^2}{2} \cos(k\Omega_2) \\
&= \sum_{l=1}^4 \frac{A_l^2}{4} e^{jk\Omega_l}
\end{aligned}$$

Equating coefficients of $\exp(j\Omega_l k)$ on both sides of the resulting equations leads to

$$\begin{aligned}
P_l (A_l^2 M + 4E[b_n^2] + 4\sigma_\eta^2) + \sum_{\substack{m=1 \\ m \neq l}}^2 A_l^2 P_m \frac{e^{j(\Omega_m - \Omega_l)M} - 1}{1 - e^{-j(\Omega_m - \Omega_l)}} &= A_l^2 \\
\Rightarrow P_l + \sum_{\substack{m=1 \\ m \neq l}}^2 \frac{P_m}{M + 4 \times (E[b_n^2] + \sigma_\eta^2) / A_l^2} \frac{e^{j(\Omega_m - \Omega_l)M} - 1}{1 - e^{-j(\Omega_m - \Omega_l)}} &= \frac{1}{M + 4 \times (E[b_n^2] + \sigma_\eta^2) / A_l^2}
\end{aligned}$$

The interaction between the positive and negative frequency components is small [115], and the upper 4-by-4 linear equations are converted to the two independent sets of 2-by-2 equations:

$$P_l + \sum_{\substack{m=1 \\ m \neq l}}^2 \frac{P_m}{M + 4 \times (E[b_n^2] + \sigma_\eta^2) / A_l^2} \frac{e^{j(\Omega_m - \Omega_l)M} - 1}{1 - e^{-j(\Omega_m - \Omega_l)}} = \frac{1}{M + 4 \times (E[b_n^2] + \sigma_\eta^2) / A_l^2}, \quad l = 1, 2 \quad (2.17)$$

$$P_l + \sum_{\substack{m=3 \\ m \neq l}}^4 \frac{P_m}{M + 4 \times (E[b_n^2] + \sigma_\eta^2) / A_l^2} \frac{e^{j(\Omega_m - \Omega_l)M} - 1}{1 - e^{-j(\Omega_m - \Omega_l)}} = \frac{1}{M + 4 \times (E[b_n^2] + \sigma_\eta^2) / A_l^2}, \quad l = 3, 4$$

Parameters $\{P_l\}$ can then be readily derived from these 2-by-2 equations for forward linear prediction. The minimum variance for forward prediction in equation (2.8) and forward-backward prediction in equation (2.10) are derived as the function of parameters $\{P_l\}$ respectively:

$$\begin{aligned} \min\{V_1\} &= E \left[\left(d_n - \sum_{i=1}^M a_i x_{n-i} \right)^2 \right] \\ &= E[d_n^2] - \sum_{i=1}^M 2a_i E[d_n x_{n-i}] + \sum_{j=1}^M \sum_{i=1}^M a_i a_j E[x_{n-j} x_{n-i}] \\ &= \frac{A_1^2 + A_2^2}{2} - \sum_{i=1}^M 2a_i E[d_n x_{n-i}] + \sum_{i=1}^M a_i E[d_n x_{n-i}] \\ &= \frac{A_1^2 + A_2^2}{2} - \sum_{i=1}^M \sum_{l=1}^4 P_l e^{j\Omega_l i} \left(\frac{A_1^2}{2} \cos(i\Omega_1) + \frac{A_2^2}{2} \cos(i\Omega_2) \right) \\ &= \frac{A_1^2 + A_2^2}{2} - \sum_{i=1}^M \sum_{l=1}^4 \sum_{k=1}^4 P_l e^{j\Omega_l i} \frac{A_k^2}{4} e^{j\Omega_k i} \\ &= \frac{A_1^2 + A_2^2}{2} - \sum_{l=1}^4 \frac{A_l^2 P_l M}{4} - \sum_{l=1}^4 \sum_{\substack{k=1 \\ |k-l| \neq 2}}^4 \frac{A_k^2 P_l}{4} \left[\frac{1 - e^{j(\Omega_l + \Omega_k)M}}{e^{-j(\Omega_l + \Omega_k)} - 1} \right] \end{aligned} \quad (2.18)$$

$$\begin{aligned} \min\{V_2\} &= \varepsilon_1^2 - \left(\sum_{l=1}^4 \frac{A_l^2 P_l M}{8} + \sum_{l=1}^4 \sum_{\substack{k=1 \\ |k-l| \neq 2}}^4 \frac{A_k^2 P_l}{8} \left[\frac{1 - e^{-j(\Omega_l + \Omega_k)M}}{e^{-j(\Omega_l + \Omega_k)} - 1} \right] \right) + \dots \\ &\left(\sum_{l=1}^4 \sum_{r=1}^4 \sum_{k=1}^4 \frac{A_k^2 P_l P_r}{8} \left(\sum_{n_1=1}^M e^{j(\Omega_l + \Omega_k) n_1} \right) \left(\sum_{n_2=1}^M e^{j(\Omega_k - \Omega_r) n_2} \right) \right) \end{aligned} \quad (2.19)$$

Similarly substituting (2.15) and (2.16) into (2.13) and equating coefficients of $\exp(j\Omega_l k)$ in the resulting equations leads to

$$\begin{aligned}
\text{Left} &= \sum_{i=1}^M a_i E[(x_{n-i} + x_{n+i})(x_{n-k} + x_{n+k})] \\
&= \sum_{i=1}^M a_i \{E[x_{n-i}x_{n-k}] + E[x_{n+i}x_{n-k}] + E[x_{n-i}x_{n+k}] + E[x_{n+i}x_{n+k}]\} \\
&= \sum_{i=1}^M \sum_{l=1}^4 P_l e^{j\Omega_l i} \{E[x_{n-i}x_{n-k}] + E[x_{n+i}x_{n-k}] + E[x_{n-i}x_{n+k}] + E[x_{n+i}x_{n+k}]\} \\
&= \sum_{l=1}^4 \frac{e^{jk\Omega_l}}{4} \left(2MA_l^2 P_l + \sum_{\substack{m=1 \\ m \neq l}}^4 A_l^2 P_m \frac{e^{j(\Omega_m - \Omega_l)M} - 1}{1 - e^{-j(\Omega_m - \Omega_l)}} + \sum_{\substack{m=1 \\ |m-l| \neq 2}}^4 A_l^2 P_m \frac{e^{j(\Omega_m + \Omega_l)M} - 1}{1 - e^{-j(\Omega_m + \Omega_l)}} + 4P_l (E[b_n^2] + \sigma_\eta^2) \right) \\
&\quad \dots + \sum_{l=1}^4 \frac{e^{-jk\Omega_l}}{4} \left(2MA_l^2 P_l + \sum_{\substack{m=1 \\ m \neq l}}^4 A_l^2 P_m \frac{e^{j(\Omega_m - \Omega_l)M} - 1}{1 - e^{-j(\Omega_m - \Omega_l)}} + \sum_{\substack{m=1 \\ |m-l| \neq 2}}^4 A_l^2 P_m \frac{e^{j(\Omega_m + \Omega_l)M} - 1}{1 - e^{-j(\Omega_m + \Omega_l)}} + 4P_l (E[b_n^2] + \sigma_\eta^2) \right)
\end{aligned}$$

$$\text{Right} = E[d_n(x_{n-k} + x_{n+k})] = \sum_{l=1}^4 \frac{A_l^2}{4} e^{jk\Omega_l} + \sum_{l=1}^4 \frac{A_l^2}{4} e^{-jk\Omega_l}$$

Left = Right

$$\begin{aligned}
\Rightarrow P_l + \sum_{\substack{m=1 \\ m \neq l}}^4 \frac{P_m}{2M + 4(E[b_n^2] + \sigma_\eta^2)/A_l^2} \left(\frac{e^{j(\Omega_m - \Omega_l)M} - 1}{1 - e^{-j(\Omega_m - \Omega_l)}} \right) + \sum_{\substack{m=1 \\ |m-l| \neq 2}}^4 \frac{P_m}{2M + 4(E[b_n^2] + \sigma_\eta^2)/A_l^2} \left(\frac{e^{j(\Omega_m + \Omega_l)M} - 1}{1 - e^{-j(\Omega_m + \Omega_l)}} \right) \\
= \frac{1}{2M + 4(E[b_n^2] + \sigma_\eta^2)/A_l^2}
\end{aligned}$$

The optimum parameters $\{P_l\}$ for block prediction can be solved through eliminating the negative correlated term and then converting the upper 4-by-4 linear equations into 2-by-2 equations in the same way as (2.17). It can be observed that the optimum solutions for parameter (a_k) estimation from MMSE are different for forward prediction and block prediction. The minimum variance for block linear prediction in equation (2.11) becomes

$$\min\{V_3\} = \frac{A_1^2 + A_2^2}{2} - \sum_{l=1}^4 \sum_{\substack{k=1 \\ |k-l| \neq 2}}^4 \frac{A_k^2 P_l}{4} \left(\frac{e^{j(\Omega_k + \Omega_l)M} - 1}{1 - e^{-j(\Omega_k + \Omega_l)}} \right) - \sum_{l=1}^4 \sum_{\substack{k=1 \\ k \neq l}}^4 \frac{P_l A_k^2}{4} \left(\frac{e^{j(\Omega_k - \Omega_l)M} - 1}{1 - e^{-j(\Omega_k - \Omega_l)}} \right) - \sum_{l=1}^4 \frac{MP_l A_l^2}{2} \quad (2.20)$$

Simulations

With the derived minimum variance we can study the comparative performances for the three data estimation structures with simulations; listed as follows, all possible impacted parameters are fixed except the filter length M :

$$E[b_n^2]/A_1^2 = 10dB, E[b_n^2]/A_2^2 = 20dB, E[b_n^2]/\sigma_\eta^2 = 30dB, \Omega_1 = 0.76\pi, \Omega_2 = 0.82\pi$$

Assuming that the same value is used for filter length M in both forward and backward filters, it can be observed in Figure 2-9 that the block prediction estimation performs better than the other two predictors under the same SNR situation. The ripple depth of those curves in Figure 2-9 is impacted by some parameters, i.e. the Bragg-lines frequency difference as shown in Figure 2-10 and SNR as shown in Figure 2-11. However compared to the block prediction during parameter estimation, the forward-backward prediction has less computation complexity.

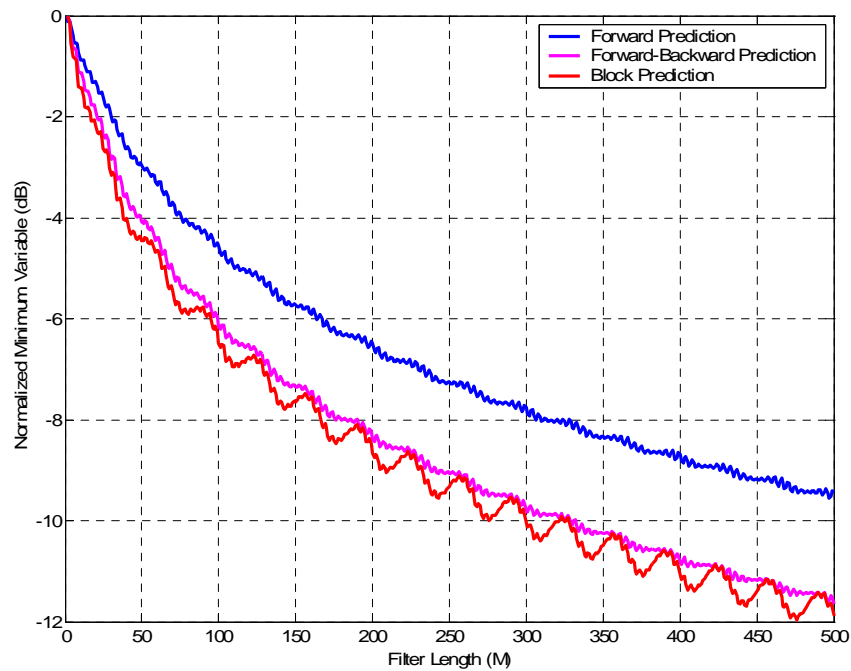


Figure 2-9 Normalized Minimum Variance of three linear predictions

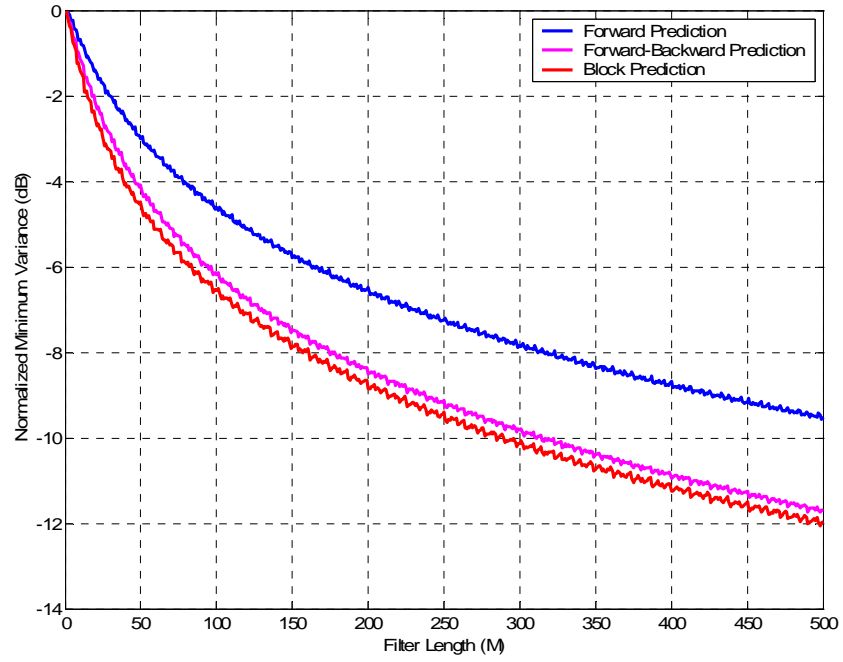


Figure 2-10 Normalized Minimum Variance of three linear predictions (The same assumption as Figure 2-9 except for $\Omega_1 = 0.61\pi, \Omega_2 = 0.92\pi$)

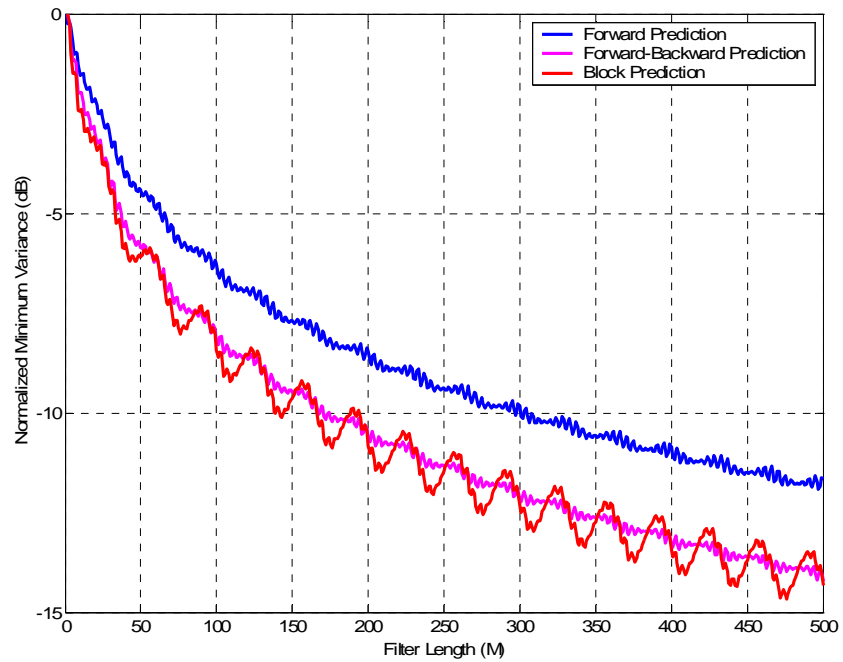


Figure 2-11 Normalized Minimum Variance of three linear predictions (The same assumption as Figure 2-9 except for $E[b_n^2]/\sigma_\eta^2 = 27dB$)

2.4 Further Interpolation and Improvement

2.4.1 Signal Enhancement

Signal property mapping takes advantage of the prescribed property of the desired signal and modifies the measured signal slightly to achieve signal enhancement. Therefore the enhanced signal would have a better representation of the underlying signal than that of the original measured one. The measured signal can be in the form of either vector (1-D) or matrix (2-D). For example the underlying matrix signal could have some theoretical property such as Toeplitz/Hankel structure, or positive semi-definite; however the imperfect measurement process causes the loss of some or even all of these properties. It is meaningful and possible to seek for an optimal signal which possesses the desired properties as the underlying signal and at the same time has the minimum distance to the underlying one. In other words this signal property mapping is a de-noising process based on the underlying signal's special properties.

We can take advantage of the signal mapping methodology to further improve the performance of the existing linear prediction estimations. As we know, the prediction parameters are estimated from the product of inverse of the autocorrelation matrix and the cross correlation vector. The autocorrelation matrix is supposed to be a Hermitian-Toeplitz and positive definite matrix. With the measurement noise and limited data, the measured autocorrelation matrix may not be Toeplitz any more and therefore impact the prediction performance. The proposed composite property mapping method [118] contains the Toeplitz property and rank p property mapping according to autocorrelation matrix's various properties.

The Toeplitz property mapping [118] is a linear transformation to the closest Toeplitz matrix for the underlying signal. The autocorrelation matrix is first partitioned and concatenated into column vector format by linear transformation $\boldsymbol{\gamma} = T[\mathbf{R}]$. Due to the Toeplitz/Hankel nature, the vector presentation can be fully expressed by matrix's first/last column and first row elements as

$$\boldsymbol{\gamma} = \mathbf{A}\boldsymbol{\phi}$$

where \mathbf{A} is an $M^2 \times (2M - 1)$ characteristic matrix and $\boldsymbol{\phi}$ is a $(2M - 1) \times 1$ vector which contains the independent auto-correlation coefficients (M is the linear prediction order). Through minimizing the Euclidean norm $\|\boldsymbol{\gamma} - \mathbf{A}\boldsymbol{\phi}\|$, the optimal solution is found to be

$$\boldsymbol{\phi} = [\mathbf{A}^T \mathbf{A}]^{-1} \mathbf{A}^T \boldsymbol{\gamma}$$

Then the Toeplitz property mapping for autocorrelation matrix \mathbf{R} is

$$\mathbf{R}_A = T^{-1} \left[\mathbf{A} [\mathbf{A}^T \mathbf{A}]^{-1} \mathbf{A}^T T[\mathbf{R}] \right]$$

The rank p property mapping [119] to be used for the covariance matrix corresponds to the known fact that the signal model has prescribed low-rank $p < M$; the covariance matrix also reflects the known uncorrelated additive white noise interference. In other words the energy of noise spreads over the whole observation space while the energy of the signal components is concentrated in a size p subspace. The mapping nulls the noise only subspace and removes the noise contribution in the signal subspace. The singular value decomposition (SVD) provides an orthogonal decomposition representation for this class of matrices. The SVD representation of matrix \mathbf{R} is

$$\mathbf{R} = \sum_{k=1}^M \sigma_k \mathbf{u}_k \mathbf{v}_k^H$$

where the σ_k are real nonnegative singular values which are ordered in the monotonically non-increasing fashion $\sigma_k \geq \sigma_{k+1}$, and the \mathbf{u}_k and \mathbf{v}_k are the corresponding $M \times 1$ orthonormal left and right singular vectors, respectively. The signal can be easily enhanced through nulling its components in noise subspace and modifying the signal subspace with suitable parameter $\{g_k, 0 \leq k \leq p\}$

$$\mathbf{R}_{(p)} = \sum_{k=1}^p g_k \sigma_k \mathbf{u}_k \mathbf{v}_k^H$$

Based on different optimization criteria, i.e. least square, minimum variance and time-domain constrained, the corresponding weight elements g_k are different as well. The performance analysis for these various weight elements are listed in [119]. For simplicity the weights can be chosen

$$g_k = \frac{\sigma_k - \frac{1}{M-p} \sum_{i=p+1}^M \sigma_i}{\sigma_k}$$

and then the rank p property mapping is defined as

$$\mathbf{R}_{(p)} = \sum_{k=1}^p \left(\sigma_k - \frac{1}{M-p} \sum_{i=p+1}^M \sigma_i \right) \mathbf{u}_k \mathbf{v}_k^H$$

So the composite property mapping can be formed by these two linear transformations as

$$\mathbf{R}_{c1} = F_{(p)}(F_A(\mathbf{R})) \text{ or } \mathbf{R}_{c2} = F_A(F_{(p)}(\mathbf{R}))$$

where $F_A(\cdot)$, $F_{(p)}(\cdot)$ are the formations of Toeplitz mapping and rank p mapping respectively.

To test the potential benefit of the two composite property mapping algorithm, the simulated signal model is generated as

$$x_n = A_1 e^{-j\Omega_1 n + \theta_1} + A_2 e^{j\Omega_2 n + \theta_2} + \eta_n + b_n$$

where $\{A_i, \Omega_i, \theta_i\}$ are defined as the amplitude, frequency and initial phase of the two simulated Bragg lines. η_n is white noise while b_n is the assumed impulsive noise which exists in short time period of the time sequence. The additive white noise variance is selected to ensure the SNR during prediction parameter estimation is adjustable (from 1dB to 40dB). The number of snapshots used is 300. The simulation results are shown in Figure 2-12. It can be observed that for low SNR signal enhancements outperform traditional linear prediction. For high SNR the signal enhancements add perturbation noise from the mapping process and perform slightly worse than the linear prediction method, but elsewhere significant gains are evident.

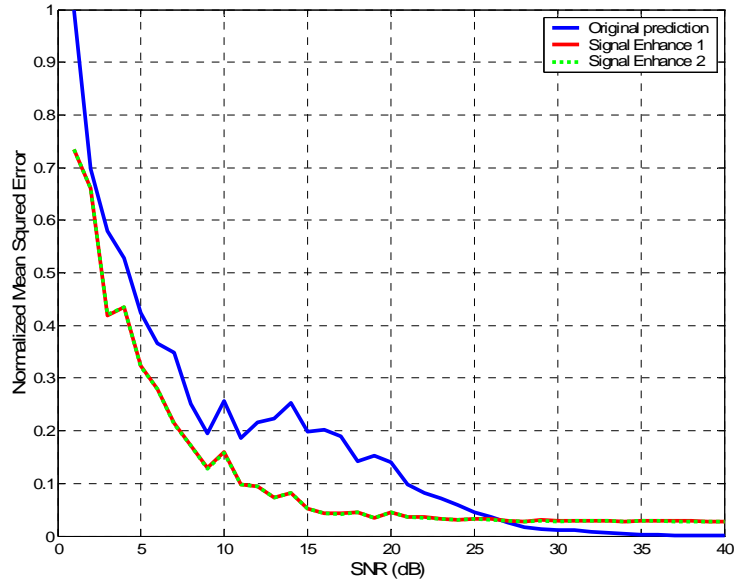


Figure 2-12 The signal enhancements performance comparison for forward linear prediction simulation. Signal enhance 1: $\mathbf{R}_{c1} = F_{(p)}(F_A(\mathbf{R}))$; signal enhance 2: $\mathbf{R}_{c2} = F_A(F_{(p)}(\mathbf{R}))$.

2.4.2 Theoretical Extension

From another point of view the whole data set including past segment, current missing/corrupted segment and future segment can be considered as one multi-variety Gaussian distribution with mean vector \mathbf{m} and variance matrix \mathbf{R} . In this section we show that all three linear prediction methods can be extracted from one general formulation, and their theoretical performances can be readily compared.

$$\begin{bmatrix} \mathbf{x}_p \\ \mathbf{x}_m \\ \mathbf{x}_f \end{bmatrix} \sim normal[\mathbf{m}, \mathbf{R}] \quad (2.21)$$

where

$$\begin{aligned} \mathbf{x}_p &\sim normal[\mathbf{m}_p, \mathbf{R}_p] \\ \mathbf{x}_m &\sim normal[\mathbf{m}_m, \mathbf{R}_m] \\ \mathbf{x}_f &\sim normal[\mathbf{m}_f, \mathbf{R}_f] \\ \mathbf{m} &= \begin{bmatrix} \mathbf{m}_p \\ \mathbf{m}_m \\ \mathbf{m}_f \end{bmatrix}, \quad \mathbf{R} = \begin{bmatrix} \mathbf{R}_p & \mathbf{R}_{pm} & \mathbf{R}_{pf} \\ \mathbf{R}_{pm}^H & \mathbf{R}_m & \mathbf{R}_{mf} \\ \mathbf{R}_{pf}^H & \mathbf{R}_{mf}^H & \mathbf{R}_f \end{bmatrix}. \end{aligned}$$

The lengths of \mathbf{x}_p , \mathbf{x}_m and \mathbf{x}_f are N_p , N_m and N_f , respectively. Without loss of generality,

we can change the data order during derivation as

$$\begin{bmatrix} \mathbf{x}_m \\ \mathbf{x}_p \\ \mathbf{x}_f \end{bmatrix} \sim normal[\ddot{\mathbf{m}}, \ddot{\mathbf{R}}] \quad (2.22)$$

where

$$\ddot{\mathbf{m}} = \begin{bmatrix} \mathbf{m}_m \\ \mathbf{m}_p \\ \mathbf{m}_f \end{bmatrix}, \quad \ddot{\mathbf{R}} = \begin{bmatrix} \mathbf{R}_m & \mathbf{R}_{pm}^H & \mathbf{R}_{mf} \\ \mathbf{R}_{pm} & \mathbf{R}_p & \mathbf{R}_{pf} \\ \mathbf{R}_{mf}^H & \mathbf{R}_{pf}^H & \mathbf{R}_f \end{bmatrix}$$

Then the conditional distribution can be written as follows:

$$\begin{aligned}
f(\mathbf{x}_m | \mathbf{x}_p, \mathbf{x}_f) &= \frac{f(\mathbf{x}_m, \mathbf{x}_p, \mathbf{x}_f)}{f(\mathbf{x}_p, \mathbf{x}_f)} \\
&= \frac{(2\pi)^{-N_m/2} (2\pi)^{-N_p/2} (2\pi)^{-N_f/2} |\ddot{\mathbf{R}}|^{-1/2} \exp \left\{ -(1/2) \left\{ \begin{bmatrix} \mathbf{x}_m \\ \mathbf{x}_p \\ \mathbf{x}_f \end{bmatrix} - \ddot{\mathbf{m}} \right\}^T \ddot{\mathbf{R}}^{-1} \left\{ \begin{bmatrix} \mathbf{x}_m \\ \mathbf{x}_p \\ \mathbf{x}_f \end{bmatrix} - \ddot{\mathbf{m}} \right\} \right\}}{(2\pi)^{-N_p/2} (2\pi)^{-N_f/2} \begin{vmatrix} \mathbf{R}_p & \mathbf{R}_{pf} \\ \mathbf{R}_{pf}^H & \mathbf{R}_f \end{vmatrix}^{-1/2} \exp \left\{ -(1/2) \left\{ \begin{bmatrix} \mathbf{x}_p \\ \mathbf{x}_f \end{bmatrix} - \begin{bmatrix} \mathbf{m}_p \\ \mathbf{m}_f \end{bmatrix} \right\}^T \begin{bmatrix} \mathbf{R}_p & \mathbf{R}_{pf} \\ \mathbf{R}_{pf}^H & \mathbf{R}_f \end{bmatrix}^{-1} \left\{ \begin{bmatrix} \mathbf{x}_p \\ \mathbf{x}_f \end{bmatrix} - \begin{bmatrix} \mathbf{m}_p \\ \mathbf{m}_f \end{bmatrix} \right\} \right\}}
\end{aligned} \tag{2.23}$$

Based on the Partitioned Matrix Inverse Theorem [117], the inversion of the variance is described as

$$\begin{aligned}
\ddot{\mathbf{R}}^{-1} &= \begin{bmatrix} \mathbf{0}_{N_m \times N_m} & \mathbf{0}_{N_m \times (N_p + N_f)} \\ \mathbf{0}_{(N_p + N_f) \times N_m} & \mathbf{A}^{-1} \end{bmatrix} + \begin{bmatrix} \mathbf{I}_{N_m \times N_m} \\ -\mathbf{A}^{-1} \begin{bmatrix} \mathbf{R}_{pm} \\ \mathbf{R}_{mf}^H \end{bmatrix} \end{bmatrix} \left[\mathbf{Q}^{-1} \right] \begin{bmatrix} \mathbf{I}_{N_m \times N_m} & -(\mathbf{R}_{pm}^H \ \mathbf{R}_{mf}) \mathbf{A}^{-1} \end{bmatrix} \\
\mathbf{A}^{-1} &= \begin{bmatrix} \mathbf{R}_p & \mathbf{R}_{pf} \\ \mathbf{R}_{pf}^H & \mathbf{R}_f \end{bmatrix}^{-1} \\
\mathbf{Q} &= \mathbf{R}_m - \begin{bmatrix} \mathbf{R}_{pm}^H & \mathbf{R}_{mf} \end{bmatrix} \mathbf{A}^{-1} \begin{bmatrix} \mathbf{R}_{pm} \\ \mathbf{R}_{mf}^H \end{bmatrix}
\end{aligned} \tag{2.24}$$

The corresponding determinant is

$$|\ddot{\mathbf{R}}| = |\mathbf{A}| |\mathbf{Q}|$$

Substituting equation (2.24) into the conditional density (2.23), the resulting formula is also Gaussian. So the conditional distribution of \mathbf{x}_m , given $\mathbf{x}_p, \mathbf{x}_f$, is multivariate normal

$$f(\mathbf{x}_m | \mathbf{x}_p, \mathbf{x}_f) \sim \text{normal}[\hat{\mathbf{x}}_m, \mathbf{P}]$$

with conditional mean

$$\hat{\mathbf{x}}_m = \mathbf{m}_m + \begin{bmatrix} \mathbf{R}_{pm}^H & \mathbf{R}_{mf} \end{bmatrix} \begin{bmatrix} \mathbf{R}_p & \mathbf{R}_{pf} \\ \mathbf{R}_{pf}^H & \mathbf{R}_f \end{bmatrix}^{-1} \begin{bmatrix} \mathbf{x}_p - \mathbf{m}_p \\ \mathbf{x}_f - \mathbf{m}_f \end{bmatrix} \tag{2.25}$$

and conditional covariance

$$\mathbf{P} = \mathbf{R}_m - \begin{bmatrix} \mathbf{R}_{pm}^H & \mathbf{R}_{mf} \end{bmatrix} \begin{bmatrix} \mathbf{R}_p & \mathbf{R}_{pf} \\ \mathbf{R}_{pf}^H & \mathbf{R}_f \end{bmatrix}^{-1} \begin{bmatrix} \mathbf{R}_{pm} \\ \mathbf{R}_{mf}^H \end{bmatrix}. \tag{2.26}$$

From this general formulation we can derive the corresponding Gaussian distribution for the proposed predictions as follows:

Forward linear prediction:

$$\begin{aligned} f(\mathbf{x}_m | \mathbf{x}_p) &\sim \text{normal}\left(\mathbf{m}_m + \mathbf{R}_{pm}^H \mathbf{R}_p^{-1} (\mathbf{x}_p - \mathbf{m}_p), \mathbf{R}_m - \mathbf{R}_{pm}^H \mathbf{R}_p^{-1} \mathbf{R}_{pm}\right) \\ &\sim \text{normal}(\hat{\mathbf{x}}_{m,1}, \mathbf{P}_1) \end{aligned} \quad (2.27)$$

Forward-backward linear prediction:

$$\begin{aligned} f(\mathbf{x}_m | \mathbf{x}_p, \mathbf{x}_f) &\sim \text{normal}\left(\mathbf{m}_m + \begin{bmatrix} \mathbf{R}_{pm}^H & \mathbf{R}_{mf} \end{bmatrix} \begin{bmatrix} \mathbf{R}_p & \mathbf{0} \\ \mathbf{0} & \mathbf{R}_f \end{bmatrix}^{-1} \begin{bmatrix} \mathbf{x}_p - \mathbf{m}_p \\ \mathbf{x}_f - \mathbf{m}_f \end{bmatrix}, \mathbf{R}_m - \begin{bmatrix} \mathbf{R}_{pm}^H & \mathbf{R}_{mf} \end{bmatrix} \begin{bmatrix} \mathbf{R}_p & \mathbf{0} \\ \mathbf{0} & \mathbf{R}_f \end{bmatrix}^{-1} \begin{bmatrix} \mathbf{R}_{pm} \\ \mathbf{R}_{mf}^H \end{bmatrix}\right) \\ &\sim \text{normal}(\hat{\mathbf{x}}_{m,2}, \mathbf{P}_2) \end{aligned} \quad (2.28)$$

Block linear prediction:

$$\begin{aligned} f(\mathbf{x}_m | \mathbf{x}_p, \mathbf{x}_f) &\sim \text{normal}\left(\mathbf{m}_m + \begin{bmatrix} \mathbf{R}_{pm}^H & \mathbf{R}_{mf} \end{bmatrix} \begin{bmatrix} \mathbf{R}_p & \mathbf{R}_{pf} \\ \mathbf{R}_{pf}^H & \mathbf{R}_f \end{bmatrix}^{-1} \begin{bmatrix} \mathbf{x}_p - \mathbf{m}_p \\ \mathbf{x}_f - \mathbf{m}_f \end{bmatrix}, \mathbf{R}_m - \begin{bmatrix} \mathbf{R}_{pm}^H & \mathbf{R}_{mf} \end{bmatrix} \begin{bmatrix} \mathbf{R}_p & \mathbf{R}_{pf} \\ \mathbf{R}_{pf}^H & \mathbf{R}_f \end{bmatrix}^{-1} \begin{bmatrix} \mathbf{R}_{pm} \\ \mathbf{R}_{mf}^H \end{bmatrix}\right) \\ &\sim \text{normal}(\hat{\mathbf{x}}_{m,3}, \mathbf{P}_3) \end{aligned} \quad (2.29)$$

There are several remarkable properties of the estimator $\hat{\mathbf{x}}_{m,k}$ and the error $\hat{\mathbf{n}}_k = \mathbf{x}_m - \hat{\mathbf{x}}_{m,k}$.

Firstly the estimator $\hat{\mathbf{x}}_{m,k}$ is Gaussian with the same mean \mathbf{m}_m as \mathbf{x}_m and covariance matrix $\hat{\mathbf{P}}_k$ as the forward, forward-backward, and block linear predictors are respectively:

$$\hat{\mathbf{P}}_1 = E\left[(\hat{\mathbf{x}}_{m,1} - \mathbf{m}_m)(\hat{\mathbf{x}}_{m,1} - \mathbf{m}_m)^H\right] = \mathbf{R}_{pm}^H \mathbf{R}_p^{-1} \mathbf{R}_{pm} \quad (2.30)$$

$$\hat{\mathbf{P}}_2 = E\left[(\hat{\mathbf{x}}_{m,2} - \mathbf{m}_m)(\hat{\mathbf{x}}_{m,2} - \mathbf{m}_m)^H\right] = \begin{bmatrix} \mathbf{R}_{pm}^H & \mathbf{R}_{mf} \end{bmatrix} \begin{bmatrix} \mathbf{R}_p & \mathbf{0} \\ \mathbf{0} & \mathbf{R}_f \end{bmatrix}^{-1} \begin{bmatrix} \mathbf{R}_{pm} \\ \mathbf{R}_{mf}^H \end{bmatrix} \quad (2.31)$$

$$\hat{\mathbf{P}}_3 = E\left[(\hat{\mathbf{x}}_{m,3} - \mathbf{m}_m)(\hat{\mathbf{x}}_{m,3} - \mathbf{m}_m)^H\right] = \begin{bmatrix} \mathbf{R}_{pm}^H & \mathbf{R}_{mf} \end{bmatrix} \begin{bmatrix} \mathbf{R}_p & \mathbf{R}_{pf} \\ \mathbf{R}_{pf}^H & \mathbf{R}_f \end{bmatrix}^{-1} \begin{bmatrix} \mathbf{R}_{pm} \\ \mathbf{R}_{mf}^H \end{bmatrix} \quad (2.32)$$

Secondly the error $\hat{\mathbf{n}}_k$ is Gaussian with zero mean and covariance matrix $\tilde{\mathbf{P}}_k$ as follows:

$$\begin{aligned}
\tilde{\mathbf{P}}_1 &= E\left[(\mathbf{x}_m - \hat{\mathbf{x}}_{m,1})(\mathbf{x}_m - \hat{\mathbf{x}}_{m,1})^H\right] \\
&= \mathbf{R}_m - \mathbf{R}_{pm}^H \mathbf{R}_p^{-1} \mathbf{R}_{pm} \\
&= \mathbf{P}_1
\end{aligned} \tag{2.33}$$

$$\begin{aligned}
\tilde{\mathbf{P}}_2 &= E\left[(\mathbf{x}_m - \hat{\mathbf{x}}_{m,2})(\mathbf{x}_m - \hat{\mathbf{x}}_{m,2})^H\right] \\
&= \mathbf{R}_m - \mathbf{R}_{pm}^H \mathbf{R}_p^{-1} \mathbf{R}_{pm} - \mathbf{R}_{mf}^H \mathbf{R}_f^{-1} \mathbf{R}_{mf} \\
&= \mathbf{P}_2
\end{aligned} \tag{2.34}$$

$$\begin{aligned}
\tilde{\mathbf{P}}_3 &= E\left[(\mathbf{x}_m - \hat{\mathbf{x}}_{m,3})(\mathbf{x}_m - \hat{\mathbf{x}}_{m,3})^H\right] \\
&= \mathbf{R}_m - \begin{bmatrix} \mathbf{R}_{pm}^H & \mathbf{R}_{mf}^H \end{bmatrix} \begin{bmatrix} \mathbf{R}_p & \mathbf{R}_{pf} \\ \mathbf{R}_{pf}^H & \mathbf{R}_f \end{bmatrix}^{-1} \begin{bmatrix} \mathbf{R}_{pm} \\ \mathbf{R}_{mf}^H \end{bmatrix} \\
&= \mathbf{P}_3
\end{aligned} \tag{2.35}$$

It is observed that the error vector shares the same covariance matrix as \mathbf{x}_m . In one word the random vector \mathbf{x}_m has an orthogonal (or uncorrelated) representation under the form $\mathbf{x}_m = \hat{\mathbf{n}} + \hat{\mathbf{x}}_m$. The error vector describes the difference between the estimation $\hat{\mathbf{x}}_m$ and the real data \mathbf{x}_m . Its variance matrix is one criterion for measuring the estimation performance. The smaller the variance of the noise $\hat{\mathbf{n}}$, the better the estimation is. Considering the predictor covariances in equations (2.27), (2.28) and (2.29), we can easily conclude that block linear prediction and forward-backward linear prediction have the better estimation performance compared with the forward linear prediction method. Note that both residuals can be readily shown to be positive definite as shown by the following equations:

$$\text{trace}(\mathbf{P}_1) - \text{trace}(\mathbf{P}_2) = \text{trace}(\mathbf{P}_1 - \mathbf{P}_2) = \text{trace}(\mathbf{R}_{mf} \mathbf{R}_f^{-1} \mathbf{R}_{mf}^H) > 0$$

$$\text{trace}(\mathbf{P}_1) - \text{trace}(\mathbf{P}_3) = \text{trace}(\mathbf{P}_1 - \mathbf{P}_3) = \text{trace}\left(\begin{bmatrix} \mathbf{R}_{pm}^H & \mathbf{R}_{mf}^H \end{bmatrix} \begin{bmatrix} \mathbf{R}_p & \mathbf{R}_{pf} \\ \mathbf{R}_{pf}^H & \mathbf{R}_f \end{bmatrix}^{-1} \begin{bmatrix} \mathbf{R}_{pm} \\ \mathbf{R}_{mf}^H \end{bmatrix} - \mathbf{R}_{mf} \mathbf{R}_f^{-1} \mathbf{R}_{mf}^H\right) > 0$$

It is not straightforward to compare the performances of block linear prediction and forward-backward linear prediction. However as shown in [117] and [129], the non-zero cross covariance information in block linear prediction helps to further improve the estimation accuracy. The conclusion obtained in this section is consistent with the one obtained from section 2.3.

2.5 Section Conclusion

We have presented an effective excision method that detects and removes impulsive noise without disturbing the underlying signal in order to improve the detection sensitivity of the range-Doppler image. The forward-backward and block predictors, the key points of our algorithm, not only smoothly update those abnormal impulsive points without frequency leakage but also correct the errors caused by a non-optimal threshold. A real time implementation of our algorithm is feasible and underway. The real experimental data verifies the effectiveness of our methods in improving the SNR and enhancing the target detectability. Further the minimum variance is proposed as the performance standard and the corresponding minimum variance error of those prediction methods have been derived theoretically for our impulsive noise problem. The block prediction method has been shown to have the best performance not only from minimum variance criteria but also from the covariance matrix orthogonal decomposition for the conditional probability distribution. Signal property mapping has been applied on the estimated covariance matrix to further improve the prediction performance especially for weak signal. The improvements afforded by the signal enhancement mapping are about 3

dB for low signal to noise ratio at the expense of extra computation of SVD and matrix multiplications.

Chapter 3 - Sidelobe Control in Adaptive Beamforming

3.1 Introduction

The purpose of adaptive beamforming is to apply a scaling weight to each of an array's sensor outputs in such a way that their linear weighted combination in effect steers the array's beam in a desired direction while blindly learning and then attenuating interference and background clutter from other directions. The signals of interest can be detected and localized by measuring the beamformed sensor output power. Adaptive beamforming has been applied to a wide variety of civil and military systems such as radar, sonar, wireless communication and seismology [16][17][18][19][20].

In general there are three different optimality criteria [21] adopted for weights' estimation in adaptive beamforming: the least mean square error, the maximum SNR and minimum variance distortionless response (MVDR). However their solutions only differ by a gain scalar in steady state, and in this chapter we will consider sidelobe control for the most popular MVDR.

The MVDR beamformer [15][22], also known as Capon's beamformer, minimizes the array output power while maintaining a fixed gain in the directions of the desired signals.

Although a beampattern would be free of high sidelobes when computed using the true covariance matrix, sidelobes are definitely an issue when any practical sample covariance matrix is used. Through high sidelobes, non-stationary clutter or reverberation will increase the false detection probability, and a pulsed jammer can interfere with the system and reduce the ideal signal detection probability. Due to the non-stationary background of sea clutter and transient co-channel interference [1], false detection is a serious problem in HF radar even when large amount of received data are available to estimate the covariance matrix.

Due to the importance of the sidelobe control in adaptive beamforming, much relevant work has been contributed in recent years. The diagonal loading method [23][24] is an effective and simple approach to suppress sidelobes. By adding a small number on the diagonal of the covariance matrix, the algorithm becomes robust against small time varying interferences. However there is no closed form solution for the loading value, which is generally set by simulation trial or empirical experience. The statistical performance analysis of MVDR with diagonal loading can be found in [25]. A linearly constrained minimum power (LCMP) beamformer is developed in [26][27] under quadratic beam-weights constraints with adaptive implementation, which is equivalent to an adaptive diagonal loading method with the loading value iteratively updated. Although LCMP solves the loading value set problem, it can not guarantee the convergence in a satisfactory finite number of iterations.

A penalty function (PF) has been proposed [28][29] and included in the MVDR beamformer in order to force the adaptive beampattern to follow the low sidelobe quiescent (such as Dolph-Tchebychev) beampattern in the sidelobe region. An alternative,

presented in [30] and based on QR decomposition, decreases the algorithm's computational complexity and improves the stability compared to the original PF method. There are other methods based on subspace projection [31][32][33] to suppress the sidelobe levels, however the results are not promising.

None of the above discussed methods can guarantee that the sidelobes remain below a desired level even if such solutions exist. Multiple hard quadratic constraints outside of the mainbeam are proposed in [34] to ensure that all the sidelobes are below an expected level when the optimization problem is feasible. The method is realized by a second order cone (SOC) program [35], for which there is a fast and efficient (in polynomial time) tool called SeDuMi [35]. However a hard threshold needs to be pre-chosen by ad hoc trials with the consideration that it should not be too tight or too slack in order to keep the problem feasible and the constraints active. As the number of interferences increases, it is hard to find the threshold solution and then an infeasible and non-meaningful solution is possible.

As a means of changing the preset parameter into one optimization variable, we propose a new approach for obtaining the optimal threshold for the sidelobe pattern control without requiring any prior information. The MVDR objective function is reformulated by introducing a new weighted "penalty function" which is related to the threshold for the multiple quadratic constraints outside the mainlobe. The simulation and experimental results validate the improved performance and feasibility of our proposed method.

3.2 Array Signal Model and Adaptive Beamforming

In this section we give a brief description of the well-known array signal model and the conventional MVDR adaptive beamformer when incident narrowband plane-wave signals are impinging on the uniform linear array (ULA). Although the study is based on the ULA and narrowband signal assumptions, the results could be extended to other array structures and wideband signals. The convention adopted here is that bold lower-case letters denote vectors, and bold upper-case letters denote matrices. Superscript T and H denote transpose and conjugate transpose respectively.

3.2.1 Array Snapshot Model

Assuming that the receiving sensor array snapshot output at time instant t ($t = 1, 2, \dots, N$) is $\mathbf{x}(t) \in \mathbb{R}^m$ with m the number of sensors, then the traditional narrow-band array model [19] for far field planar incident waves is:

$$\mathbf{x}(t) = \mathbf{A}(\theta)\mathbf{s}(t) + \mathbf{n}(t) \quad (3.1)$$

where $\mathbf{s}(t) \in \mathbb{R}^k$ contains temporal signals reflected by the k non-coherent scattered sources and is uncorrelated with $\mathbf{n}(t) \in \mathbb{R}^m$, the additive spatially white noise vector. Although the sources are all due to targets that are reflecting the impinging transmitted pulses, there may be unwanted signals, i.e. interference. Matrix $\mathbf{A}(\theta) = [\mathbf{a}(\theta_1), \dots, \mathbf{a}(\theta_k)]$ contains the signal-plus-interference direction vectors of the associated sources, the i^{th} column of which is

$$\mathbf{a}(\theta_i) = \left[1, e^{-j2\pi \frac{d \sin(\theta_i)}{\lambda}}, \dots, e^{-j2\pi \frac{d \sin(\theta_i)}{\lambda} (m-1)} \right]^T \quad (3.2)$$

where θ_i is the direction of arrival (DOA) of the i^{th} source; λ and d are respectively the carrier wavelength and sensor spacing.

The array covariance matrix $\mathbf{R} \in \mathbb{R}^{m \times m}$ of the sensor output vector $\mathbf{x}(t)$ is

$$\mathbf{R} = E\{\mathbf{x}(t)\mathbf{x}^H(t)\} = \mathbf{A}(\theta)\mathbf{R}_{ss}\mathbf{A}(\theta)^H + \sigma^2\mathbf{I}_{m \times m} \quad (3.3)$$

where σ^2 is the common variance of noise vector $\mathbf{n}(t)$, \mathbf{R}_{ss} is signal-plus-interference covariance matrix with full rank and $E\{\cdot\}$ is the expectation operator. $\mathbf{I}_{m \times m}$ is the identity matrix with dimension m .

3.2.2 Conventional Adaptive Beamforming (MVDR)

Beamforming is a spatial domain filtering technique for localizing signal sources using antenna arrays. Those steering locations which result in maximum array output power yield the DOA estimates. The output of the beamformer is a linear combination of received data from all antennas. Let $y(t)$ be the beamformer output at time instant t and let \mathbf{w} be the m -by-1 complex weight vector; then we have:

$$y(t) = \mathbf{w}^H \mathbf{x}(t). \quad (3.4)$$

The array output power is measured by

$$P = E\left\{\left|\mathbf{w}^H \mathbf{x}\right|^2\right\} = \mathbf{w}^H \mathbf{R} \mathbf{w} \quad (3.5)$$

where \mathbf{R} is the array covariance matrix defined in Eq. (3.3). In practice, \mathbf{R} is usually unknown and can only be estimated from the sample covariance matrix

$$\hat{\mathbf{R}} = \frac{1}{N} \sum_{t=1}^N \mathbf{x}(t)\mathbf{x}^H(t) \quad (3.6)$$

In conventional digital beamforming the desired weight vector is the windowed and normalized steering vector and is not related with the array covariance matrix. In the

following adaptive beamforming, the desired weight vector is varied over time with the statistics of the received data set.

The MVDR beamformer minimizes the power contributed by noise and interference coming from other directions while maintaining a fixed gain in the direction of interest. The minimization problem can be formulated as follows:

$$\begin{aligned} \min_{\mathbf{w}} \quad & \mathbf{w}^H \mathbf{R} \mathbf{w} \\ \text{s.t.} \quad & \mathbf{w}^H \mathbf{a}_s = f \end{aligned} \quad (3.7)$$

where f is a constant number and usually set to 1, \mathbf{w} is the desired weight vector of the sensor array, and \mathbf{a}_s is the steering vector for the direction of interest. Symbol *s.t.* is acronym for subject to. By setting the gradient of the corresponding Lagrange function to be zero, the closed-form solution for the MVDR weights is

$$\mathbf{w} = \mathbf{R}^{-1} \mathbf{a}_s \left(\mathbf{a}_s^H \mathbf{R}^{-1} \mathbf{a}_s \right)^{-1} f \quad (3.8)$$

The highest peaks of the beamformer output power P as a function of the trial direction parameter become the estimates of the DOA parameters. The conventional MVDR beamformer may be adequate if we are only concerned with maximizing the SNR instead of detecting targets. In real radar and sonar systems, high sidelobe levels may increase the false detection probability due to non-stationary clutter or reverberation, and may reduce the correct signal detection probability due to pulsed jammer or interference. In conventional beamforming, low sidelobes are usually achieved by the application of window function (taper weights) on the array elements. But this ‘pre-windowing’ is not effective for adaptive arrays, for which the adaptive algorithm gives a beampattern which is identical to that obtained without the pre-windowing.

3.3 Sidelobe Control in Adaptive Beamforming

In this section we review several existing approaches and propose improved methods in adaptive beamforming to control the sidelobes. We first discuss the most general and robust method: diagonal loading. In fact many recently developed approaches could be categorized to be a specific example of the diagonal loading method. We then consider the PF methods; these add a penalty term in the objective function in order to force the sidelobes to follow a desired ‘quiescent’ beampattern. Finally we try to suppress the sidelobes by some constrained optimization algorithms.

3.3.1 Diagonal Loading

The diagonal loading technique [23] is used to compensate the antenna pattern distortion or mismatch, which also can suppress the high sidelobes due to small sample size. The idea is to add a small positive value δ to the diagonal elements of the array covariance matrix \mathbf{R} when computing the adaptive weights:

$$\mathbf{w} = (\mathbf{R} + \delta \mathbf{I}_{m \times m})^{-1} \mathbf{a}_s \left(\mathbf{a}_s^H (\mathbf{R} + \delta \mathbf{I}_{m \times m})^{-1} \mathbf{a}_s \right)^{-1} f \quad (3.9)$$

The working principle of diagonal loading can be better understood from the eigenspace point of view. As is well known, the signal-plus-interference subspace is composed of the sub-eigenspace corresponding to the largest eigenvalues of the covariance matrix, and the remaining ideally small and equal eigenvalues correspond to the so-called noise subspace. It has been shown [24] that the high sidelobes are due to the variation of the small eigenvalues of \mathbf{R} from the ideal constant noise level. Adding a small positive value to the diagonal of \mathbf{R} will minimally distort the signal and the interference nulling, but considerably suppress the noise eigenvalue spreading, thus desensitizing the system, and

giving robustness against small interference sources and small sample size. Therefore the sidelobes of the MVDR beampattern after diagonal loading are lower than those from the original MVDR. An example in Figure 3-1 shows the sidelobe suppression effect of the diagonal loading method with different loading factor values.

Alternative Quadratic Constrained Optimization Formulation

The MVDR with diagonal loading can be reformulated into a constrained optimization problem. It has been determined that the sensitivity of the MVDR beamformer to array perturbation or sample covariance matrix estimation error increases as the norm of \mathbf{w} increases [27]. This means that a quadratic constraint on the norm of \mathbf{w} could be introduced into MVDR to increase the algorithm's robustness, and the quadratic constrained MVDR is

$$\min_{\mathbf{w}} \mathbf{w}^H \mathbf{R} \mathbf{w} \quad s.t. \quad \mathbf{w}^H \mathbf{a}_s = f, \|\mathbf{w}\|_2^2 = T_0. \quad (3.10)$$

By using the Lagrange multiplier method, we obtain the optimal solution as

$$\mathbf{w} = (\mathbf{R} + \lambda_1 \mathbf{I}_{m \times m})^{-1} \mathbf{a}_s \left[\mathbf{a}_s^H (\mathbf{R} + \lambda_1 \mathbf{I}_{m \times m})^{-1} \mathbf{a}_s \right]^{-1} f \quad (3.11)$$

where λ_1 is determined by the pre-set value T_0 . Notice Eqs. (3.9) and (3.11). have the same form. Until now there has been no closed form expression for the optimal diagonal loading factor and it must be solved adaptively.

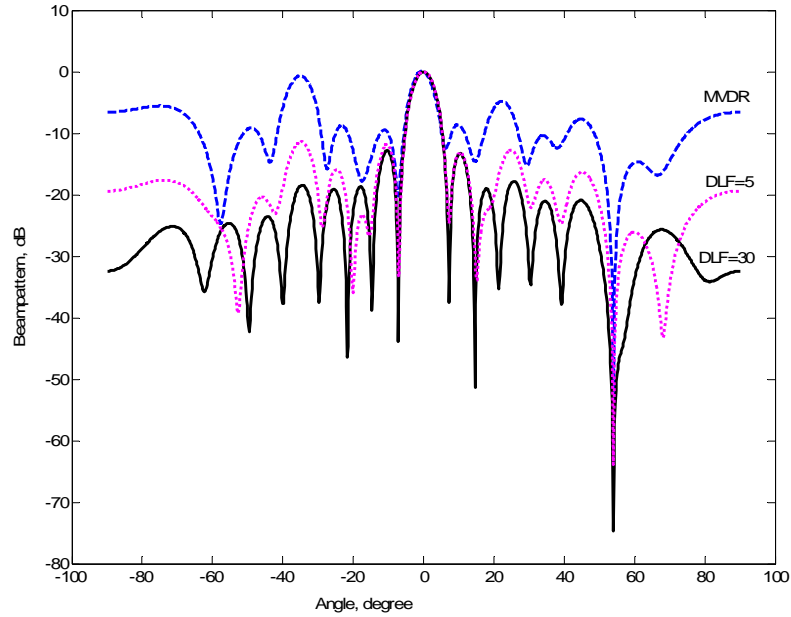


Figure 3-1 Beam patterns before and after diagonal loading; DLF means diagonal loading factor or value δ ; the sole desired signal is at 0° ; the sole interference is at 54°

3.3.2 Penalty Function Method

The PF method [28] provides a distance measure between a desired low sidelobe quiescent beampattern corresponding to the weight vector \mathbf{w}_q and the adaptively computed beampattern defined by the weight vector \mathbf{w} . The corresponding optimization problem can be formulated as

$$\min_{\mathbf{w}} \mathbf{w}^H \mathbf{R} \mathbf{w} + u^2 (\mathbf{w} - \mathbf{w}_q)^H \mathbf{Z} (\mathbf{w} - \mathbf{w}_q) \quad s.t. \quad \mathbf{w}^H \mathbf{a}_s = f \quad (3.12)$$

where u^2 is a non-negative scalar weighting factor, and the symmetric matrix \mathbf{Z} is defined as

$$\mathbf{Z} = \int_{-0.5\pi}^{0.5\pi} h(\theta) \mathbf{a}(\theta) \mathbf{a}^H(\theta) d\theta$$

where $h(\theta)$ is a suitable, non-negative weighting function to emphasize the beam pattern at angles θ outside of the mainbeam, and $\mathbf{a}(\theta)$ is defined as in Eq. (3.2). The optimal solution is

$$\mathbf{w} = (\mathbf{R} + u^2 \mathbf{Z})^{-1} (\lambda_0 \mathbf{a}_s + u^2 \mathbf{Z} \mathbf{w}_q) \quad (3.13)$$

and the closed form for the parameter λ_0 is:

$$\lambda_0 = \frac{f - u^2 \mathbf{a}_s^H (\mathbf{R} + u^2 \mathbf{Z})^{-1} \mathbf{Z} \mathbf{w}_q}{\mathbf{a}_s^H (\mathbf{R} + u^2 \mathbf{Z})^{-1} \mathbf{a}_s}$$

Furthermore the hard constraint in Eq. (3.12) can be replaced by a soft constraint as a second PF term:

$$\min_{\mathbf{w}} \mathbf{w}^H \mathbf{R} \mathbf{w} + u^2 (\mathbf{w} - \mathbf{w}_q)^H \mathbf{Z} (\mathbf{w} - \mathbf{w}_q) + \beta^2 \left| (\mathbf{w}^H \mathbf{a}_s - f) \right|^2 \quad (3.14)$$

where the scalar β^2 is a pre-chosen weight factor. Although the signal to interference and noise ratio (SINR) of the output is improved slightly, the gain in the look direction fluctuates around value f . Only when the weight β^2 is chosen to be infinite, the solution of Eq. (3.14) is the same as that of (3.12). The idea is to allow some small mainbeam distortion to obtain a better sidelobe pattern.

As we know, minimizing the output power in MVDR will alter the sidelobe's symmetric property and give deep nulls around the interference locations, which leads to an enlarged distance between the quiescent weight \mathbf{w}_q and the designed weight \mathbf{w} . It is unnecessary and inefficient to minimize this large distance in order to suppress the sidelobes. In fact the above PF methods have a potential disadvantage since they tend to weaken the interference nulling ability by raising the nulls up to the quiescent beam pattern. This results in lower SINR and has no advantage in suppressing sidelobes.

Better understanding is found in Figure 3-2. It is obvious that there is a big difference (distance) between the quiescence beampattern and adaptive beampattern around 54° where a strong interference is present. In original PF methods an attempt is made to reduce this distance as it is harmful in the sense of interference cancelling and makes the algorithm less efficient since some degrees of freedom are wasted without any gain in sidelobe control.

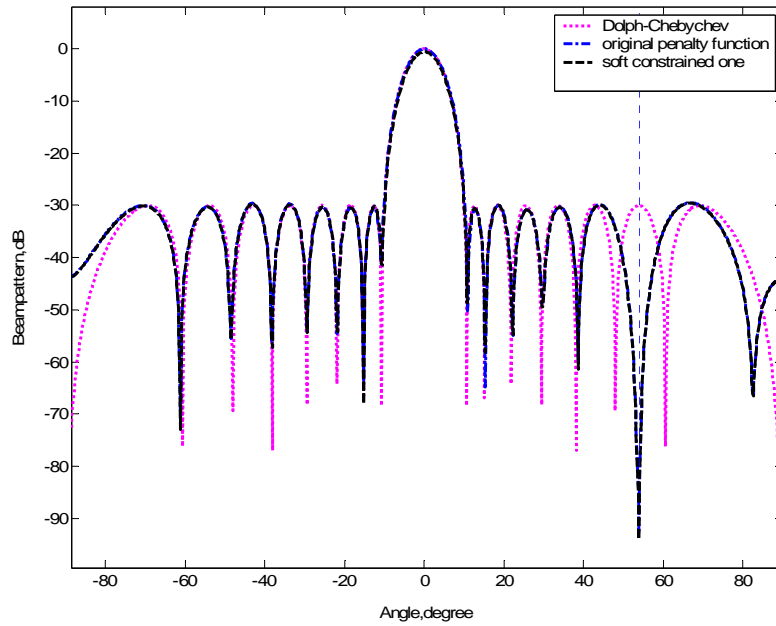


Figure 3-2 Performance comparison among different PF methods; dashed trace: soft constrained PF; dash-dot trace: original PF; dotted trace: quiescent beampattern

3.3.3 MVDR with Quadratic Inequality Constraints

In addition to the diagonal loading and PF methods, control of the sidelobes in MVDR can be achieved by adding a set of quadratic inequality constraints outside of the mainbeam. The formulation is

$$\min_{\mathbf{w}} \mathbf{w}^H \mathbf{R} \mathbf{w} \quad s.t. \quad \mathbf{w}^H \mathbf{a}_s = f$$

$$\left| \mathbf{w}^H \mathbf{a}(\theta_j) \right|^2 \leq \varepsilon^2 \quad \text{for } j = 1, 2, \dots, J \quad (3.15)$$

where $\{\mathbf{a}(\theta_j), j=1, \dots, J\}$ are the sampled steering vectors corresponding to a finite set of angles θ_j in the sidelobe region, parameters ε are the preset hard thresholds that set the desired sidelobe levels, and J is the total sample number. We call this approach the preset threshold discrete quadratic constrained optimization method (PT-DQC). There is no closed form solution for (3.15), and we resort to optimization algorithms to solve it. If an optimal solution is obtainable, the resulting sidelobes will be guaranteed to be no higher than the prescribed threshold because of the inequality constraints. An SOC formulation is proposed in [34], and we will summarize that in next section. When the threshold ε is chosen to make the problem feasible, this modified MVDR can converge to the optimal solution and the output power is minimized under this threshold. However, an unsuitable sidelobe threshold can make the problem infeasible.

3.3.4 Optimum Threshold for PT-DQC

In order to overcome the uncertainty of feasibility, we propose a new approach to search for the optimal threshold. In this approach the objective function in the MVDR method is reformulated by introducing a new weighted “penalty function”, which is the threshold for the multiple quadratic constraints outside the mainlobe. The principle is to search for the solution that optimally and automatically trades off among the interference null’s depth, the mainlobe width and the sidelobe level. The corresponding form of the optimum threshold discrete quadratic constrained optimization method (OT-DQC) is

$$\begin{aligned} \min_{\mathbf{w}, \varepsilon} \quad & \mathbf{w}^H \mathbf{R} \mathbf{w} + \alpha^2 \varepsilon^2 \quad s.t. \quad \mathbf{w}^H \mathbf{a}_s = f \\ & \left| \mathbf{w}^H \mathbf{a}(\theta_j) \right|^2 \leq \varepsilon^2 \quad \text{for } j = 1, 2, \dots, J \end{aligned} \quad (3.16)$$

where α^2 is the parameter indicating the degree of importance of the sidelobe control. We can adjust the weight in certain range, but no matter which one we choose the optimization problem is feasible. Note that the parameter ε is not a preset threshold as in Eq. (3.15), but is an optimization variable. Again there is still a question of finding an efficient optimization algorithm to solve Eq. (3.16).

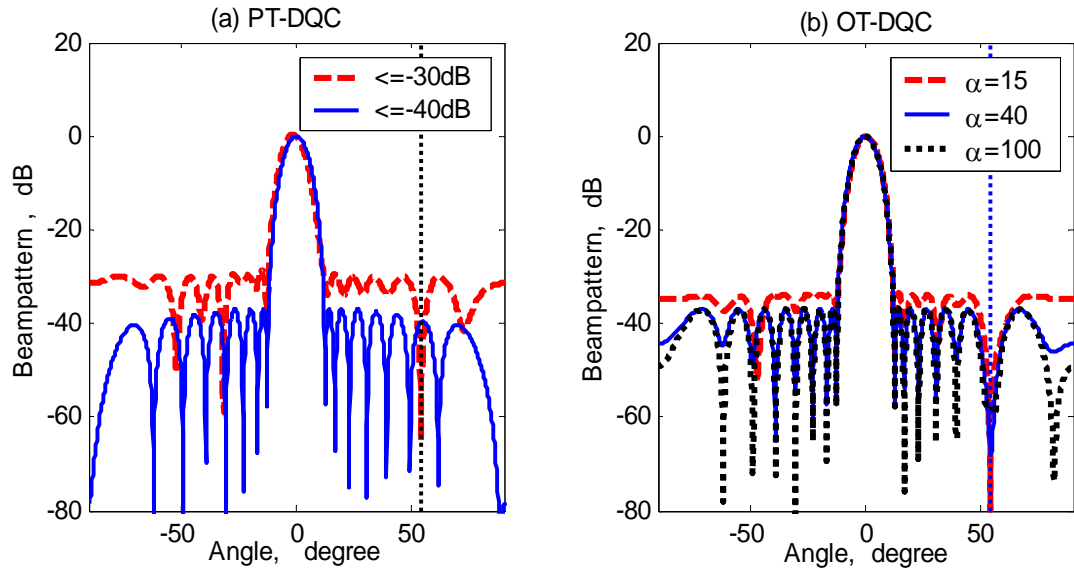


Figure 3-3 (a) Beam patterns of PT-DQC for sidelobes less than -30 dB and -40 dB; (b) Beam patterns of OT-DQC for α equal to 15, 40 and 100

Examples of sidelobe control from PT-DQC and OT-DQC are shown in Figure 3-3. Again the desired signal is at 0° and the interferer is at 54° . From Figure 3-3 (a) it is obvious that when the hard threshold is chosen too small (corresponding to -40 dB), the PT-DQC fails to work since a peak instead of a null appears at 54° . In Figure 3-3 (b) we demonstrate the effect of weight factor α in OT-DQC. Three different values are tried, and all resulting beam patterns and SINRs indicate that OT-DQC is insensitive to α when its value is above 10.

3.4 SOC and Unification of Sidelobe Control Methods

The SOC [37] is a constrained optimization problem that minimizes a linear cost function over the intersection of an affine set and the direct product of second-order cones, which can be formulated as:

$$\min_{\mathbf{x}} \mathbf{c}_0^T \mathbf{x} \quad s.t. \quad \|\mathbf{A}_i \mathbf{x} + \mathbf{b}_i\|_2 \leq \mathbf{c}_i^T \mathbf{x} + d_i, \quad i = 1, 2, \dots, q \quad (3.17)$$

where $\mathbf{x} \in \mathbb{R}^n$, $\mathbf{A}_i \in \mathbb{R}^{(k_i-1) \times n}$, $\mathbf{b}_i \in \mathbb{R}^{(k_i-1)}$, $\mathbf{c}_i \in \mathbb{R}^n$ and $d_i \in \mathbb{R}$. The symbol $\|\cdot\|_2$ represents the Euclidean norm (2-norm). The i^{th} constraint is the k_i -dimensional second-order cone defined by

$$soc^{k_i} = \begin{cases} \{(z_1, \mathbf{z}_2) \mid z_1 \geq \|\mathbf{z}_2\|_2\} & \text{for } k_i > 1 \\ \{(z_1) \mid z_1 \geq 0\} & \text{for } k_i = 1 \end{cases} \quad (3.18)$$

where variables $z_1 = \mathbf{c}_i^T \mathbf{x} + d_i \in \mathbb{R}$, $\mathbf{z}_2 = \mathbf{A}_i \mathbf{x} + \mathbf{b}_i \in \mathbb{R}^{k_i-1}$.

The SOC can be solved efficiently via primal-dual interior point methods [36] and several Matlab toolboxes have been developed such as Lobo, Vandenberghe, Boyd's SOC package, and Sturm's SeDuMi [35]. SeDuMi using a self-dual interior-point method is adopted in this chapter. It is possible to formulate our SOC models in primal or dual form treated the same way as in SeDuMi. The dual problem yields the tight lower bound if the primal problem is feasible and the solution is on the boundary. The standard forms of the primal problem (3.19) and dual problem (3.20) are

$$\min_{\mathbf{x}} \mathbf{c}^H \mathbf{x} \quad s.t. \quad \mathbf{A} \mathbf{x} = \mathbf{b}; \mathbf{x} \in K \quad (3.19)$$

$$\min_{\mathbf{y}} \mathbf{b}^H \mathbf{y} \quad s.t. \quad \mathbf{c} - \mathbf{A}^H \mathbf{y} \in K \quad (3.20)$$

where \mathbf{x} and \mathbf{y} denote the vectors containing the designed variables, and equation $\mathbf{c}^H \bar{\mathbf{x}} = \mathbf{b}^H \bar{\mathbf{y}}$ holds when $\bar{\mathbf{x}}$ and $\bar{\mathbf{y}}$ are the optimal solutions for problems (3.19) and (3.20),

respectively. The symmetric cone K is a Cartesian product of elementary cones which are defined in (3.18).

3.4.1 SOC Formulation of PT-DQC

PT-DQC is formulated as SOC programming in [34]. The output power in the problem can be rewritten as

$$\mathbf{w}^H \mathbf{R} \mathbf{w} = \mathbf{w}^H \mathbf{R}^{\frac{1}{2}} \mathbf{R}^{\frac{1}{2}} \mathbf{w} = \left\| \mathbf{R}^{\frac{1}{2}} \mathbf{w} \right\|_2^2 \quad (3.21)$$

Therefore the problem (3.15) can be reformulated into

$$\begin{aligned} \min \tau \quad & \text{s.t. } \mathbf{w}^H \mathbf{a}_s = f; \\ & \left\| \mathbf{R}^{\frac{1}{2}} \mathbf{w} \right\|_2 \leq \tau; \left\| \mathbf{w}^H \mathbf{a}(\theta_j) \right\|_2 \leq \varepsilon; \text{ for } j = 1, 2, \dots, J \end{aligned}$$

which is an SOC problem.

3.4.2 SOC Formulation of OT-DQC

The corresponding SOC form of the OT-DQC is as follows:

$$\min_{\mathbf{w}, \varepsilon} \left\| \begin{bmatrix} \mathbf{R}^{\frac{1}{2}} \mathbf{w} \\ \alpha \varepsilon \end{bmatrix} \right\|_2 \quad \text{s.t. } \mathbf{w}^H \mathbf{a}_s = f; \left\| \mathbf{w}^H \mathbf{a}(\theta_j) \right\|_2 \leq \varepsilon; \text{ for } j = 1, 2, \dots, J.$$

Then our approach can be solved by the SeDuMi toolbox as a standard dual problem, where the form is

$$\begin{aligned}
& \min_{\mathbf{y}} \mathbf{b}^H \mathbf{y} \\
& s.t. \quad \mathbf{a}_s^H \mathbf{w} - f = -f - \begin{bmatrix} 0 & 0 & -\mathbf{a}_s^H \end{bmatrix} \mathbf{y} \triangleq \mathbf{c}_1 - \mathbf{A}_1^H \mathbf{y} \in soc^1 \\
& \quad \begin{bmatrix} \tau \\ \frac{1}{\mathbf{R}^2} \mathbf{w} \\ \alpha \varepsilon \end{bmatrix} = \begin{bmatrix} 0 \\ \mathbf{0} \\ 0 \end{bmatrix} - \begin{bmatrix} -1 & 0 & \mathbf{0}^T \\ 0 & 0 & -\mathbf{R}^2 \\ 0 & -\alpha & \mathbf{0}^T \end{bmatrix} \mathbf{y} \triangleq \mathbf{c}_2 - \mathbf{A}_2^H \mathbf{y} \in soc^{m+2} \\
& \quad \begin{bmatrix} \varepsilon \\ \mathbf{a}^H(\theta_j) \mathbf{w} \end{bmatrix} = \begin{bmatrix} 0 \\ \mathbf{0} \end{bmatrix} - \begin{bmatrix} 0 & -1 & \mathbf{0}^T \\ 0 & 0 & -\mathbf{a}^H(\theta_j) \end{bmatrix} \mathbf{y} \triangleq \mathbf{c}_{2+j} - \mathbf{A}_{2+j}^H \mathbf{y} \in soc^2 \\
& \quad \text{for } j=1, 2, \dots, J
\end{aligned}$$

and where the variable vectors \mathbf{y} and \mathbf{b} are defined as $\mathbf{y} = [\tau \ \varepsilon \ \mathbf{w}^H]^H$,

$\mathbf{b} = [1 \ \mathbf{0}_{(m+1) \times 1}^T]^T$ respectively. Compared with the dual problem (3.20), the standard

parameters are defined as $\mathbf{c} = [\mathbf{c}_1^T \ \mathbf{c}_2^T \ \dots \ \mathbf{c}_{J+2}^T]^T$; $\mathbf{A} = [\mathbf{A}_1^H \ \mathbf{A}_2^H \ \dots \ \mathbf{A}_{J+2}^H]^H$;

$$K = soc^1 \times soc^{m+2} \times (soc^2)^J.$$

3.4.3 SOC Formulation of Diagonal Loading

The MVDR with diagonal loading in Eq. (3.10) can be recast into the SOC formulation:

$$\min_{\mathbf{w}} \left\| \mathbf{R}^{\frac{1}{2}} \mathbf{w} \right\|_2 \quad s.t. \quad \mathbf{w}^H \mathbf{a}_s = f; \|\mathbf{w}\|_2 \leq \sqrt{T_0}$$

3.4.4 SOC Formulation of PF Methods

The original PF can also be formulated into the SOC structure as

$$\min_{\mathbf{w}, \varepsilon} \left\| \begin{bmatrix} \frac{1}{\mathbf{R}^2} \mathbf{w} \\ \mu \varepsilon \end{bmatrix} \right\|_2 \quad s.t. \quad \mathbf{w}^H \mathbf{a}_s = f; \left\| \mathbf{Z}^{\frac{1}{2}} (\mathbf{w} - \mathbf{w}_q) \right\|_2 \leq \varepsilon$$

3.5 Simulations and Experiments

In this section we compare the performances of those sidelobe control methods discussed through the numerical simulations. Because all approaches can be formulated as SOC, the SeDuMi is a friendly tool to work with. We adopt a uniform linear array with 16 sensors spaced at half-wavelength. The desired signal is at 0° and the corresponding SNR is 0 dB. A jamming interference at 54° is injected with a power of 45 dB relative to the sensor signal. The space and time domain sensor noises are modeled as white Gaussian noise.

In the first example we present the effect of the weight factor α in OT-DQC through the Monte Carlo simulation (100 trials). Two parameters of interest, the output average SINR and the optimal threshold obtained from the SOC, are considered to measure the sensitivity of the weight α in OT-DQC, as shown in Figure 3-4. The covariance matrix is calculated from 32 snapshots. It is obvious that SINR and the threshold converge to the stable values when the weight factors are 10 and 20 respectively. The converged value of SINR is 9.75dB and that of the threshold is $10\log_{10}(\varepsilon^2) = -37.2dB$. So the solution from OT-DQC is not sensitive to the weight factor α when it is within a widely selectable region.

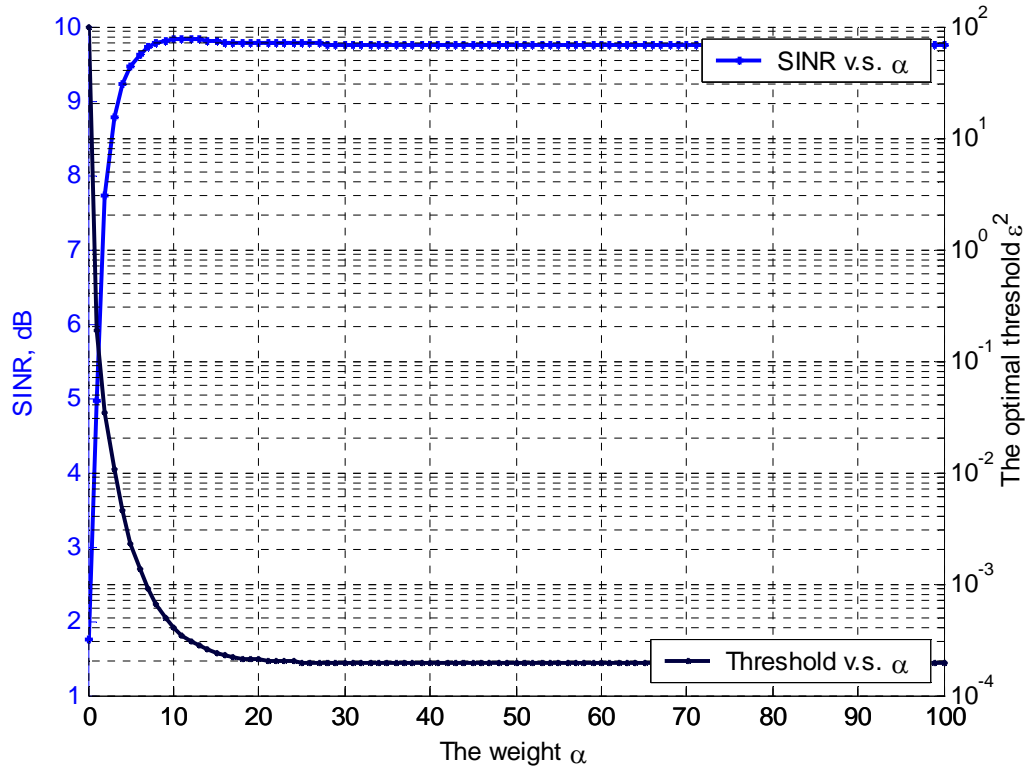


Figure 3-4 SINR and the optimal threshold ε^2 variation versus the weight α

Next we compare the performances of the different sidelobe control methods through numerical simulation. The loading factor in the diagonal loading method is estimated as the standard deviation of the diagonal elements of the estimated covariance matrix [30]. For the PF method the symmetric Dolph-Tchebychev quiescent beampattern is chosen with -30 dB sidelobe level and the weighting function is defined as

$$h(\theta) = \begin{cases} 0 & \text{if } |\theta| \leq \theta_0 \\ \cos \theta & \text{if } |\theta| > \theta_0 \end{cases} \quad (3.22)$$

where $\theta_0 = 12^\circ$. Moreover, the weighting factor u^2 is chosen to be 225 for the PF method. We choose 40 symmetric uniformed inequality constraints in the sidelobe region for the PT-DQC and OT-DQC. The hard threshold for the PT-DQC is chosen to be $\varepsilon^2 = 0.001$

which corresponds to sidelobe level -30 dB. The weighting factor for the OT-DQC is chosen to be $\alpha = 15$ in order to be the same as the weight in the PF method.

In Figure 3-5 we have taken 32 snapshots of the received data to compute the sample covariance matrix. In Figure 3-6 the number of snapshots is varied, and the average output SINRs vs. snapshot number are displayed for the different methods. The optimum SINR is 12 dB. The diagonal loading method in Figure 3-6 has the highest average SINR, which is about 11.7 dB in the steady state, however the resulting highest sidelobe is -13.3 dB (Figure 3-5 (a)), which is also the highest among all the methods. The PF method has steady state SINR output = 11.2 dB, and its highest sidelobe is -29 dB (Figure 3-5 (b)). The PT-DQC and OT-DQC have almost the same SINR output curves as shown in Figure 3.6. The highest sidelobe for PT-DQC and OT-DQC are respectively -30dB (Figure 3-5 (c)), and -36.5 dB (Figure 3-5 (d)). Overall, OT-DQC has the best sidelobe control performance with little SINR sacrificed. Lower sidelobes may be achieved by the PT-DQC or PF method by setting a lower threshold or quiescent beampattern with a lower sidelobe level, respectively. However a more aggressive choice may result in an infeasible and non-meaningful solution as shown in Figure 3-3 (a).

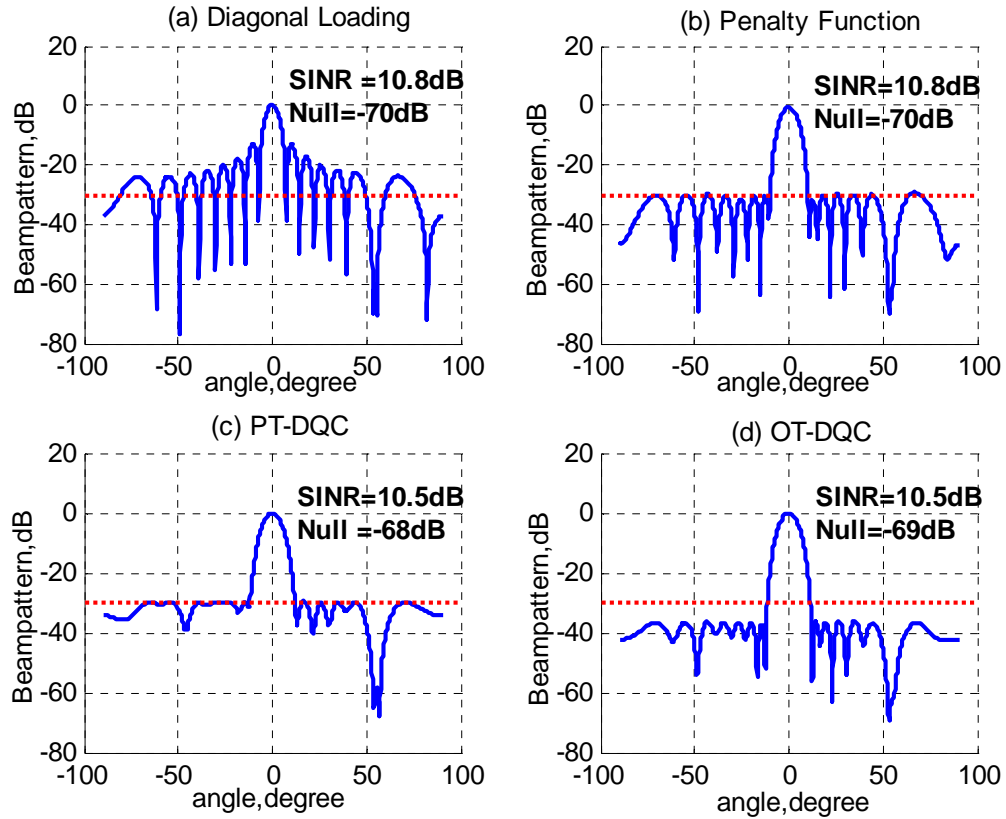


Figure 3-5 The beam pattern of the sidelobe control algorithms, 32 snapshots; (a) Diagonal loading ; (b) PF with weighting factor $\mu = 15$; (c) PT-DQC with $\varepsilon^2 = 0.001$, (d) OT-DQC with weighting factor $\alpha = 15$.

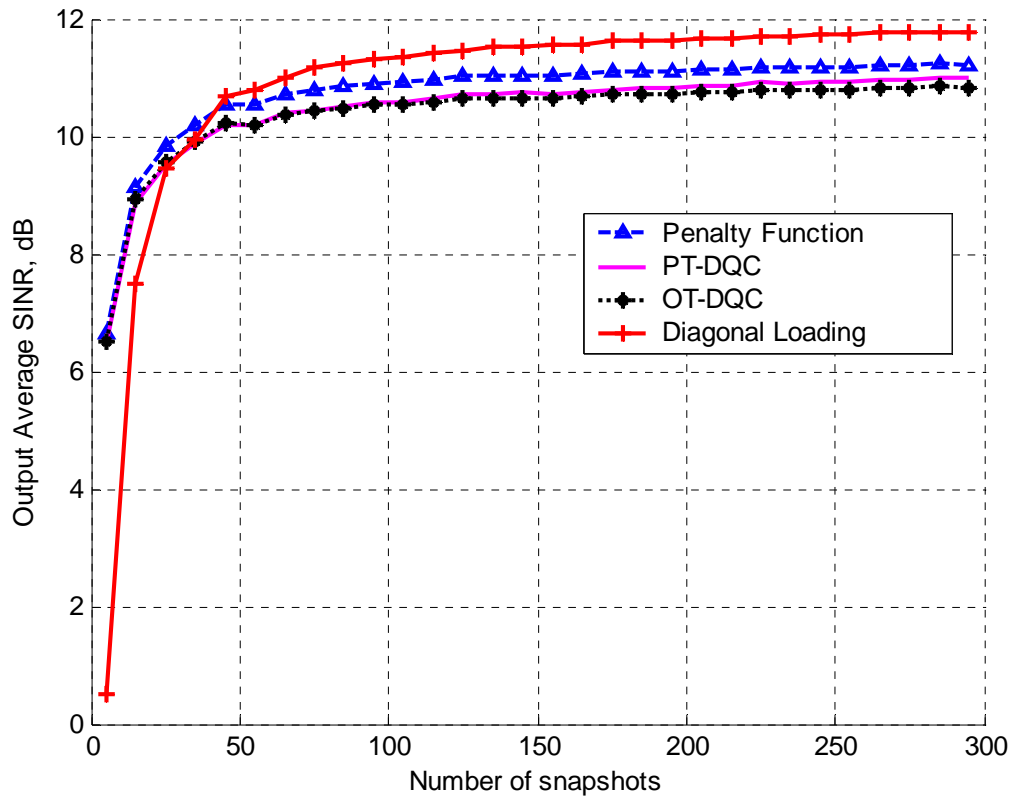


Figure 3-6 The output average SINR (300 trials) vs. number of snapshots.

Real sea clutter background data has been provided by Raytheon Canada Ltd. The radar utilizes a floodlight transmitting antenna and omnidirectional phased array with 16 sensors as receiver. The data set is collected using a 3.2MHz carrier frequency and the dwell time is about 164s. The surveillance range is 51.5 km ~300 km with azimuth of 120 degrees. We simulate a target at range 180 km, DOA 30 degrees, and Doppler frequency 0.1028 Hz. Here we utilize a large number of snapshots to estimate the covariance matrix, so the high sidelobes in the beampattern after adaptive beamforming is not produced from the small sample size but from the complicated sea conditions. The sidelobe control algorithms are applied to show the different threshold level, mainbeam width and nulling depth in Figure 3-7. The symmetric Dolph-Tchebychev quiescent beampattern is chosen

with -20 dB sidelobe and the threshold in PT-DQC is set as $\varepsilon^2 = 0.01$ (-20 dB sidelobe threshold).

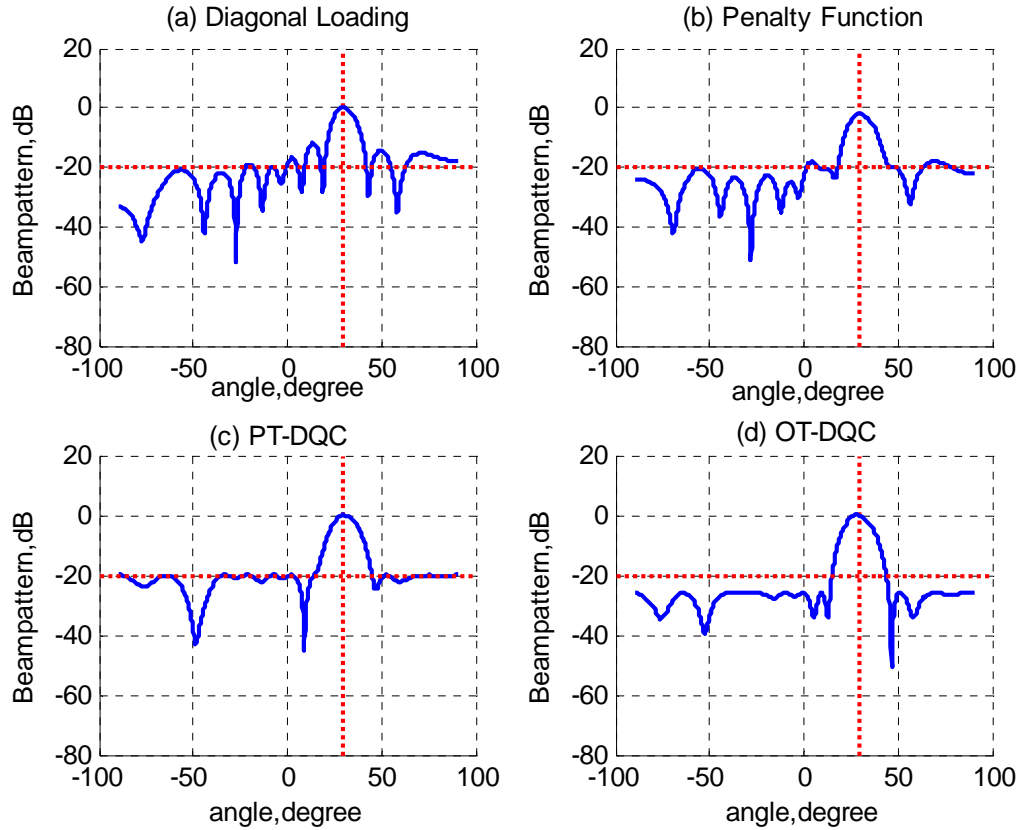


Figure 3-7 The beampattern of the sidelobe control algorithms.

3.6 Summary

We have discussed three categories of sidelobe control techniques for MVDR; these are diagonal loading methods, PF methods and quadratic inequality constraints. All these methods satisfy the SINR slightly different, while gaining greatly enhanced suppression over the sidelobe levels.

Diagonal loading minimizes the whole beampattern level (both sidelobe and mainbeam) except in the look direction, which makes the output SINR from diagonal

loading higher than the other algorithms. Although the diagonal loading algorithm is fast and simple, the sidelobe control performance is not satisfactory due to two obvious reasons: 1) there is no optimum expression for the loading value, and 2) there is no direct relationship between the loading value and sidelobe levels.

The original PF methods have moderate SINR, but they have no precise control over the sidelobes. They also have the inherent disadvantage (as discussed in section 3.2) that they tend to minimize the difference in levels of the interference null and quiescence peak.

The PT-DQC method solves the problem for strict control over the sidelobe beam pattern with a reasonable SINR, however there is still a feasibility problem. By changing the preset hard threshold into one optimization parameter, the OT-DQC overcomes the feasibility problem. The idea is to search for the optimal solution that trades off the interference null's depth, the mainlobe width and the sidelobe level automatically. The simulation results validate the improved performance and feasibility.

Chapter 4 - Constant False Alarm Rate Detectors

4.1 Introduction

Constant False Alarm Rate is a general approach to detect targets beyond fixed thresholds in radar and sonar systems. In HF radar, target echoes are usually buried in all kinds of noises and clutters. The clutter-plus-noise power is usually unknown and a fixed threshold scheme for target detection will result in a high false alarm rate.

There are three main classes of CFAR algorithms discussed in the open literature: *non-parametric detector*, *adaptive threshold* and *clutter map*. Both non-parametric detectors and adaptive threshold methods are based on the assumption that at least homogeneity exists in a small region around the target cell being tested. Non-parametric detectors, also known as Distribution Free detectors, require no knowledge of the background statistics and obtain a constant false alarm rate by ranking the test samples, usually against the reference cells. Under the hypothesis that all the samples (test and reference) are independent samples from an unknown Probability Density Function

(PDF), the test samples all have a uniform density function and consequently, a threshold, which yields a CFAR, can be set. The adaptive threshold methods assume that the noise distribution is known but with unknown parameters. The surrounding reference cells are then used to estimate the unknown parameters and a threshold based on the estimated distribution is obtained. Clutter map CFAR stores an average background level for each range-azimuth cell. A target is then declared in a range-azimuth cell if the new value exceeds the average background level by a specified constant [38].

Among adaptive threshold methods, the Cell Averaging (CA) CFAR processor is optimal (maximizing detection probability) in a homogeneous background when the reference cells contain Independent and Identically Distributed (IID) observations. However the CA-CFAR degrades dramatically when applied to non-homogeneous background such as clutter edge or multiple targets scenarios. A number of modifications and novel schemes based on CA-CFAR have been developed to improve the performance in non-homogeneous situation with different degrees of CFAR loss. The detailed methods will be reviewed in the next section. These methods are firstly investigated and analyzed based on targets detection in Rayleigh noise and then extended to other distributions including both Weibull and K distributions. It is well known that if the complex data is Gaussian, its envelope is Rayleigh-distributed and its power is exponentially distributed. The CFAR process may have a linear (based on Rayleigh distribution) or square-law (based on exponential distribution) detector; however there is little difference between these two methods in practical application. Although the reference window is in general set along the range cells in CFAR processing, recent research has extended the methods

into both 2-dimensional (range-Doppler) CFAR and 3-dimensional (range-Doppler-time) CFAR as well [51].

In section 4.2, we present a literature survey of current CFAR schemes. In section 4.3 we present a novel hybrid CFAR method with an adaptive footprint, which improves the target detection performance for the complex clutter and noise situation of HF radar. The theoretical performance analyses are studied in section 4.4 for both homogeneous and non-homogeneous backgrounds. The CFAR results from real data are presented in section 4.5, where the final tracker output results are also shown to demonstrate the advantage of novel CFAR detector.

4.2 State of the Art

Radar detection is a binary hypothesis-testing problem. Although there are several criteria available to solve this problem, the most appropriate one is the Neyman-Pearson in that it requires no prior probability information. This criterion maximizes the probability of detection for a given probability of false alarm by comparing the likelihood ratio to a scalar value. The threshold is determined by the probability of false alarm P_{fa} . Assuming the PDF in the null hypothesis (H_0) is $f_0(x)$ and the PDF in the alternative hypothesis (H_1) is $f_1(x)$. The null hypothesis means that the received signal contains noise and clutter only while the alternative hypothesis means that the received signal consists of a target return. The probability of detection P_d is

$$P_d = P[x > x_0 | H_1] = \int_{x_0}^{\infty} f_1(x) dx \quad (4.1)$$

And the probability of false alarm P_{fa} , which is to declare H_1 while H_0 is actually in effect, can be expressed as

$$P_{fa} = P[x > x_0 | H_0] = \int_{x_0}^{\infty} f_0(x) dx \quad (4.2)$$

where x_0 is the fixed threshold under the assumption that the total power is known. The probabilities P_d and P_{fa} decrease simultaneously when x_0 increases.

In the CFAR detector the tested cell is declared as a target or not based on the comparison with the product of T and Z (TZ is the estimation of x_0).

$$\begin{aligned} x > TZ & \text{ target detected} \\ x \leq TZ & \text{ no target} \end{aligned}$$

The random variable Z is related to the local estimate of the noise power within the finite reference window. The constant scale factor T is selected to obtain a given false alarm probability, as illustrated in Figure 4-1. The estimation variance results in inherent loss of detection probability in CFAR process compared with the optimal detector.

If it is assumed that the square-law detector is adopted, the output of each range cell is exponentially distributed:

$$f(x) = \frac{1}{2\lambda_1} \exp\left(-\frac{x}{2\lambda_1}\right) \quad (4.3)$$

where

$$\lambda_1 = \begin{cases} \mu & \text{under } H_0 \\ \mu(1+S) & \text{under } H_1 \end{cases}.$$

Under the null hypothesis H_0 of there being no target in a range cell and a homogeneous background, λ_1 is equal to the background noise power μ . Under the alternative hypothesis H_1 indicating the presence of a target, λ_1 is $\mu(1+S)$ with S be the signal-to-noise ratio of the target.

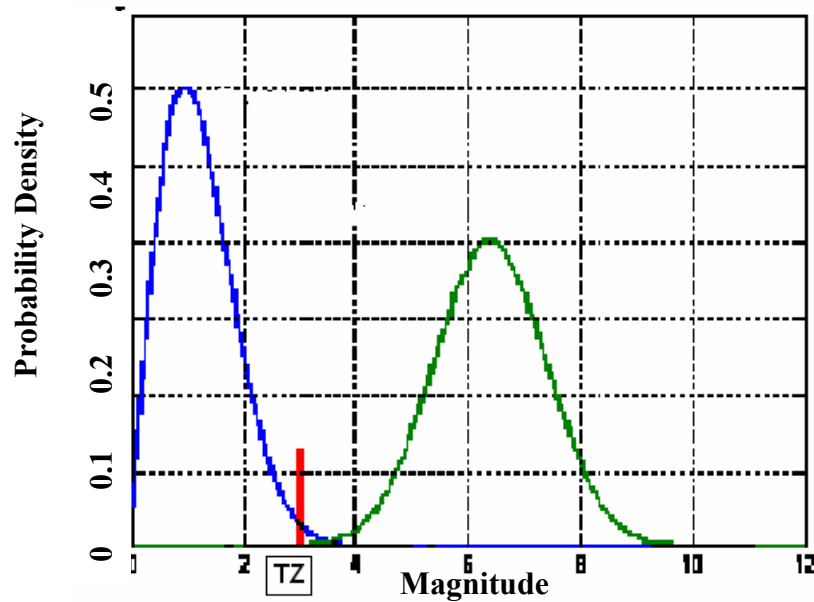


Figure 4-1 Illustration of the Neyman-Pearson rule. Blue trace (PDF of noise only); green trace (PDF of target + noise); red line (threshold).

4.2.1 CA-CFAR and Its Variants

CA-CFAR sets the threshold adaptively by estimating the mean level in a reference window around the test cell. It is a consistent, unbiased and minimum-variance estimator, whose performance converges to the optimum Neyman-Pearson detector for a homogeneous background when the reference window tends to infinity.

The performance of CA-CFAR is significantly degraded when the assumption of a homogeneous environment does not hold. Recent research has mainly focused on the clutter transition region and multiple targets situation in the reference window. When

there is a clutter edge in the reference window, the increased background noise power degrades the detector performance (either excessive false alarm or target masking). When there are two or more close-spaced targets, the noise power estimate is biased by the interfering signal resulting in an unnecessarily high threshold and the weak targets may not be detected. Modifications of the CA-CFAR schemes have been proposed to overcome these problems with somewhat performance loss under the homogenous situation.

The reference window can be split into leading and lagging parts symmetrically around the cell under test. Hansen [39] has proposed the Greatest Of (GO) CFAR to regulate false alarm rate especially in the region of clutter transition; in his procedure the noise power is estimated by the larger sum in the leading and lagging windows. The Censored Greater Of (CGO) CFAR attempts to improve the GO-CFAR performance when an arbitrary number of interfering targets are present in the leading and lagging reference cells. The CGO-CFAR discards several of the largest samples on each side window from further analyses. However, it has been shown that the performance is improved only if the number of targets is less than the censored number [40]. An Adaptive GO-CFAR proposed in [41] adopts the approach of [42] to accept or reject the reference samples.

Trunk [43] proposes a CFAR processing scheme in order to prevent the suppression of closely spaced targets; the Smallest Of (SO) the sums in the leading and lagging windows is used to estimate the noise power. However this processor only works well if the interfering targets are located in either the leading or lagging windows and not both.

Furthermore the SO-CFAR processor fails to maintain a constant false alarm rate at clutter edges.

An excision CFAR detector, proposed and analyzed in [44] and illustrated in Figure 4-2, alleviates the interference presence by excising strong signals before the cell-averaging operation. The samples pass through an excisor, which nulls any sample that exceeds a predetermined threshold. The set of surviving samples at the excisor's output is averaged with only the nonzero samples. The average value of the samples is multiplied by another predetermined detection coefficient and the product is used as the detection threshold. A sample cell that exceeds the detection threshold is declared to be a local detection. To improve the overall performance, the Excision CFAR detector can be augmented with a post-detection integrator which performs global detection. An analysis of the excision CFAR detector in the presence of fluctuating targets has been undertaken in [45] where it is shown to be only applicable when the interference power level is higher than the target signal.

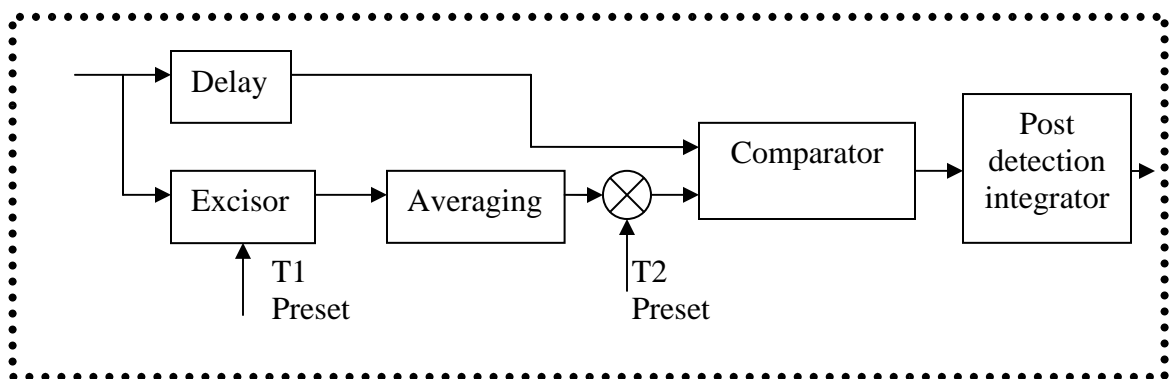


Figure 4-2 The Block Diagram of Excision CFAR detector

4.2.2 Ordered Statistics CFAR

A different processor, known as the Ordered Statistics CFAR (OS-CFAR) scheme, has been introduced to deal with both multi-targets and clutter edge environments [46] [47]. The idea is borrowed from image processing where OS schemes, especially median filtering, are effective in rejecting impulsive noise and preserving edges in image restoration. The OS-CFAR estimates the noise power by selecting the k^{th} largest cell in the reference window. This processor suffers only minor degradation in the probability of detection, and can resolve closely spaced targets effectively (maximum k different target without range spread). However the OS-CFAR processor is unable to prevent excessive false alarm rate at the clutter edges without sacrificing great loss of detection performance. A performance comparison of OS-CFAR with CA-CFAR and Censored CA-CFAR is presented in [48].

The Moving Order Statistics (MOS) CFAR [49] is a two-layer OS-CFAR where the selected samples in the first layer are obtained from a moving sub-window in the reference cells. These samples are then ranked again in the second layer to obtain the final noise power estimation as shown in Figure 4-3. It has been shown that the performance of MOS-CFAR in non-homogeneous situation is superior to that of OS-CFAR. However the rank parameter in each layer must be carefully selected in order to maintain a robust result.

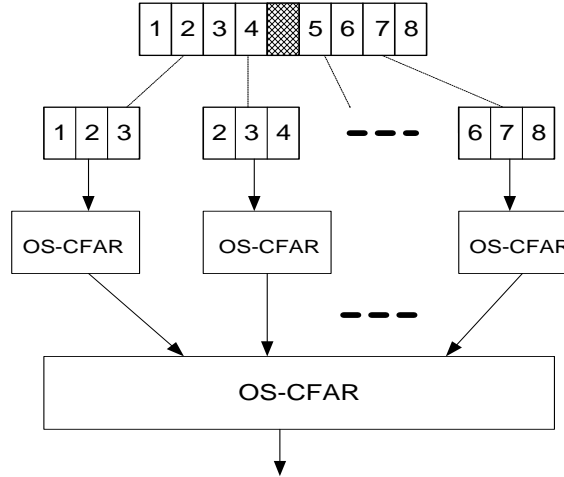


Figure 4-3 Block diagram for MOS-CFAR detector

A hybrid CFAR processor, its block diagram shown in Figure 4-4, has been implemented in [50]; it is named as the Censored Mean-Level (CML) CFAR. The samples in the reference window of size N are symmetrically split into leading and lagging parts. Within each part the range cells are ranked according to their amplitude level and the largest $\frac{N}{2} - k_{1,2}$ samples are removed and the sub-sum of each part is the combination of the CA- and OS-CFAR processors

$$Z_{[1,2]} = \sum_{i=1}^{k_{[1,2]}} x_{i[1,2]} + \left(\frac{N}{2} - k_{[1,2]} \right) x_{k_{[1,2]}} \quad (4.4)$$

where $(.)_{[1,2]}$ refers to lagging and leading parts respectively.

The CML-CFAR is more robust in the multi-target environment than CA- and OS-CFAR when the number of extra targets is known *a priori*.

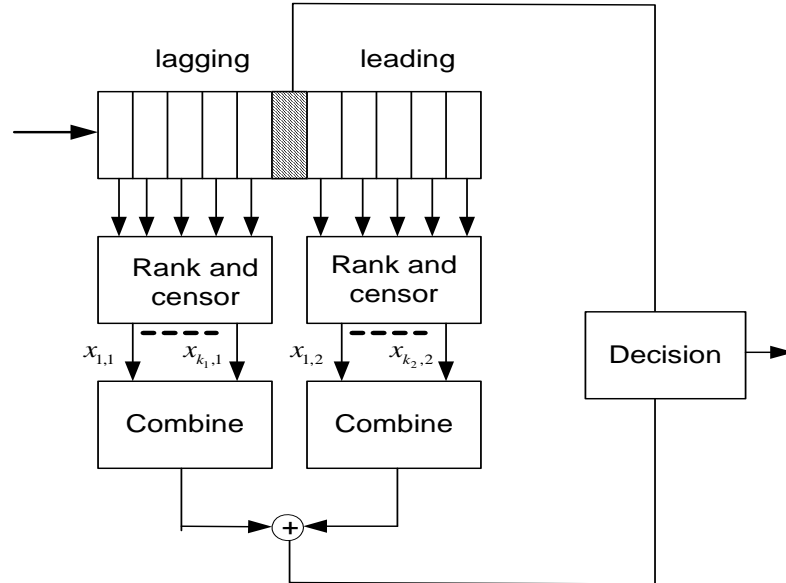


Figure 4-4 Block diagram of the CML-CFAR detector

The OS-CFAR method and its modifications sacrifice detection performance in homogenous background to provide better performance in a non-homogeneous environment. Moreover the CFAR loss will become unacceptable in the case of small reference window. The weighted window (step window and trapezium window) CFAR [54] is proposed to overcome this problem and can be viewed as a compromise between CA- and Trimmed Mean CFAR [42]. This approach is of practical interest in the special cases of the low SNR and small size reference window.

4.2.3 Clutter Map CFAR

In the homogeneous environment, clutter maps store an average background level for each range-azimuth cell. This average power level is updated every scan. A target is then declared in the tested cell if its value exceeds the average background level by a specified amount [55].

Lops and Orsini propose a novel scan-by-scan averaging CFAR [56], which uses an envelope detector instead of the square-law detector in the original Clutter Map (CM) CFAR. A small map window is chosen and the maximum cell value in this map is selected to update the background power in this map, thus provide certain level of protection against the local non-homogeneous clutter. A block diagram for this CFAR is shown in Figure 4-5. The current return is compared with the power level stored in last scan as

$$\begin{cases} x_n(i) > TZ_{n-1} & \text{target in } i^{\text{th}} \text{ cell} \\ x_n(i) < TZ_{n-1} & \text{no target in } i^{\text{th}} \text{ cell} \end{cases}$$

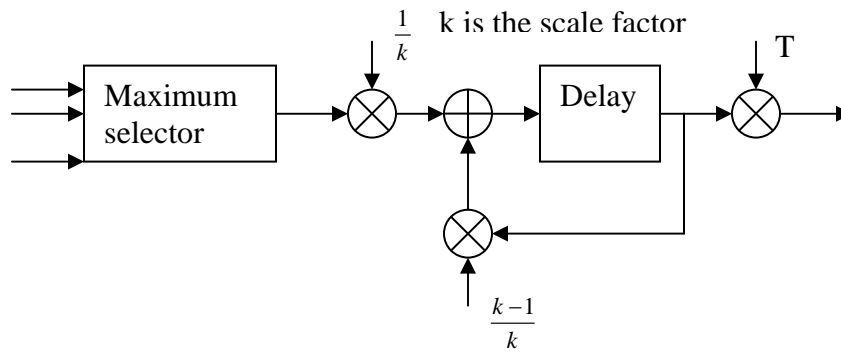


Figure 4-5 Block diagram of scan by scan averaging CFAR

When the clutter comes from ocean or land, the more common clutter PDF is multi-parametric PDF with scale and shape parameters. Conte and Lops [57] extend the clutter-map CFAR to lognormal and Weibull distributed clutter, whose cumulative distributed functions (CDF) are

$$P(x | H_0) = 1 - \exp\left[-\left(\frac{x}{\alpha}\right)^\beta\right] \quad (\text{weibull CDF})$$

$$P(x | H_0) = 1 - Q\left(\frac{\ln x - \alpha}{\beta}\right) \quad (\text{lognormal CDF})$$

where $Q(\bullet)$ is the area under the right tail of a standard Gaussian variable; α and β are scale and shape parameters, respectively. The value Z in the CFAR threshold is a function of the estimated parameters α and β from the map cells. The parameter estimation can be obtained through linear filters where the Weibull or log-normal PDF is converted into a location-scale distribution by a logarithmic transformation as shown in Figure 4-6. The performance of this CFAR is presented in [58].

The selection of the spatial filter will lead to different algorithms. The combined CA-CM CFAR or OS-CM CFAR performance can be obtained by respectively averaging the map cells or picking the k^{th} largest value. The threshold is then updated using the information from both the neighboring cells and former scans [59]. Another way to use a filter with unbiased parameters is to linearly combine the map cells as in [60]. In order to prune outliers, the map cells are ranked and the largest k_1 cells and the smallest k_2 cells are discarded before linear combination.

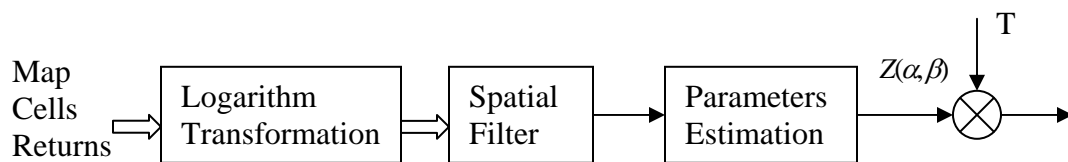


Figure 4-6 Block diagram for PDF transformed CM-CFAR

4.3 Hybrid CFAR Algorithm for HF Radar

High Frequency Surface Wave Radar is designed to detect and track maritime targets beyond the horizon. An OS-CFAR detector has been implemented to minimize false detections due to clutter for ship mode. A CA-CFAR has been applied for the air mode, where detection is generally against a homogeneous noise-like background. The OS-CFAR detector suffers moderate degradation in detection probability, but is effective in resolving closely spaced targets in non-uniform clutter. However the OS-CFAR detector does not provide optimal performance due to the highly dynamic and complex nature of the clutter. Further improvement can be achieved for ship detection. In the following sections, a new CFAR scheme is proposed and evaluated to show the potential for the improved ship detection.

4.3.1 Range-Doppler Map Analysis

In HFSWR the transmitter sends out omni-directional pulses which cover the surveillance area of interest. The back-scattered pulses are received by a linear array of sensors and are coherently integrated to extract the Doppler information. A longer coherent integration time is used to obtain higher Doppler resolution for discriminating slow moving marine targets from the generally more dominant ocean clutter. After the beamforming process, a 3-D range-Doppler-azimuth data set is formed. The CFAR detector searches for possible target hits in Range-Doppler (RD) map for a given angle of arrival. As can be observed in Figure 4-7, the ionospheric and sea clutters dominate some particular areas of the RD map. The statistics associated with these clutters vary from CIT to CIT. The ocean clutter is the result of radar returns from the ocean surface

and has a complex structure. It is dominated by two peaks called first-order Bragg lines that can mask the returns from targets at their corresponding Doppler region. Ionospheric clutter is defined as those radar echoes whose propagation paths involve ionospheric layers.

According to the central limit theorem, the test and reference cells have Gaussian distributions after the Fourier transform. Therefore it has been assumed that the noise background in the RD map has a Gaussian distribution with varying mean and variance. Conventional CFAR methods that seek the target in a homogeneous background fail to reach expected performance when applied in the non-stationary mixed environment.

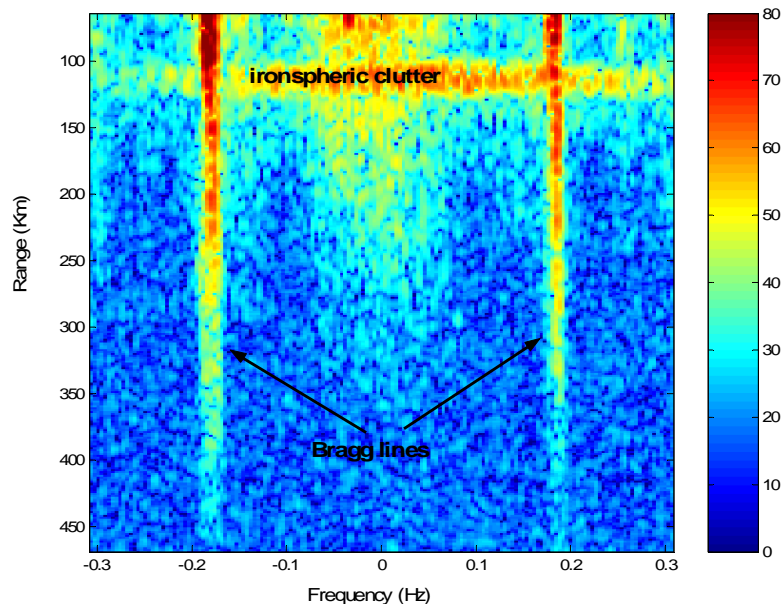


Figure 4-7 Sampled range-Doppler map from HF radar

In HFSWR the targets for CFAR detection spread in both range and Doppler dimensions. In order to improve the detection probability and decrease the straddling loss, over-sampling has been implemented in the pulse compression module. That is, there are

five samples in each range resolution cell. Moreover the weighted window in Doppler processing causes the target spreading in Doppler dimension. Generally speaking, the targets are considered to occupy 9 cells in the range dimension and 3 cells in the Doppler dimension.

4.3.2 Adaptive Switching CFAR

A variety of hybrid CFAR procedures have been proposed to improve the detection performance in the presence of mixed environments. For example a weighted CFAR technique [50] has been proposed, however this approach achieves neither the performance of CA-CFAR or OS-CFAR. In [52] a hybrid CFAR detector is introduced for HF radar, which is based on Greatest Of Order Statistic (GOOS) CFAR. In GOOS-CFAR the median values, along both range and Doppler cells' windows are compared, and the greatest is set as the threshold value Z

$$Z = \max(\text{rank}_{50\%}(\text{range window}), \text{rank}_{50\%}(\text{Doppler window})).$$

The median is chosen for its good edge detection property, and the Greatest-Of method is used to discriminate range and Doppler spread clutter. In this hybrid CFAR an extra local peak detection procedure is added in the GOOS to reduce the false alarm rate, which is claimed to be able to blank out part of the Bragg line effects. Qiang, et al. considers to separate detection for ship and aircraft in a range-Doppler map of the Over-the-Horizon Radar system [53]. For aircraft detection, preprocessing with a median filter is applied to suppress the slow-varying sea clutter and the final threshold is determined by OS-CFAR. In ship-mode, high-resolution processing (AR modeling) is applied in the pulse domain prior to CFAR detection in order to sharpen the Bragg lines, since the spectrum from the

AR filter has higher resolution than the conventional FFT. A composite CFAR technique proposed in [61] selects a CA-CFAR scheme in a homogeneous environment and switches to OS-CFAR in a non-homogeneous environment. However in this solution the switching threshold is based on only range information and is not appropriate when applied to the two-dimensional CFAR. In the following section we propose a hybrid CFAR technique based on a new switching criterion to obtain better target detection performance.

4.3.2.1 Switching Rule

The typical CA-CFAR adjusts the threshold adaptively from the estimated mean level of the reference window surrounding the test cell. Based on the range and Doppler spreading of point targets in HF radar, a guard window is adopted to exclude the spreading target information from noise power estimation. The decision, as to the presence of a target, is made based on the following criteria:

$$x(r,d) \underset{<}{\overset{\geq}{T}} \bullet \left[\frac{\sum_{i=-m}^m \sum_{j=-n}^n x(r+i,d+j) - \sum_{i=-m'}^{m'} \sum_{j=-n'}^{n'} x(r+i,d+j)}{(2m+1) \times (2n+1) - (2m'+1) \times (2n'+1)} \right] \quad (4.5)$$

where $(2m+1) \times (2n+1)$ is the size of reference window and $(2m'+1) \times (2n'+1)$ is the size of guard window. Target detection is claimed if the above greater sign is satisfied. The OS-CFAR processor estimates the noise power simply by selecting the k^{th} largest cell in the reference window. The same guard window is utilized in the reference window for proper estimation of the noise power.

To select different CFAR techniques for both non-homogeneous and homogenous environments a switching criterion is required. It has been shown that CFAR techniques based on linear, or amplitude detection and square-law, or power give similar results. For the square-law detector, each range-Doppler cell is assumed exponentially distributed with PDF the same as (4.3). The mean μ_x and variance σ_x^2 are computed directly from

$$\begin{aligned}\mu_x &= \int_0^{\infty} x \cdot f(x) dx = 2\lambda_1 \\ \sigma_x^2 &= \int_0^{\infty} x^2 \cdot f(x) dx - \mu_x^2 = (2\lambda_1)^2\end{aligned}\quad (4.6)$$

Based on the above equations the measured mean and variance are dependent on the only parameter in the exponential distribution. We can utilize either one to identify the type of background distribution.

The Kullback-Leibler (K-L) criterion [62], is an information measure that provides a directed distance of the dissimilarity between two statistical models. Through minimizing this K-L distance the best model is found to approximate the true data distribution in the candidate pool. Here the original cells in the RD map are Gaussian, so it can be assumed as the Gaussian Mixture Model [63]. The mixture number is one for the homogeneous background, while the mixture number is larger than one for the non-homogeneous background. The Bayesian Information Criterion (BIC) [64][65], a modified K-L distance for incomplete data analysis, has been utilized to estimate the optimal mixture number.

$$K = \arg \min(BIC(k)) = \arg \min \left\{ -2 \sum_{i=1}^N \log(g(x_i | \hat{\theta}(k))) + 2m_k \log(N) \right\}, \quad k = 1, 2, \dots, k_{\max} \quad (4.7)$$

where $g(x_i | \hat{\theta}(k))$ is the Gaussian mixture model of the samples x_i in the random sequence conditioned on the estimated vector $\hat{\theta}$ of cluster number k and $2m_k \log(N)$ is

the penalty to adjust for the bias in the first term. K-means [66] is adopted to cluster the data set based on the particular cluster number and to estimate the corresponding mean and variance for each cluster.

Standard deviation and information-based clustering have been used to discriminate the non-homogeneous region from the homogeneous region. Figure 4-8 shows the standard deviation map corresponding to the range-Doppler map of Figure 4-7. The larger the standard deviation within the reference window around the test cell, the more likely the reference window belongs to the clutter-dominated region. Figure 4-9 shows the division for the homogeneous and the non-homogeneous regions based on the BIC criterion. It is clear that two methods have similar results, except that there is small difference in certain ionosphere clutter region where it is set as the clutter-dominated region from the standard deviation method, but determined as one cluster from the BIC method. Overall the BIC method more accurately discriminates the clutter-dominated region from noise dominated region due to its minimum transition edge. However the standard deviation method is more computationally efficient, and the measured standard deviation σ_x is adopted to classify the noise-clutter background in the proposed adaptive switching CFAR algorithm without sacrificing too much performance.

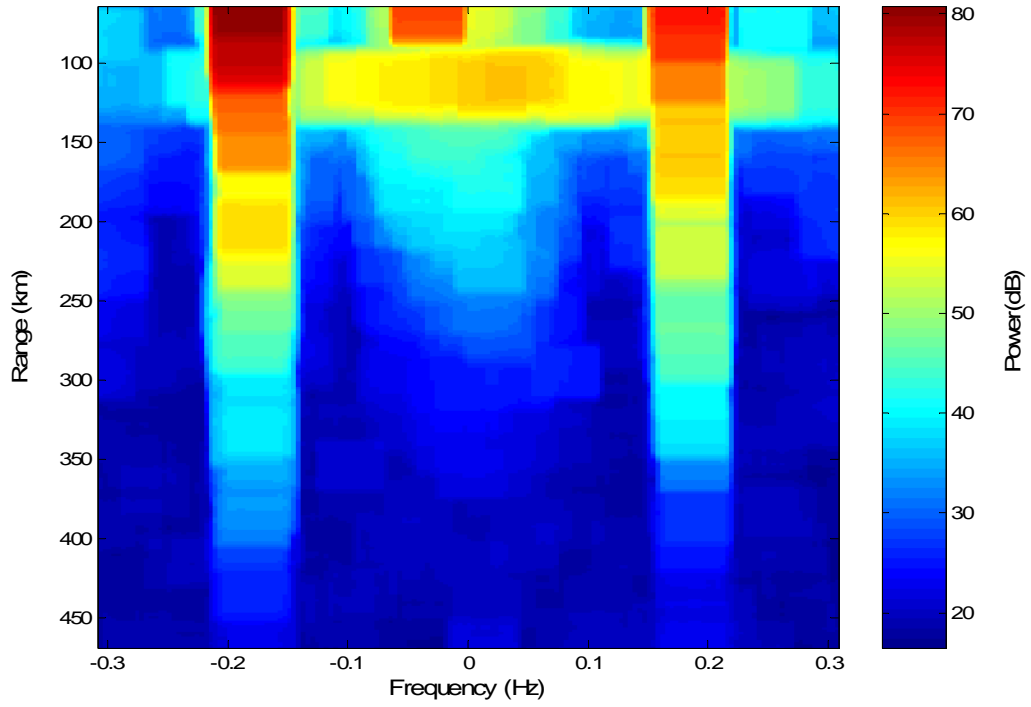


Figure 4-8 The standard deviation variation of range-Doppler map

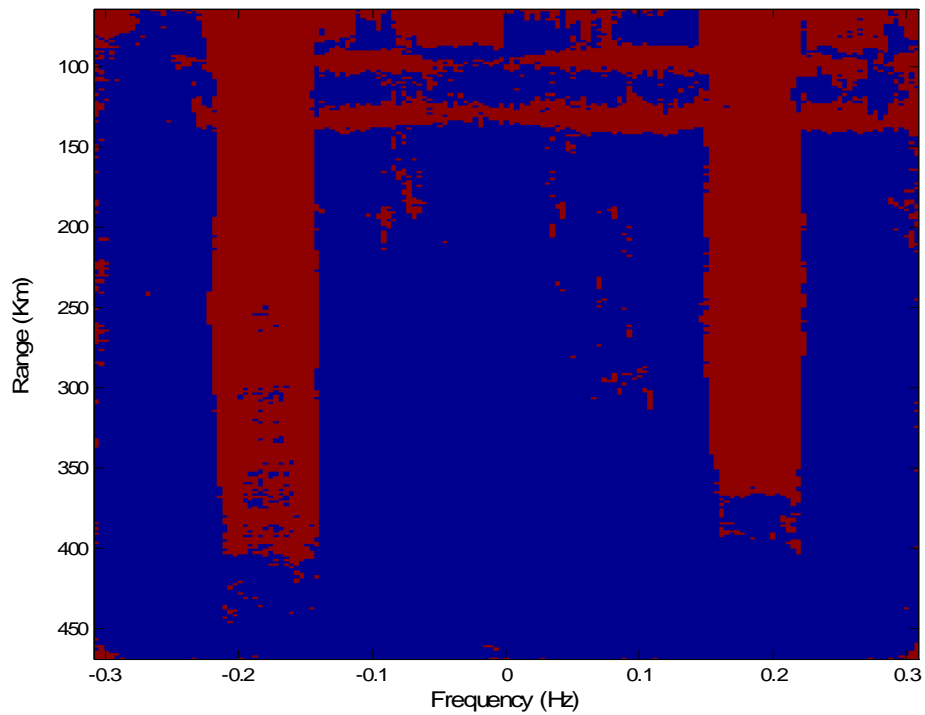


Figure 4-9 The division solution from BIC (blue means only one class and the red means more than one classes)

4.3.2.2 Adaptive Window Rule

In the above discussed CFAR detectors, the reference window for the non-homogeneous background is fixed in both size and shape, which does not properly represent the dynamic and complex RD map in HF radar. Sea clutter distributes along range, but the ionosphere clutter generally distributes along Doppler. A fixed reference window will yield a biased threshold near the clutter region and potentially suppress targets nearby. Excessive false alarms are also observed from the clutters. In order to address these issues, an adaptive window is proposed and integrated into the switching CFAR. In this Adaptive Switching CFAR (AS-CFAR) the reference window adapts its shape to the background clutter by stretching its dimension which is parallel to the clutter distribution and shrinking the other dimension which is orthogonal to the clutter distribution. By this means the excessive false alarm rate can be decreased and targets probability of detection can be increased at the clutter transition region.

4.3.2.3 Block Diagram for Adaptive Switching CFAR

The adaptive switching CFAR has been implemented for HFSWR radar target detection with the following adaptations.

- 1) In the far range a slightly higher threshold has been implemented around the theoretical Bragg lines position to reduce the false detections caused by the Bragg lines residue. Although the detection probability is affected, the dual-thread (frequency) can recover the loss of weak targets because the targets' Doppler is linearly proportional to the carrier frequency while that of Bragg lines is not.

- 2) Within the ionospheric clutter the reference window is extended more in the Doppler and less in range to reduce the false alarm.

The block diagram of the algorithm is shown in Figure 4-10, and the corresponding procedures are listed as follows:

Step 1. Parameters initialization

Step 2. Go through the entire test cells in order of range, Doppler and then beam; stop and return to the main program if the last test cell has been examined, otherwise go to step 3.

Step 3. Judge the local situation around test cell in range-Doppler map based on the variance map; if it is homogeneous go to step 4, otherwise go to step 5.

Step 4. Apply CA-CFAR detector, and record the detection results if the threshold is crossed; go to step 2.

Step 5. Judge if the test cell is near ionospheric clutter; yes go to step 6, otherwise go to step 7.

Step 6. If the test cell is near Bragg lines, use smallest of CFAR; if not, using adaptive window size CFAR. Go to step 2.

Step 7. If the test cell is not within the ionospheric clutter, apply regular OS-CFAR; otherwise apply the adaptive window OS-CFAR. Go to step 2.

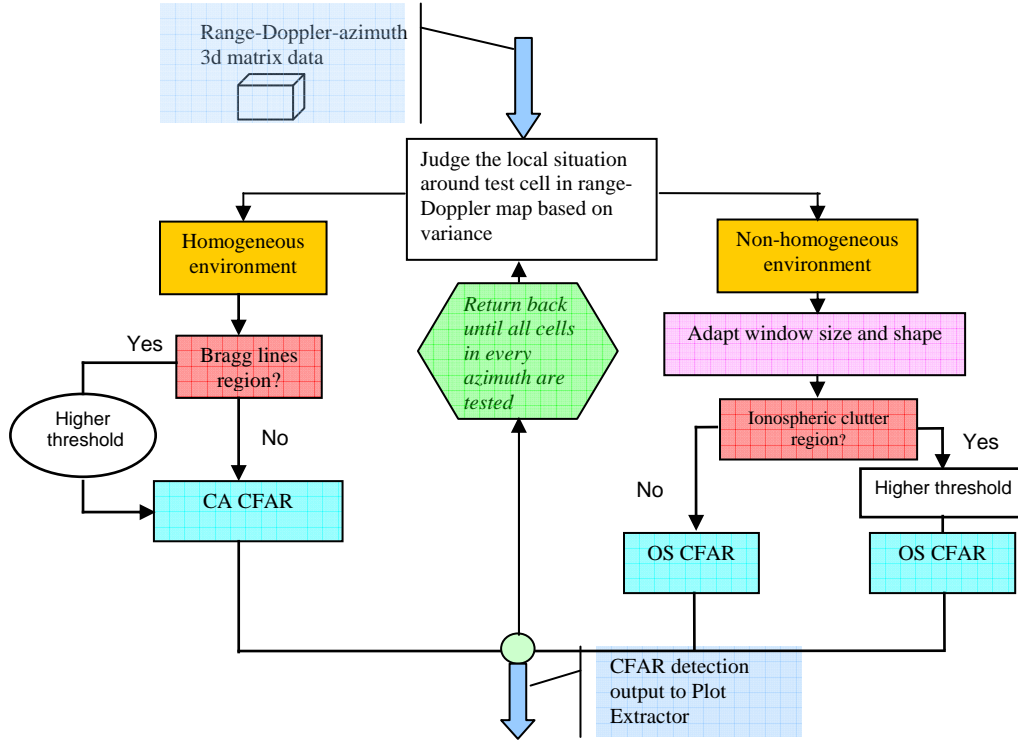


Figure 4-10 Block diagram of adaptive switching CFAR detector

4.4 Performance Analysis

4.4.1 Homogeneous Background

In the CA-CFAR processor, the noise power is estimated by the mean level of the cells in the reference window (N background cells). So we have

$$Z = \sum_{i=1}^N \frac{x_i}{N}$$

where $\{x_i\}$ are the reference cells following the IID exponential distribution at the homogeneous situation. It is well known that *the density function of the sum of N statistically independent random variables is the $(N-1)$ -fold convolution of the N individual density functions [67]*. Then the PDF of the variable Z is

$$\begin{aligned}
f_z(Z) &= f_1(x) * f_2(x) * \dots * f_N(x) \\
&= \left[\int_0^Z \frac{1}{2\mu} \exp\left(\frac{-x}{2\mu}\right) \frac{1}{2\mu} \exp\left(\frac{-Z+x}{2\mu}\right) dx \right] * f_3(x) * \dots * f_N(x) \\
&= \left[\left(\frac{1}{2\mu}\right)^2 Z \exp\left(\frac{-Z}{2\mu}\right) \right] * f_3(x) * \dots * f_N(x) \\
&\dots \\
&= \left(\frac{1}{2\mu}\right)^N \frac{Z^{N-1}}{(N-1)!} \exp\left(\frac{-Z}{2\mu}\right)
\end{aligned} \tag{4.8}$$

And the corresponding false alarm probability is given by

$$\begin{aligned}
P_{fa} &= E_z \{ P[x > TZ | H_0] \} \\
&= E_z \left\{ \int_{TZ}^{\infty} \frac{1}{2\mu} \exp\left(-\frac{x}{2\mu}\right) dx \right\} \\
&= E_z \left\{ -\exp\left(-\frac{x}{2\mu}\right) \Big|_{TZ}^{\infty} \right\} \\
&= \int_0^{\infty} \exp\left(-\frac{TZ}{2\mu}\right) f_z(Z) dZ \\
&= \int_0^{\infty} \exp\left(-\frac{TZ}{2\mu}\right) \left(\frac{1}{2\mu}\right)^N Z^{N-1} \exp\left(-\frac{Z}{2\mu}\right) \frac{1}{(N-1)!} dZ \\
&= \int_0^{\infty} \frac{-1}{(N-1)!(T+1)} \left(\frac{Z}{2\mu}\right)^{N-1} d \exp\left(-\frac{(T+1)Z}{2\mu}\right) \\
&= \frac{-1}{(N-1)!(T+1)} \left(\frac{Z}{2\mu}\right)^{N-1} \exp\left(-\frac{(T+1)Z}{2\mu}\right) \Big|_0^{\infty} - \int_0^{\infty} \frac{-1}{(N-1)!(T+1)} \exp\left(-\frac{(T+1)Z}{2\mu}\right) d \left(\frac{Z}{2\mu}\right)^{N-1} \\
&= \int_0^{\infty} \frac{-1}{(N-2)!(T+1)^2} \left(\frac{Z}{2\mu}\right)^{N-2} d \exp\left(-\frac{(T+1)Z}{2\mu}\right) \\
&\dots \\
&= \frac{-1}{(T+1)^N} \exp\left(-\frac{(T+1)Z}{2\mu}\right) \Big|_0^{\infty} \\
&= (T+1)^{-N}
\end{aligned} \tag{4.9}$$

From Eq (4.9), the constant factor T is calculated as

$$T = P_{fa}^{\frac{1}{N}} - 1 \tag{4.10}$$

Moreover the detection probability is determined by replacing 2μ with $2\mu(1+S)$:

$$P_d = \left[1 + \frac{T}{1+S} \right]^{-N} \quad (4.11)$$

In the OS-CFAR processor the noise power is estimated by taking the k^{th} largest sample in the reference window. So the variable Z has the PDF

$$\begin{aligned} f_z(Z) &= k \binom{k}{N} [1 - P(x \leq Z)]^{k-1} [P(x \leq Z)]^{N-k} f(Z) \\ &= k \binom{k}{N} \left[\exp\left(-\frac{Z}{2\mu}\right) \right]^k \left[1 - \exp\left(-\frac{Z}{2\mu}\right) \right]^{N-k} \frac{1}{2\mu} \end{aligned} \quad (4.12)$$

Therefore the false alarm probability is

$$\begin{aligned} P_{fa} &= E_z \{ P[x > TZ \mid H_0] \} \\ &= E_z \left\{ \int_{TZ}^{\infty} \frac{1}{2\mu} \exp\left(-\frac{x}{2\mu}\right) dx \right\} \\ &= \int_0^{\infty} \exp\left(-\frac{TZ}{2\mu}\right) f_z(Z) dZ \\ &= \int_0^{\infty} \exp\left(-\frac{TZ}{2\mu}\right) k \binom{k}{N} \left[\exp\left(-\frac{Z}{2\mu}\right) \right]^k \left[1 - \exp\left(-\frac{Z}{2\mu}\right) \right]^{N-k} \frac{1}{2\mu} dZ \\ &= \frac{N!}{(N-k)!(k-1)!} \int_0^{\infty} \exp\left(-\frac{(T+k)Z}{2\mu}\right) \left[1 - \exp\left(-\frac{Z}{2\mu}\right) \right]^{N-k} d\frac{Z}{2\mu} \\ &= \frac{N!}{(N-k)!(k-1)!} \int_0^{\infty} \frac{-1}{T+k} \left[1 - \exp\left(-\frac{Z}{2\mu}\right) \right]^{N-k} d \exp\left(-\frac{(T+k)Z}{2\mu}\right) \\ &\dots\dots \\ &= \prod_{i=k}^N \frac{i}{(T+i)} \end{aligned} \quad (4.13)$$

From Eq (4.13), it can be observed that the constant factor T is a function of false alarm probability and parameter k . The corresponding detection probability is

$$P_d = \prod_{i=k}^N \frac{i}{\left(\frac{T}{1+S} + i \right)} \quad (4.14)$$

In Figure 4-11 the detection performances of the CA-CFAR and OS-CFAR are plotted as a function of the signal to noise ratio in the homogeneous background given

the probability of false alarm and the reference window size (excluding the test cell). It is shown that the CA-CFAR has the higher detection probability for the same SNR, and the detection probability of OS-CFAR is worse when the parameter k increases.

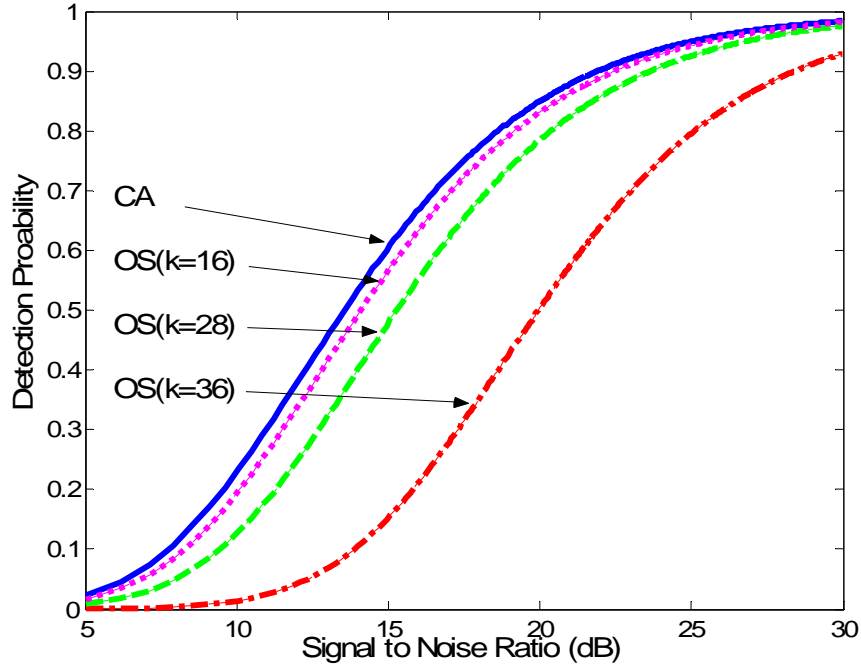


Figure 4-11 The detection probability of CA- and OS-CFAR vs SNR ($P_{fa} = 10^{-6}$ and $N = 40$)

4.4.2 Non-homogeneous Background

The clutter transition and multi-targets are two main concerns in a non-homogeneous background. In HFSWR systems the existing sea clutter and ionosphere clutter cause the degradation of the target detection severely. In this section we analyze the performances of CA-CFAR and OS-CFAR in clutter transition background.

Assuming there are only two different noise distributions in the background; white noise reference cells have $\lambda_1 = \mu$ while clutter reference cells have $\lambda_1 = \mu(1+C)$, where

factor C is the clutter to noise ratio. In the reference window assume there are r cells from clutter background and the other $N - r$ cells contain only background noise.

Then the PDF of the variable Z in the CA-CFAR is modified as

$$\begin{aligned} f_z(Z) &= f_1(x) * f_2(x) * \dots * f_N(x) \\ &= \int_0^Z f_{z_1}(Z_1) f_{z_2}(Z - Z_1) dZ_1 \end{aligned} \quad (4.15)$$

where Z_1 is the sub-sum of the clutter cells and Z_2 is the sub-sum of the noise cells:

$$\begin{aligned} f_{z_1}(Z_1) &= \left[\left(\frac{1}{2\mu(1+C)} \right)^r \frac{Z_1^{r-1}}{(r-1)!} \exp\left(\frac{-Z_1}{2\mu(1+C)} \right) \right]; \\ f_{z_2}(Z_2) &= \left[\left(\frac{1}{2\mu} \right)^{N-r} \frac{Z_2^{N-r-1}}{(N-r-1)!} \exp\left(\frac{-Z_2}{2\mu} \right) \right] \end{aligned}$$

If the test cell is from noise background the false alarm probability is

$$\begin{aligned} P_{fa} &= E_z \left\{ \int_{TZ}^{\infty} \frac{1}{2\mu} \exp\left(-\frac{x}{2\mu} \right) dx \right\} \\ &= \int_0^{\infty} \exp\left(-\frac{TZ}{2\mu} \right) f_z(Z) dZ \\ &= \int_0^{\infty} \exp\left(-\frac{TZ}{2\mu} \right) \int_0^Z f_{z_1}(Z_1) f_{z_2}(Z - Z_1) dZ_1 dZ \\ &= \int_0^{\infty} f_{z_1}(Z_1) \int_{Z_1}^{\infty} \exp\left(-\frac{TZ}{2\mu} \right) f_{z_2}(Z - Z_1) dZ dZ_1 \\ &= \int_0^{\infty} f_{z_1}(Z_1) \exp\left(-\frac{TZ_1}{2\mu} \right) dZ_1 \int_0^{\infty} f_{z_2}(Z_2) \exp\left(-\frac{TZ_2}{2\mu} \right) dZ_2 \\ &\dots \\ &= [1 + (1+C)T]^{-r} [1+T]^{r-N} \end{aligned} \quad (4.16)$$

Otherwise, the test cell is from the clutter background and the false alarm probability is

$$\begin{aligned} P_{fa} &= E_z \left\{ \int_{TZ}^{\infty} \frac{1}{2\mu(1+C)} \exp\left(-\frac{x}{2\mu(1+C)} \right) dx \right\} \\ &= [1+T]^{-r} \left[1 + \frac{T}{1+C} \right]^{r-N} \end{aligned} \quad (4.17)$$

In the OS-CFAR the false alarm probability for the test cell from the noise background is formulated [68] as

$$P_{fa} = T \sum_{i=k}^N \sum_{L=\max(0,i-r)}^{\min(i,N-r)} \binom{L}{N-r} \binom{i-L}{r} \sum_{j_1=0}^L \sum_{j_2=0}^{i-L} \frac{\binom{j_1}{L} \binom{j_2}{i-L} (-1)^{j_1+j_2}}{N-r-L+T+j_1+(j_2+r-i+L)/(1+C)} \quad (4.18)$$

When the test cell is from the clutter region, the P_{fa} is obtained from the above results by

replacing T with $\frac{T}{1+C}$.

It is shown that the probabilities of false alarm vary with the number of the clutter cells, the clutter to noise ratio and the test cell's homogeneity. And the scalar number T estimated from the probability of false alarm is not constant over all reference windows in the clutter-varied region. So we need to increase T to meet the desired system false alarm rate. Due to its adaptive footprint characteristics, the AS-CFAR will have better performance than both OS-CFAR and CA-CFAR in the non-homogeneous background.

4.5 Experiments

In order to demonstrate the advantage of our proposed algorithm a comparison is undertaken using data sets collected from the Canada East Coast radars. The detectors with different CFAR algorithms are connected with the same online Plot Extractor and Tracker of the HFSWR system.

The first data set is collected from Teleost trail with a known target (Teleost). Data are processed using both conventional OS-CFAR and AS-CFAR. Tracking results are compared between the two CFAR detectors for Teleost. Improved tracking performance is observed for Teleost due to AS-CFAR (track target further in the clutter region) as

shown in Figure 4-12, where the OS-CFAR detections are indicated by circles and AS-CFAR detections are indicated by crosses. The 2-D power spectrum is shown in Figure 4-13 with the detections from AS-CFAR indicated by black crosses whereas those from OS-CFAR are indicated by circles. It can be observed that the target near strong ionospheric clutter can only be detected by AS-CFAR.

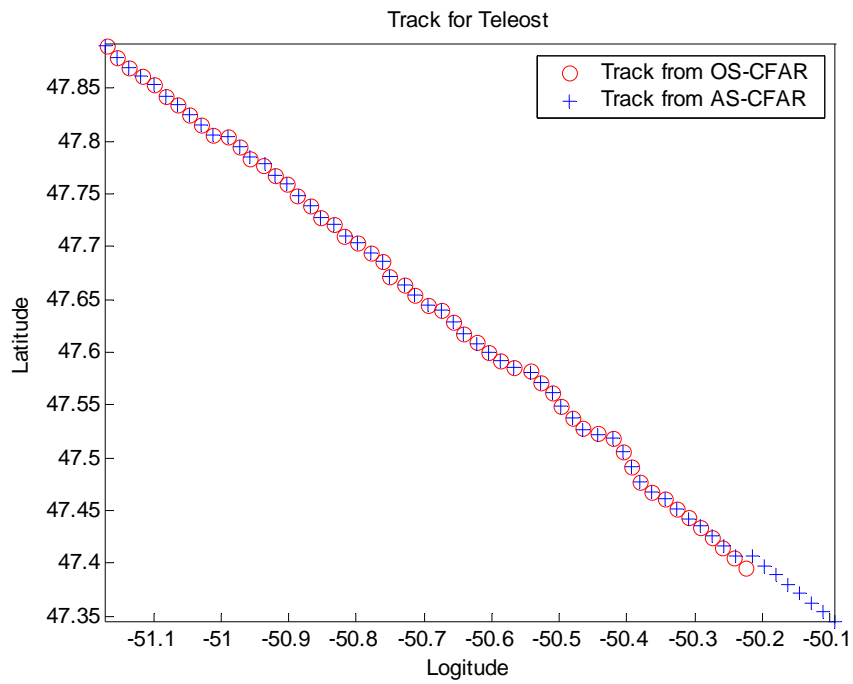


Figure 4-12 Tracking results for Teleost

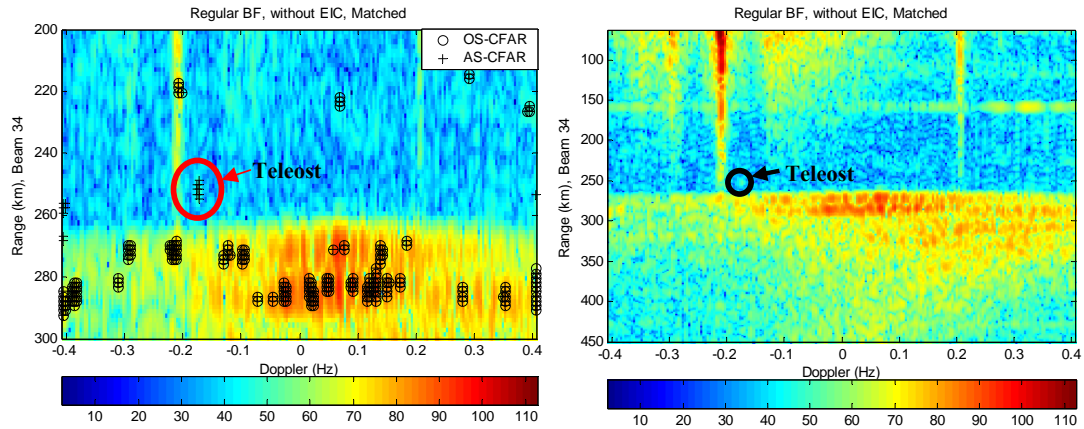


Figure 4-13 Spectrum of Teleost near the ionospheric clutter

The second data set was collected during the “Pre-Alix” trial in 2004. Again the data are processed using both OS-CFAR and AS-CFAR. Tracking results are compared between the two CFAR detectors for a target near ionospheric clutter. The track data is presented in Figure 4-14, where the blue dots represent detections while the red dots represent coasted reports (The tracker self updating without detections). From the plot it can be observed that track splitting occurs when OS-CFAR is used. Figure 4-15 presents the same data but processed with the AS-CFAR. From the figures it can be observed that the track splitting has been avoided. The 2-D power spectrum for the target is shown in Figure 4-16 with the detections from AS-CFAR indicated by black crosses and those from OS-CFAR indicated by circles. It can be observed that when the target is near strong ionospheric clutter it can only be detected by AS-CFAR.

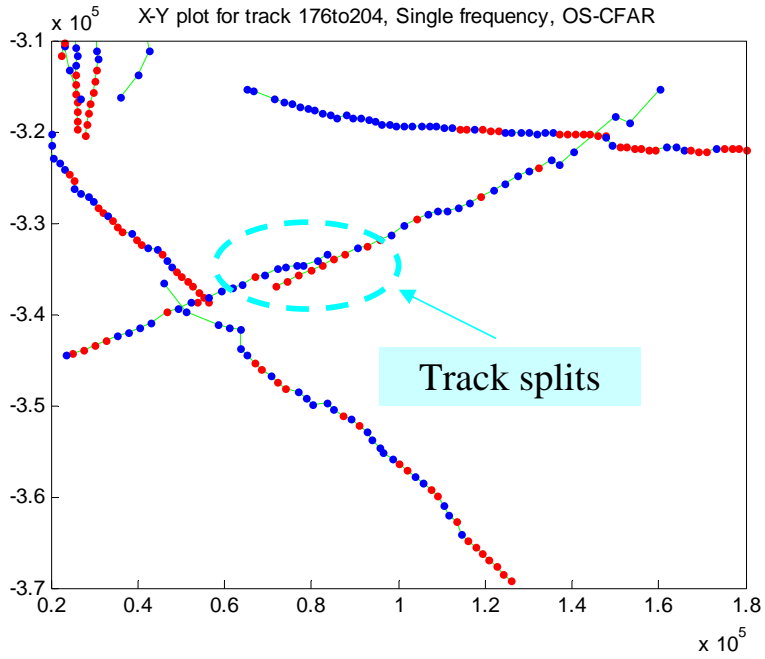


Figure 4-14 Tracking results after OS-CFAR detection

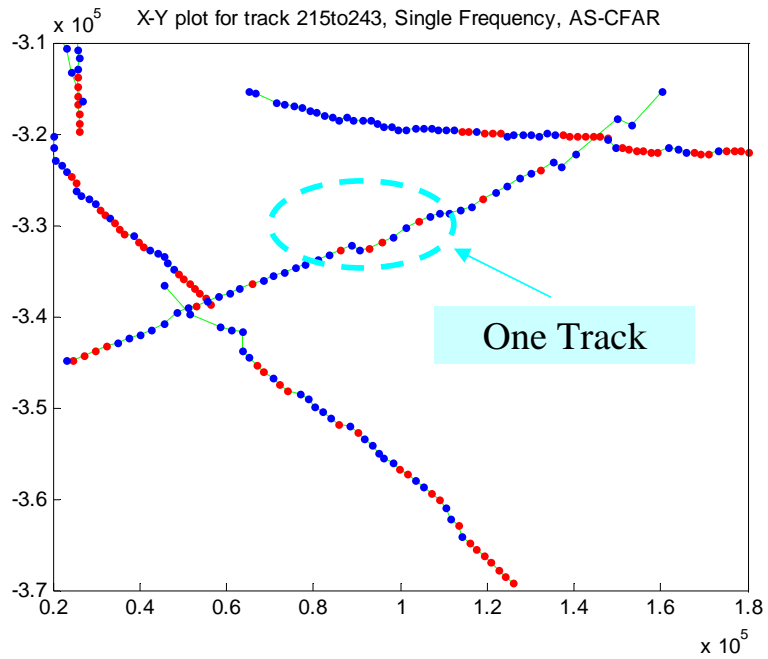


Figure 4-15 Tracking results after AS-CFAR detection

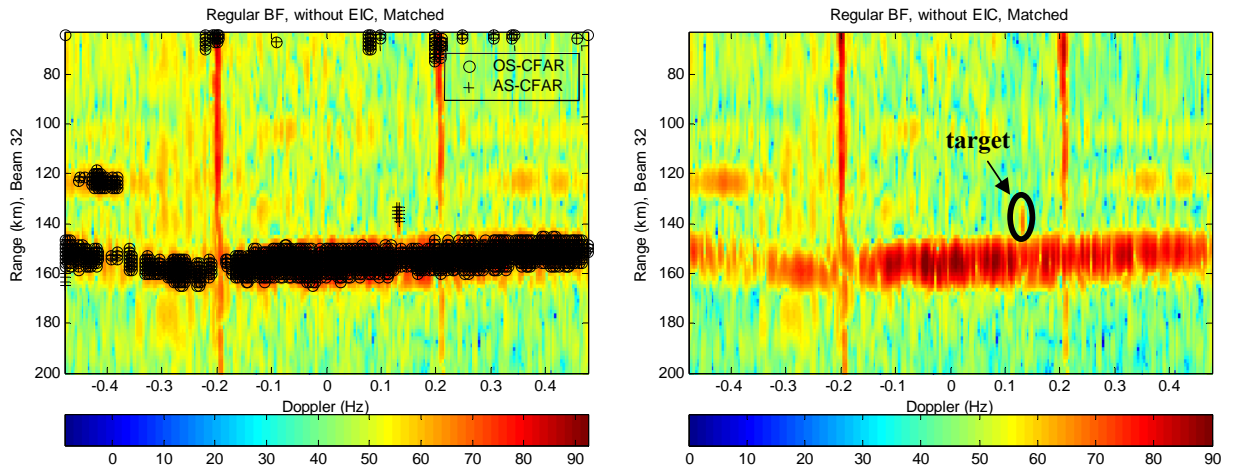


Figure 4-16 Power spectrum of the target near the ionospheric clutter

The third data set is collected from Cape Race with carrier frequency 3.2MHz. The collecting time begins at 12:24:23 and ends at 18:18:19 on Dec 1, 2004. The track results for OS-CFAR and AS-CFAR are presented in Figure 4-17 and Figure 4-18 respectively. It is shown that the AS-CFAR has better performance compared with OS-CFAR in several aspects: firstly AS-CFAR has more far-range tracks and also more updates in far-range tracks because CA-CFAR works better at the homogeneous background; secondly the adaptive window rule has provided more updates and smoother tracks near clutter transition. The detection details for the tracks are shown in Table 4-1. The AS-CFAR (476 total associated plots) produces approximately 14% more associated plots at the output of the tracker than the OS-CFAR (417 total associated plots) during the 6 hours data. This indicates the improved probability of detection from AS-CFAR. Moreover we compare the detection numbers after CFAR algorithms and the plot numbers after Plot Extractor in Figure 4-19. It is found that the OS-CFAR has 43780 detections and 67 plots per CIT on average while the AS-CFAR has 25323 detections and 97 plots per CIT on

average. That means that in this data set the OS-CFAR has 50% more false detections but 45% fewer target plots than the AS-CFAR.

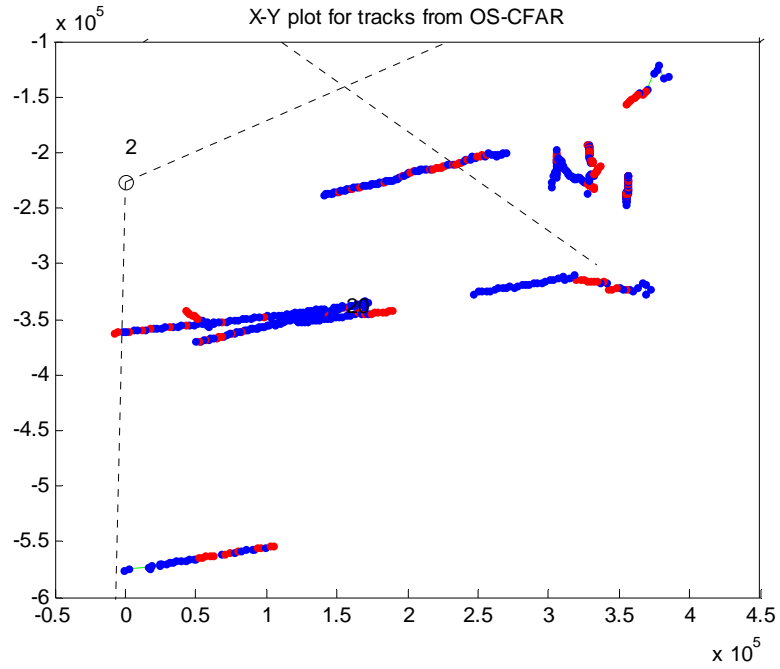


Figure 4-17 Tracking results after OS-CFAR detection

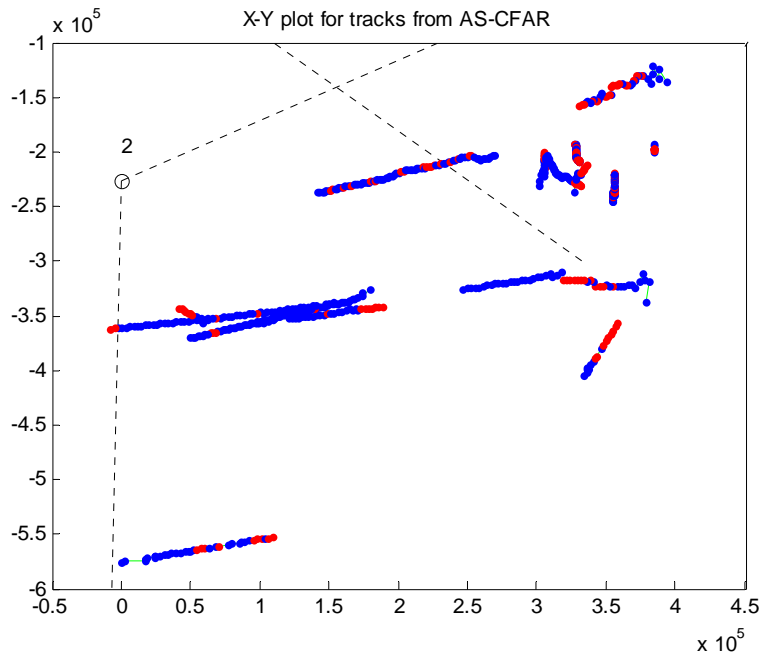


Figure 4-18 Tracking results after AS-CFAR detection

Table 4-1 The duration and position of all tracks for OS-CFAR and AS-CFAR

	ID	Time		Range (km)		Azimuth (deg.)		Updates #
		Initial	end	Initial	End	Initial	End	
OS	12	12:26	18:20	140.9	270.6	94.5	84.6	59
AS	12	12:30	18:20	142.3	270.6	94.3	84.6	63
OS	13	12:30	18:20	355.3	356.3	92.3	89.6	49
AS	13	12:30	18:20	355.3	356.3	92.3	89.6	53
OS	15	12:44	14:33	167.3	208.6	140.6	126.1	21
AS	15	12:26	14:33	162.6	208.7	143.1	126.1	25
OS	17	13:10	18:20	202.7	152.7	123.5	160.9	63
AS	16	12:57	18:20	205	152.7	118.9	160.9	71
OS	23	15:51	16:48	396.9	373.8	76.1	77.3	7
AS	23	15:30	18:07	403.9	343.8	77.1	78.7	21

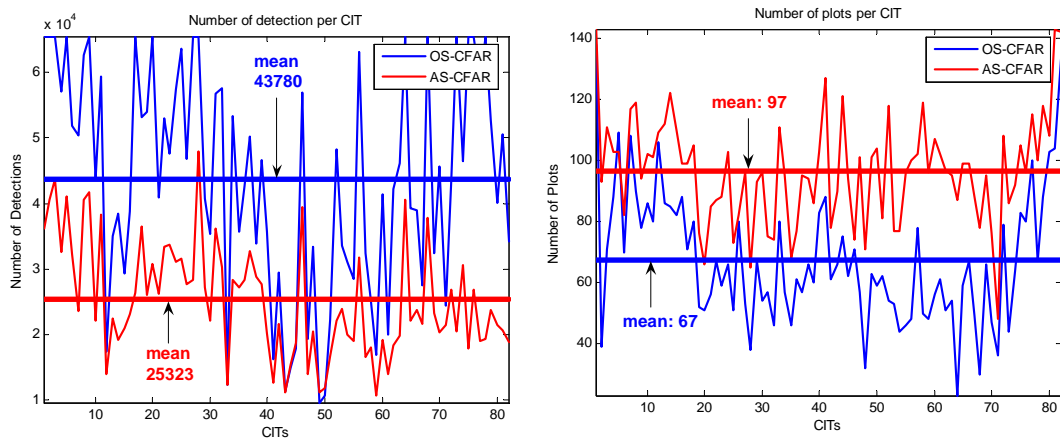


Figure 4-19 The number of detection and number of plots for OS-CFAR and AS-CFAR

4.6 Summary

We have presented a novel adaptive switching CFAR technique to improve the HFSWR detection and tracking performance. A variance-based threshold is calculated for

switching between CA- and OS-CFAR algorithms in order to increase the detection probability of the original OS-CFAR at far range area (homogeneous background). Based on the specific characteristic of the sea clutter and ionospheric clutter in the range-Doppler map, the adaptive window rule is studied and applied in the AS-CFAR to decrease the false alarms and increase the detection probability in the strong clutter regions. We have presented the theoretical performance analysis for the CA- and OS-CFAR for both homogeneous and non-homogeneous backgrounds. The experiments validate the proposed algorithm's effectiveness. Extensive real data analyses from various tests and trials consistently verify that AS-CFAR provides about 14% improvement in probability detection and reduces about 50% false alarms compared to these of OS-CFAR.

Chapter 5 - Bayesian Methods for Target Detection

The common detection method in HF radar is based on Doppler processing with a long dwell time to discriminate the ships from the background sea clutter and noise in the frequency spectrum. However when the target moves at a similar radial velocity close to or lower than that of the Bragg waves, it is masked to some level by the first-order or high-order sea clutter. So characteristics other than the Doppler frequency may be effectively extracted to discriminate the target signal from the sea clutter signal. In this chapter the time-domain characteristic of the received signal is investigated to improve the probability of the target detection in HF radar.

In general the state-space and observation equations are applied for the processing model having the form

$$\begin{aligned}\mathbf{x}(t) &= \mathbf{f}_t(\mathbf{x}(t-1), \mathbf{u}(t)) \\ \mathbf{y}(t) &= \mathbf{g}_t(\mathbf{x}(t), \mathbf{v}(t))\end{aligned}\tag{5.1}$$

where $\mathbf{y}(t)$ is a vector of observations, $\mathbf{x}(t)$ is a vector of state, $\mathbf{g}_t(\cdot)$ is a measurement function, $\mathbf{f}_t(\cdot)$ is a system transition function, $\mathbf{u}(t)$ and $\mathbf{v}(t)$ are noise vectors respectively.

The common assumptions are that the analytical forms of the functions and the

distributions of the noises are known. Based on the observations $\mathbf{y}(t)$ and the assumptions, the objective is to estimate the state vector $\mathbf{x}(t)$ recursively. The method that has been most frequently investigated and applied in practice is the Kalman filter. The Kalman filter is optimal in the case where the equations are linear and the noises are independent, additive, and Gaussian. For situations where the models are nonlinear or/and the noise is non-Gaussian, various approximate methods have been proposed to provide reasonable sub-optimal solutions such as the extended Kalman filter or Sequential Monte Carlo methods.

Sea clutter, the main noise component affecting HF radar detection, has been found not to be a simple Gaussian distribution. Several potential effective models are reviewed in Section 5.1. Based on this non-Gaussian characteristic of sea clutter, some modified processors have been developed for on-line or off-line signal detection in HF radar.

The extended Kalman filter, utilizing the first term in a Taylor expansion of the nonlinear function to provide approximation, is proposed in section 5.2 to resolve targets from sea clutter with similar Doppler frequencies; this difficult situation is not satisfactorily addressed using conventional Doppler processing. Instantaneous phase difference is estimated to resolve co-located, co-channel target/interference, instead of using only phase and amplitude information as with the coherent integration.

The Reversible Jump Markov Chain Monte Carlo (JMCMC) [93] has been developed for model determination and classification in white or even spatially colored Gaussian noise with known covariance matrix. However the existing RJMCMC methods assumes a Gaussian distribution (white or colored), and cannot be directly applied to the DOA and target number estimation in HF radar. We propose in section 5.3 to incorporate a pre-

whitening process prior to the application of RJMCMC to improve the detection performance [110]. The adaptive space-time sea clutter pre-whitening is achieved using an extended generalized sidelobe canceller (GSC)-like procedure similar to [111]. The non-stationary property of sea clutter may degrade the detection performance of modified RJMCMC.

For this situation, the on-line sequential Monte Carlo method (such as particle filter) is preferred to afford updated detection information based on recent and current radar data. Particle filtering is one numerical approach to recursively compute the relevant probability distributions through important sampling to approximate the probability distributions with discrete random measures. Further study about particle filter is listed in section 5.4.

5.1 Sea Clutter Model Analysis

Sea clutter is the radar backscatter of the electromagnetic energy from an ocean surface [38][69]. The sea echo depends not only on the sea state such as the wave height, wind speed, direction of the waves relative to that of the radar beam and so on, but also on radar parameters such as frequency, polarization, grazing angle, and, to some extent, the size of the area under observation. Most previous development in the sea clutter model has focused on microwave radar. We first review the basic ideas for modeling sea clutter at microwave, and later develop HF radar sea clutter model.

5.1.1 Microwave Radar Sea Clutter Models Review

At low resolutions (the resolution cell, or area illuminated by radar is relatively large), the probability distribution of the return signal's envelop can be well approximated by the

Rayleigh distribution [70]. At high resolutions and low grazing angles, the clutter is found to be more ‘spiky’ than account for by Rayleigh. Several heavier tailed two-parameter distributions such as log-normal distribution [71], Weibull distribution [72] or compound K distribution [73][75][76][78] are proposed to provide better fits to the amplitude of sea clutter than Rayleigh distribution. The basic idea [74] of the K-distribution is to assume the overall amplitude z of sea clutter is represented by the product of two independent random variables: $z = xy$, where x has a chi distribution due to the capillary waves (short wavelength, from surface tension) and has a long correlation time, and where y has a Rayleigh distribution due to the gravity waves (long wavelength).

Some researchers argue that the radar backscatter from an ocean surface is deterministic chaos other than stochastic distributions. For a fixed surface geometry, a slight deviation in the angle of incidence may produce a large change in the backscattering process. This high sensitivity of the scattering process to the initial conditions is suggestive of the possibility of sea clutter being a chaotic scattering phenomenon [78]. The surrogate data analysis [79][[80] based on the correlation dimension and Laypunov exponents is employed to prove the nonlinear dynamics of the sea clutter. However as Davies [81] points out, such invariants can not be used to diagnose chaos by themselves, and their use make sense only in the context of the data being deterministic to start with. Unsworth et al. [82] re-examine two principal chaotic invariants, the ‘maximum likelihood estimation of the correlation dimension’ and ‘false nearest neighbors’, through several experimental analyses. Both invariants are shown to falsely suggest chaos for known stochastic time series. Haykin et al. [83] modify the chaotic conclusion that the sea clutter is a nonlinear dynamical process with the

nonlinearity depending on the sea state being moderate or high and the ocean waves moving toward or away from the radar. Moreover it is not surprising that the dynamic reconstruction of the sea clutter using experimental time series is very difficult. The possible explanations for the non-chaotic results [82] are given in [83].

An AR process can approximate the Fourier Spectrum of a dynamical system, which describes the main exponential elements of sea clutter. Bouvier et al. [90] propose to model sea clutter by the multiplication of a modulating random variable and a correlated complex Gaussian process which is obtained by filtering a complex white Gaussian process through a low order AR model. Haykin et al. [83] model the sea clutter as a time-varying complex AR process which is fit to the data in a sliding window.

5.1.2 HF Radar Sea Clutter Models Review

The sea clutter models proposed for microwave radar have been tested with HF radar. Test procedures for K-distribution based on a rank test are presented by Zoubir in his paper [77] for HF radar. Dong [113] utilizes the chaotic dynamics to analyze the dynamical characteristic of the sea clutter in HF radar and concludes the possible connection between them. This possible chaotic characteristic of the sea clutter has been applied to improve the performance of the target detection through clutter cancellation [114]. The radar receiver data are used to build up the attractor and then subtracted the corresponding prediction of the chaotic process through the local linear fits method to improve the target SNR. Martin et al. [91] apply an AR technique to remote sea current sensing for HF radar. This approach is more accurate in determining the radial component of sea current than is the conventional FFT based method. The algorithm can

be implemented in real time and can form the basis for further signal processing improvements in a HF radar system.

In 1955 Crombie [128] first found that there were two well-defined spikes placed around the radar carrier frequency in the Doppler power spectrum of the sea clutter. In addition Crombie found that the displacement of these spikes appeared to vary with the square root of the carrier frequency and their amplitudes were dependent on wind and sea state conditions. These are called the first order Bragg lines since they are similar to the X-ray scattering mechanism in crystals identified by W. L. Bragg. Although all sea waves interact with the radar wave, only the gravity waves with exactly one half of the radar wavelength and which are moving toward (positive Doppler shift) and away (negative Doppler shift) from the radar behave as a diffraction grating and reinforce echoes. All gravity sea waves of given wavelength are known to have a given velocity:

$$v = \sqrt{gL/2\pi} \quad (5.2)$$

where g is the acceleration of gravity and L is the wavelength of the gravity wave. We can calculate the Doppler shift (Δf) of Bragg lines:

$$\Delta f = \pm 2v/\lambda = \pm\sqrt{g/\pi\lambda} \quad (5.3)$$

where λ is the radar wavelength. In fact this finding forms the basis for remote sensing of sea states.

Figure 5-1 presents an example of the measured surface-wave sea clutter Doppler spectrum at carrier frequency 3.1 MHz. The back-scattered clutter is taken at range 100 km from the receiver antenna, and the Fourier transform is taken over 164 s. The first order Bragg lines exist at about $\pm 0.18\text{Hz}$. It is obvious that there is a continuum spectrum around the first order Bragg lines, and this continuum is of second or higher order

scattering. There are a few reasonable physical models for second order scattering [9]: 1) The sea waves are not sinusoidal but trochoidal (sharp crest and broad trough) caused by the circular motion of water particles; 2) Radar waves are scattered from two sea waves traveling at a right angle difference in direction; 3) Sea waves interact with each other and result in a wave with the exactly half wavelength of the radar wave, which contributes to the continuum second order spectrum.

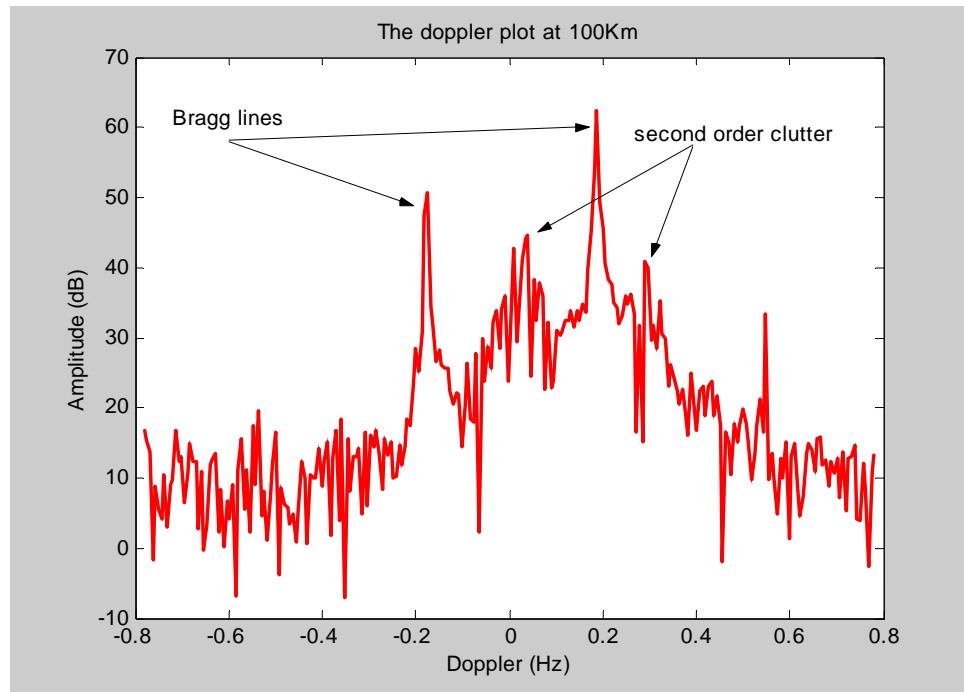


Figure 5-1 Measured HF radar sea clutter at 3.1 MHz transmitted carrier frequency. The zero Doppler frequency position corresponds to the carrier frequency. Bragg lines show at frequencies ± 0.18 Hz.

The first order Bragg lines are dominant and usually blind the nearby target detection. An important model of sea clutter for HF radar is introduced by Khan in his paper [84], where the dominant components of sea clutter are modeled by two narrow-band signals with slowly time-varying frequencies (angle modulated), centered on the first Bragg frequencies. This time-varying model has a significant impact on the processing of HF

radar data in the background of ocean, and a series of papers [85][86][87] follow this model to improve target detection or sea state parameters measurement. The author concludes that within a short observation time (less than one minute) the sea clutter signals are strictly non-stationary. It is obvious that optimal processing of such HF radar data can be achieved by a low-order linear prediction filter with time-varying coefficients. Since the prediction error filter (PEF) is an all-zero filter, it can be shown [88] that the transfer function of the PEF has M zeros on the unit circle at the locations corresponding to the angular frequencies of the M sinusoids in the signals. By this means the time-varying model for sea clutter is verified by Khan through an adaptive PEF. They show that the experimental results closely agree with the phase modulated clutter model. However application of their model fails to detect a target near the Bragg lines.

DiMonte and Arun [89] show that the time domain data (Hankel) matrix from multiple sinusoids has a rank equal to the number of sinewaves present even if their frequencies are slowly changing, and therefore the instantaneous frequencies can be estimated in a time-varying fashion using an iterative eigenstructure method. Applying this approach to beamformed sea clutter time series of range 84.5 km where there is a target with Doppler of -0.015 Hz, we obtain the frequency tracking results as shown in Figure 5-2. We observe that there are two lines with mean frequencies -0.1787 Hz and 0.1814 Hz, which correspond to the two Bragg lines. The ship target is tracked around frequency -0.014 Hz. The other two signals are considered to be higher order sea clutter. The tracking results can be better understood if we look into Figure 5-3, where there are obviously two other FM signals around frequencies 0.3 and 0.1 Hz after suppressing the first order Bragg lines at each sensor and beamforming the outputs.

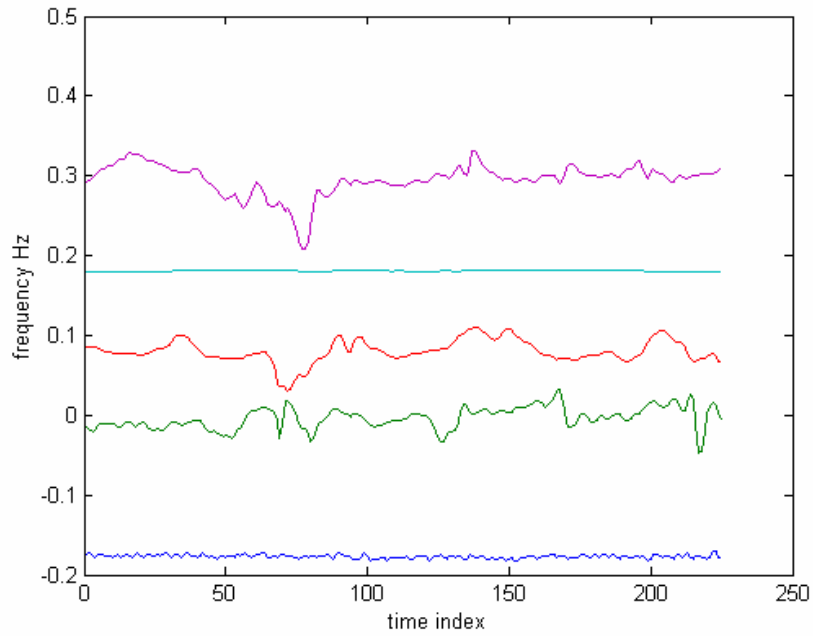


Figure 5-2 Doppler frequencies vs. time; means are [-0.1787 -0.0137 0.0795 0.1814 0.2879] Hz.

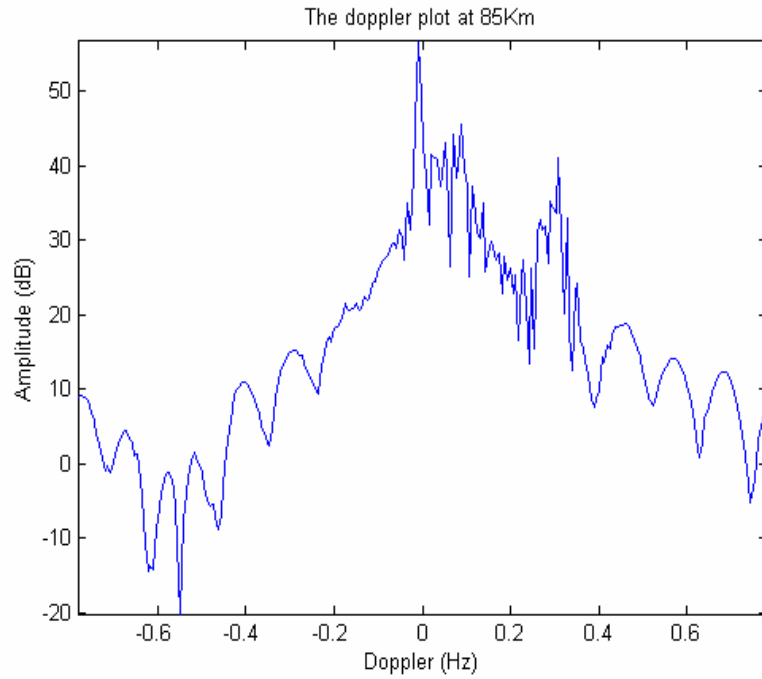


Figure 5-3 Doppler spectrum after suppressing the first order Bragg lines.

5.2 Signal Detection Based on Phase Tracking

In this section, we propose a detector which can resolve co-located targets (or target with interference) with similar Doppler frequencies. Instead of only using phase information in the coherent integration, our proposed detector tracks the phase modulation differences of the co-located, co-channel targets. The amplitude information of the targets can also be estimated and forwarded to the tracker. Simulations of the proposed method show promising results that targets with Doppler frequencies near Bragg lines can be detected.

5.2.1 Signal Model and Formulation

Similar efforts [120] [121] have been exercised in the field of communication theory, where digital phase-locked loops based on an extended Kalman filter (EKF) are used to separate co-channel sources. We formulate the problem for baseband radar signals. The signal model which we present is general enough that it may be applied to a number of multiple source problems; however in keeping within the application area of HF radar, we concentrate on the two source scenario (one target and Bragg line).

A state-space model similar to that in [120] can be extended to describe the radar signal's amplitude, phase and frequency processes, and their corresponding measurements. In the following we provide a brief description of the processing algorithms based on a first order low pass modulation assumption. However the algorithm can be readily adapted to other modulation models for different practical radar applications. The state equation for the i^{th} signal can be described as

$$\mathbf{x}_i(t+1) = \mathbf{\Phi}_i \mathbf{x}_i(t) + \mathbf{\Gamma}_i \mathbf{u}_i(t) \quad (5.4)$$

where $\mathbf{x}_i(t) = [\theta_i(t) f_i(t) A_i(t)]^T$ is the state vector with elements of phase, frequency and amplitude respectively. The state transition matrix Φ_i is the modulation model with the following form

$$\Phi_i = \begin{bmatrix} 1 & \phi_{\theta,i} & 0 \\ 0 & \phi_{f,i} & 0 \\ 0 & 0 & 1 \end{bmatrix} \quad (5.5)$$

where for first order low pass modulation $\phi_{\theta,i} = d_{\bar{f}_i} (1 - e^{-\alpha_i T_s}) / \alpha_i$ and $\phi_{f,i} = e^{-\alpha_i T_s}$. T_s is the sampling period; α_i is the modulation bandwidth and $d_{\bar{f}_i}$ describes the phase sensitivity to frequency. Γ_i is the process noise gain matrix relating the independent white Gaussian processes $\mathbf{u}_i(t)$:

$$\Gamma_i = \begin{bmatrix} \gamma_{\theta,i} & \gamma_{\theta f,i} & 0 \\ \gamma_{f\theta,i} & \gamma_{f,i} & 0 \\ 0 & 0 & 0 \end{bmatrix} \quad (5.6)$$

When there are N signals the state process model can be expressed as:

$$\mathbf{x}(t+1) = \Phi \mathbf{x}(t) + \Gamma \mathbf{u}(t) \quad (5.7)$$

where

$$\begin{aligned} \mathbf{x}(t) &= [\mathbf{x}_1^T(t) \mathbf{x}_2^T(t) \cdots \mathbf{x}_N^T(t)]^T \\ \mathbf{u}(t) &= [\mathbf{u}_1^T(t) \mathbf{u}_2^T(t) \cdots \mathbf{u}_N^T(t)]^T \\ \Phi &= \mathbf{I}_N \otimes \Phi_i \\ \Gamma &= \mathbf{I}_N \otimes \Gamma_i \end{aligned}$$

with \otimes denoting the Kronecker product and \mathbf{I}_N being the identity matrix. The measurement equation is inherently a nonlinear function of the state vector according to

$$y(t) = h(\mathbf{x}(t)) + v(t) \quad (5.8)$$

where $h(\mathbf{x}(t))$ is the observation function; $v(t)$ is $N(0, R_v)$ (Gaussian with mean zero and

covariance matrix R_v) distributed measurement noise; $y(t)$ is the actual measurement.

For N co-channel signals the observation function is

$$h(\mathbf{x}(t)) = \sum_{i=1}^N A_i(t) \sin(2\pi f_d t T_s + \theta_i(t)) \quad (5.9)$$

An EKF [122] is implemented to approximate the above models and provide the state estimates of the signals. The prediction update is as follows:

$$\hat{\mathbf{x}}(t|t-1) = \mathbf{\Phi} \hat{\mathbf{x}}(t-1|t-1) \quad (5.10)$$

$$\mathbf{P}(t|t-1) = \mathbf{\Phi} \mathbf{P}(t-1|t-1) \mathbf{\Phi}^T + \mathbf{Q}_u \quad (5.11)$$

where $\hat{\mathbf{x}}(t|t-1)$ and $\mathbf{P}(t|t-1)$ are the predicted state and predicted estimate covariance, respectively; and \mathbf{Q}_u is the covariance matrix of $\mathbf{u}(t)$.

The measurement updates are determined by the following equations:

$$\tilde{y}(t) = y(t) - h(\hat{\mathbf{x}}(t|t-1)) \quad (5.12)$$

$$S(t) = \mathbf{H}(t) \mathbf{P}(t|t-1) \mathbf{H}(t)^T + R_v \quad (5.13)$$

$$\mathbf{K}(t) = \mathbf{P}(t|t-1) \mathbf{H}(t)^T S(t)^{-1} \quad (5.14)$$

$$\hat{\mathbf{x}}(t|t) = \hat{\mathbf{x}}(t|t-1) + \mathbf{K}(t) \tilde{y}(t) \quad (5.15)$$

$$\mathbf{P}(t|t) = (\mathbf{I} - \mathbf{K}(t) \mathbf{H}(t)) \mathbf{P}(t|t-1) \quad (5.16)$$

$$\mathbf{H}(t) = \left. \frac{\partial h}{\partial \mathbf{x}} \right|_{\hat{\mathbf{x}}(t|t-1)} \quad (5.17)$$

where $\tilde{y}(t)$ is the innovation process, $S(t)$ is the innovation covariance, $\mathbf{K}(t)$ is the Kalman gain, $\hat{\mathbf{x}}(t|t)$ is the updated state estimate, and $\mathbf{P}(t|t)$ is the updated estimate covariance. The EKF observation matrix for two sources is:

$$\mathbf{H}^T(t) = \begin{bmatrix} \hat{A}_1(t|t-1)\cos(\hat{\theta}_1) \\ 0 \\ \sin(\hat{\theta}_1) \\ \hat{A}_2(t|t-1)\cos(\hat{\theta}_2) \\ 0 \\ \sin(\hat{\theta}_2) \end{bmatrix} \quad (5.18)$$

where $\hat{\theta}_i = 2\pi f_d t T_s + \hat{\theta}_i(t|t-1)$.

Our chosen measure of target separability is state observability. If the targets can be estimated or distinguished, their states should be observable. The observability is a function of the transition and observation matrices and can be examined by the observability Gramian:

$$M(t_0, t_f) = \sum_{t=t_0}^{t_f} \Phi^T(t, t_0) \mathbf{H}^T(t) \mathbf{H}(t) \Phi(t, t_0) \quad (5.19)$$

A system is uniformly completely observable if there is an interval $t_f > t_0$ such that $M(t_0, t_f)$ is positive definite [123]. For two co-channel signals, the states are observable as long as the mean frequencies are not in-phase or anti-phase as shown in [121]. Reduced state observability means increased estimation error variance, which reflects that the innovations process contains less useful information due to the reduced state information in the state measurement. This lack of confidence in the state measurement reduces the Kalman gain and leads to the domination of state prediction over the state measurement. In the following simulation section, we demonstrate that by tracking the phase modulation differences, it is feasible to detect a target close to a Bragg line.

5.2.2 Simulation

In order for the signals to be separated, their states must be estimated. Signal separation

may be decomposed into two operations: 1) initial state estimation or acquisition and 2) continuous state estimation or tracking. In the following we present two simulation results. In the first simulation, we generate two test signals with different frequency modulation bandwidths. In the second simulation we inject a simulated target into the real sea clutter and demonstrate the capability of discriminating a target near Bragg lines.

Simulation 1

In this simulation the targets bandwidths are $\alpha_1 = f_d/20$, $\alpha_2 = f_d/40$, $d_{f1} = d_{f2} = 1$ and the sampling rate is $f_s = 25f_d$ where f_d is the carrier frequency. The state estimate results are shown in Figure 5-4 and Figure 5-5 for a sample run. The estimator acquires the states after approximately 7 carrier cycles.

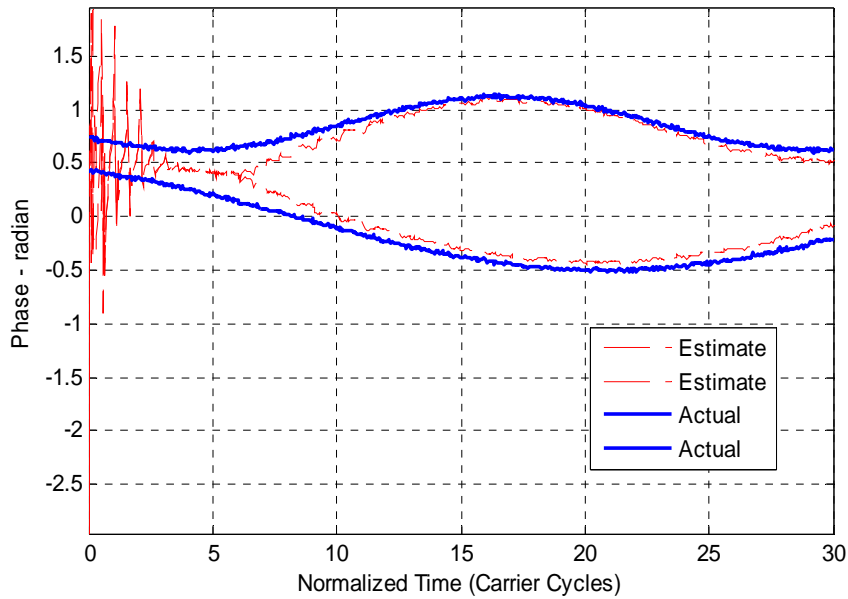


Figure 5-4 Phase modulation tracking; dashed traces represent estimation, and solid traces represent actual phase.

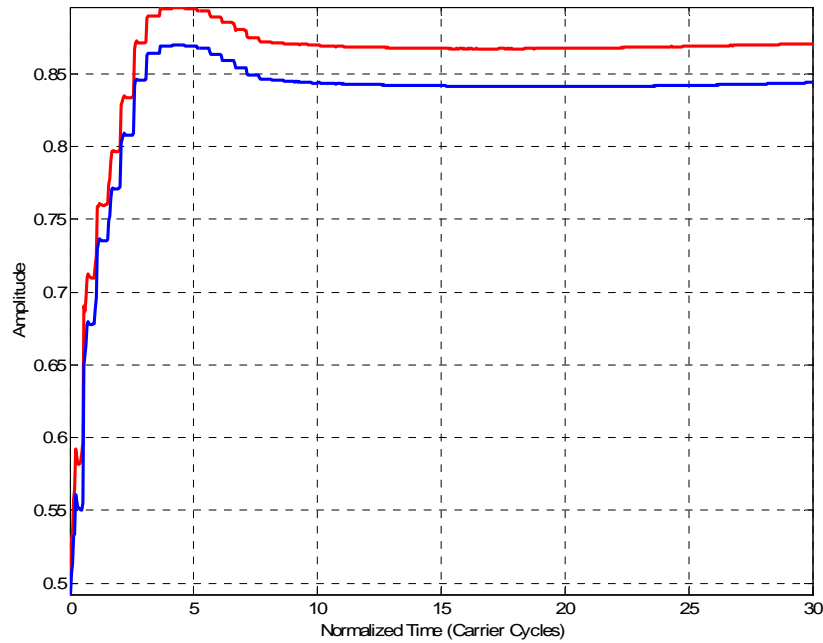


Figure 5-5 Amplitude tracking; true amplitude is 0.9 for each signal.

Simulation 2

In this simulation the ocean sea clutter is taken from 62 km with a synthetic target injected. The synthetic target is generated at frequency of 0.18 Hz, which is the same as Bragg line's mean Doppler. The modulation bandwidth is about 10%. The tracking results are shown in Figure 5-6 and Figure 5-7. The sea clutter is pre-filtered by a narrow bandpass filter centered at the Bragg line's mean frequency to reduce the other possible target or clutter's interference.

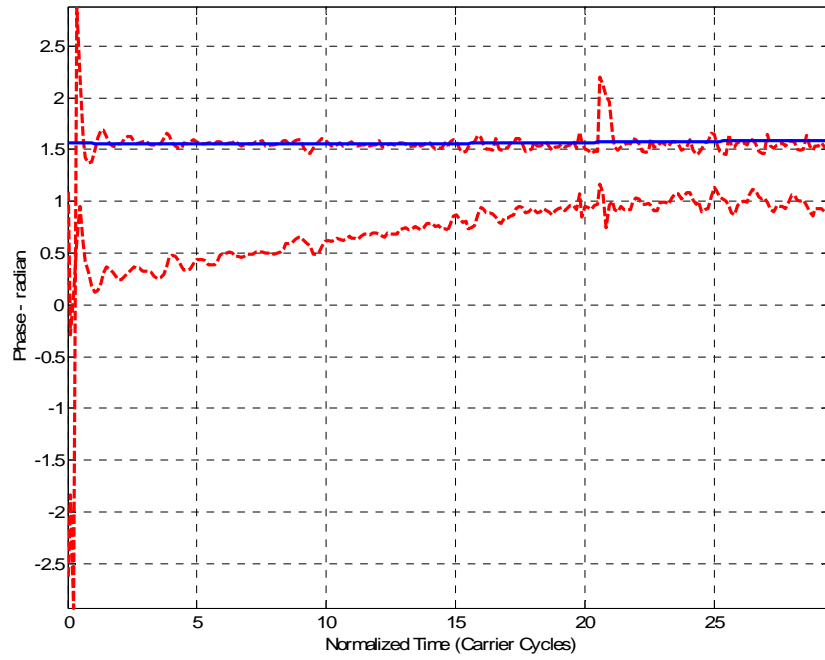


Figure 5-6 Phase modulation tracking; dashed traces represent estimation, and solid trace represents actual simulated target phase.

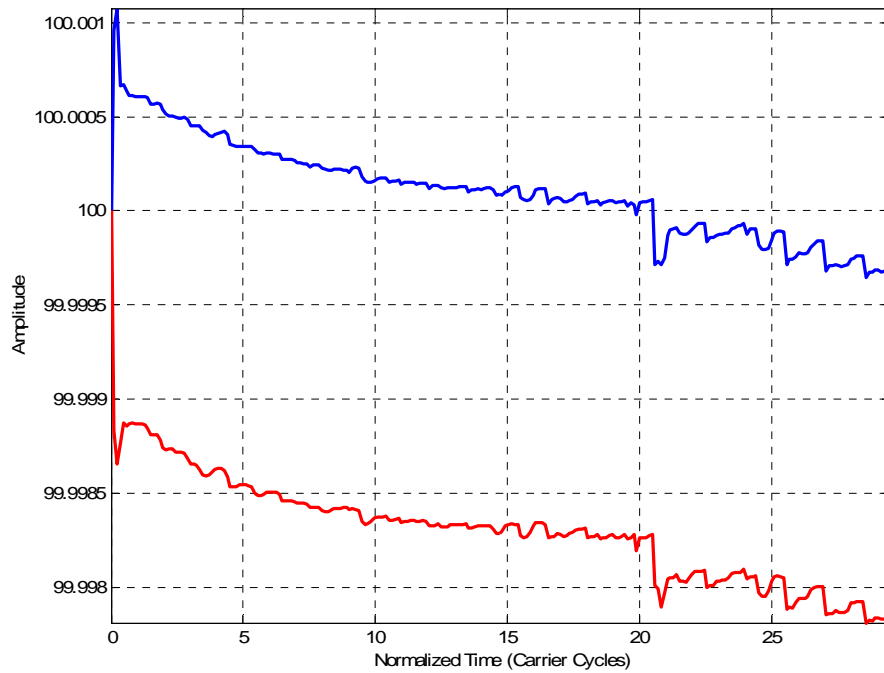


Figure 5-7 Amplitude tracking; simulated target has an amplitude equal to sea clutter.

5.2.3 Summary

In summary the ability to resolve and detect co-located and co-channel signals is a function of both the initial phases and the relative bandwidths or variances of the phase modulation processes. In the worst case when the targets' initial phases and transition matrices are the same, the signals can not be distinguished from each other. On the other hand when the targets have 90 degree initial phase difference (Quadrature) and the phase processes have substantially different transition matrices, the signals can be readily separated. Between these two extremes the targets observability and separability vary continuously. If the phase process' modulations are nearly equal, then they are separable only if the initial phases are in near Quadrature. If the initial phases are nearly the same, then the signals are separable only if the phase process modulation is substantially different.

Another factor affecting the separability is the amplitude difference between co-channel signals. It is difficult for the proposed method to detect all signals when there is a significant amplitude difference. From the simulation results the effective working range of this method is 10 dB deltas [120]. This limitation still allows detection where previously detection was ruled out.

5.3 Pre-whitened RJMCMC for DOA Estimation

Markov Chain Monte Carlo (MCMC) methods are first introduced to solve the high-dimensional integral in Bayesian inference. RJMCMC [93] and Birth-Death MCMC [94], are two mature algorithms developed to extend the model estimation from the specified parameter space (certain order) to variable parameter spaces (unknown order). The

RJMCMC has been fully developed for model determination and classification in white or even spatially colored Gaussian noise with known covariance matrix. Larocque and Reilly [95][96] modify the RJMCMC method from the white noise case into that of colored Gaussian noise with unknown covariance matrix to jointly estimate DOA and source number in time domain. More detailed theories and applications about RJMCMC can be found in [97][98].

In this section we investigate the application of the MCMC method to slowly moving targets detection in background noise dominated by sea clutter. It has been reported that sea clutter is the main noise component in ocean radar detection and there have been many efforts to define the sea clutter's dynamic model as described in section 5.1. During the study we find that the RJMCMC method can not be directly applied to the estimation of DOA and target number in HF radar. We then adopt a fast and simple adaptive filter prior to RJMCMC to suppress or pre-whiten the energy of sea clutter, particularly the first order Bragg lines, and reduce their major contributions to the background noise.

The GSC-extended preprocessing for sea clutter suppression is introduced in section 5.3.1. In section 5.3.2 we describe the basic principle and application of RJMCMC for target detection. In section 5.3.3 the performance is studied based on real sea clutter data with both real and simulated ship targets. The conclusion is summarized in section 5.3.4.

5.3.1 GSC-extended Pre-whitening

We consider a complex data vector $\mathbf{y}(t)$ received by a uniform linear array of M sensors at time t where the distance between two adjunct sensors is d . Every element of the data vector $\mathbf{y}(t)$ is composed of impinging plane wave signals from k non-coherent sinusoidal targets whose distinct center frequencies are $\omega_1, \omega_2, \dots, \omega_k$ and DOAs are

$\theta_1, \theta_2, \dots, \theta_k$ embedded in background compound noise. Then the general model for the received vector at time t is

$$\mathbf{y}(t) = \mathbf{A}\mathbf{s}(t) + \mathbf{v}(t) \quad (5.20)$$

where the k -by-1 vector $\mathbf{s}(t)$ contains the amplitude and center frequency information of the k targets. We assume that the background noise $\mathbf{v}(t)$ is mainly composed of the sea clutter (First order Bragg lines and high order spectrum). The M -by- k matrix $\mathbf{A} = [\mathbf{a}(\theta_1) \ \mathbf{a}(\theta_2) \ \dots \ \mathbf{a}(\theta_k)]$ contains the steering vectors of the impinging sources with the i^{th} column as

$$\mathbf{a}(\theta_i) = \begin{bmatrix} 1 & e^{-j2\pi\frac{d\sin(\theta_i)}{\lambda}} & \dots & e^{-j2\pi(M-1)\frac{d\sin(\theta_i)}{\lambda}} \end{bmatrix}^T$$

where λ is the radar carrier wavelength and $[\cdot]^T$ is the matrix transpose.

The sea clutter pre-whitening is achieved by an extended GSC-like procedure [111]. By this means the clutter components among different sensors are temporally and spatially whitened while keeping intact the relative target signal phases among sensors. The conventional GSC method is introduced by Griffiths and Jim [125] as an adaptive beamformer, which turns the linearly constrained minimum-variance algorithm into an unconstrained optimization problem while the constraint is explicitly embedded in the architecture.

The original array signal matrix $\mathbf{Y}_{M \times N}$ with M sensors and N time is passed through a blocking matrix \mathbf{B} (spatial filtering) to remove the desired ship signal. The blocking matrix output allows approximation of the sea clutter and noise in two dimensions (space and time). The output of the blocking matrix is then the reference interference signal to be used in the adaptive noise canceling filter. In conventional GSC the signal components

are formed by a linear combiner as in the upper part of the diagram in Figure 5-8 (a), and thereafter we lose the sensor domain. In order to take advantage of array information we extend the GSC upper branch by applying adaptive filters directly to the sensor outputs as in Figure 5-8 (b) instead of their combination. By this means the noise components among different sensors are temporally and spatially whitened while keeping intact the relative target signal phases among sensors. The final output of the processed array signal matrix is

$$\mathbf{Y}'_{M \times N} = \left[\mathbf{I} - \mathbf{R}^H \mathbf{B} (\mathbf{B}^H \mathbf{R} \mathbf{B})^{-1} \mathbf{B}^H \right] \mathbf{Y}_{M \times N} \quad (5.21)$$

where \mathbf{R} is the array covariance matrix of $\mathbf{Y}_{m \times N}$.

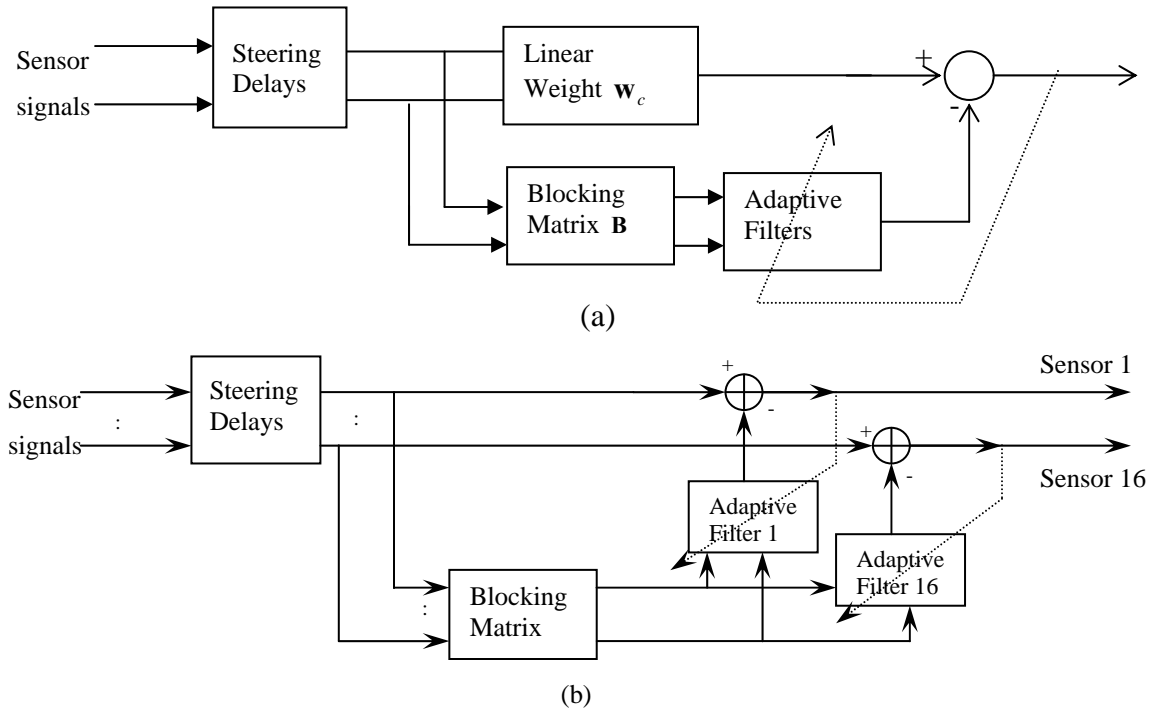


Figure 5-8 (a) The structure of generalized sidelobe canceller. (b) Extended GSC.

5.3.2 Reversible Jump MCMC

Through the preprocessing the power of the first order Bragg line is suppressed and the resulting noise from the adaptive canceller is similar to the spatially colored Gaussian noise with the distribution as $N(0, \Sigma)$, where Σ is the arbitrary covariance matrix. Then we adopt RJMCMC to jointly estimate the DOAs and sources' number. The total likelihood function of all the data is

$$f(\mathbf{Y} | \boldsymbol{\theta}(k), \mathbf{S}, \Sigma, k) = \frac{1}{\pi^{MN} |\Sigma|^N} \exp\left\{-\sum_t (\mathbf{y}(t) - \mathbf{A}(\boldsymbol{\theta}, k)\mathbf{s}(t))^H \Sigma^{-1} (\mathbf{y}(t) - \mathbf{A}(\boldsymbol{\theta}, k)\mathbf{s}(t))\right\} \quad (5.22)$$

where \mathbf{Y} and \mathbf{S} are the total received data set and corresponding sources' waveforms respectively. Under the assumption of uncorrelated noise and signal, an orthonormal matrix [126] is defined to divide the whole space into signal subspace and noise subspace as $\mathbf{U}(\boldsymbol{\theta}, k) = [\mathbf{U}_s(\boldsymbol{\theta}, k) \quad \mathbf{U}_n(\boldsymbol{\theta}, k)]$, and separate projections of the sampled data onto those subspaces are respectively

$$\mathbf{z}_s(n) = \mathbf{U}_s^H(\boldsymbol{\theta}, k)\mathbf{y}(n); \quad \mathbf{z}_n(n) = \mathbf{U}_n^H(\boldsymbol{\theta}, k)\mathbf{y}(n)$$

Thereby the unknown covariance matrix Σ is partitioned into two additive covariance matrices, one each for the $\mathbf{z}_s(n)$ and $\mathbf{z}_n(n)$. Let matrix \mathbf{W} be the covariance matrix for $\mathbf{z}_n(n)$. The desired *a posteriori* distribution based on Bayes' theorem is

$$f(\mathbf{S}, \boldsymbol{\theta}, k, \mathbf{W}^{-1} | \mathbf{z}_n, \mathbf{z}_s) = \frac{f(\mathbf{z}_n, \mathbf{z}_s | \mathbf{S}, \boldsymbol{\theta}, k, \mathbf{W}^{-1})f(\mathbf{S} | \boldsymbol{\theta}, k, \mathbf{W}^{-1})f(\mathbf{W}^{-1} | \boldsymbol{\theta}, k)f(\boldsymbol{\theta} | k)f(k)}{f(\mathbf{z}_n, \mathbf{z}_s)} \quad (5.23)$$

where the initial distributions [95] are

$$\begin{aligned}
f(\mathbf{S} | \boldsymbol{\theta}, k, \mathbf{W}^{-1}) &\sim \prod_{n=1}^N N(0, \alpha^2 \mathbf{I}_k); \\
f(\mathbf{W}^{-1} | \boldsymbol{\theta}, k) &\sim |\mathbf{W}^{-1}|^{-(M-k)}; \\
f(\boldsymbol{\theta} | k) &\sim U[0, 2\pi]^k; \\
f(k) &\sim \frac{\gamma^k e^{-\gamma}}{k!}
\end{aligned} \tag{5.24}$$

The marginal distribution $f(\mathbf{z}_n, \mathbf{z}_v)$ is unrelated with the model specification. Every DOA is independently sampled from the uniform distribution over the range $[0, 2\pi]$. \mathbf{I}_k is the identity matrix of size k . The hyperparameters α^2 and γ are adjustable but their chosen values will affect the convergence of MCMC method. Larocque and Reilly [95] simplify the *a posteriori*, and the final expression is

$$f(k, \boldsymbol{\theta} | \mathbf{z}_n) \sim \frac{\pi^{0.5(M-k)(M-k-1)} \prod_{i=1}^{M-k} \Gamma(N-i+1) |\mathbf{N}\mathbf{W}|^{-N}}{(2\pi/\gamma)^k k! (\alpha^2)^{kN}} \tag{5.25}$$

where Γ is the Gamma distribution. From maximum *a posteriori*, the basic criterion of Bayesian inference, the point $\{k, \boldsymbol{\theta}\}$ that maximizes the *a posteriori* distribution is the best estimation.

The Metropolis-Hasting (MH) algorithm [127] is one of the approaches for construction of the Markov chain from which the parameters are sampled to guarantee the convergence to a stationary distribution $f(\boldsymbol{\theta})$ as

$$\lim_{N \rightarrow \infty} f^N(\boldsymbol{\theta}^{i+1} | \boldsymbol{\theta}^i) f(\boldsymbol{\theta}^0) = f(\boldsymbol{\theta}) \tag{5.26}$$

where $f(\boldsymbol{\theta}^{i+1} | \boldsymbol{\theta}^i)$ is the transition kernel from step i to step $i+1$, and $f(\boldsymbol{\theta}^0)$ is the initial distribution, which compose the Markov chain. From equation (5.25) the parameter $\boldsymbol{\theta}$ in our problem is simply the DOA vector, and the initial distribution is assumed to be the final stationary distribution.

The complexity of MH algorithm is largely decreased, but the convergence is not clearly stable because of the random sampling from the initial distribution. RJMCMC applies three kinds of moving to realize the “reversible jumping” among variable parameter spaces to search for the global optimum. The probabilities for choosing birth moving b_k , death moving d_k and update moving n_k are

$$\begin{aligned} b_k &= 0.5 \min \left\{ \frac{f(k+1)}{f(k)}, 1 \right\}; \\ d_k &= 0.5 \min \left\{ \frac{f(k)}{f(k+1)}, 1 \right\}; \\ n_k &= 1 - b_k - d_k; \end{aligned} \quad (5.27)$$

As target number k increases, d_k increases and b_k decreases. The acceptance probability determines the moving option in each step is accepted or not, which is calculated as the rate of transitions using the i^{th} step's original value θ^i instead of the updated candidate θ' relative to those from θ' to θ^i . For instance, the acceptance probability for step i is

$$r_i = \frac{f(\theta', k' | z_n) f(\theta^i, k^i | \theta', k')}{f(\theta^i, k^i | z_n) f(\theta', k' | \theta^i, k^i)}.$$

5.3.3 Simulation and Experiments

In this section we demonstrate experimental results for both real and simulated target detection in sea clutter using our preprocessed RJMCMC. The radar utilizes a floodlight transmitting antenna and uniform linear array with 16 sensors as receiver. The data set is collected using 3.2MHz carrier frequency and the dwell time is about 164s. The surveillance range is 51.5~200 km with azimuth coverage of 120 degrees.

Experiment One: In this experiment we show the estimation results for a real ship embedded in true sea clutter echo which is known to exist at range 126 km with Doppler of -0.0832 Hz and DOA of -50 degrees. The beamformed Doppler spectrum for range 126 km and DOA of -50 degree is shown in Figure 5-9. The Parameters are chosen as $\alpha^2 = 4000$ and $\gamma = 3$. The RJMCMC without preprocessing fails whereas the result with preprocessing is shown in Figure 5-10. The total iterations are 10000 with the first 5000 iterations as burn-in. The DOA resolution for the result is 1 degree. We find that the algorithm detects the correct number of targets and estimates the DOA as -50 degree.

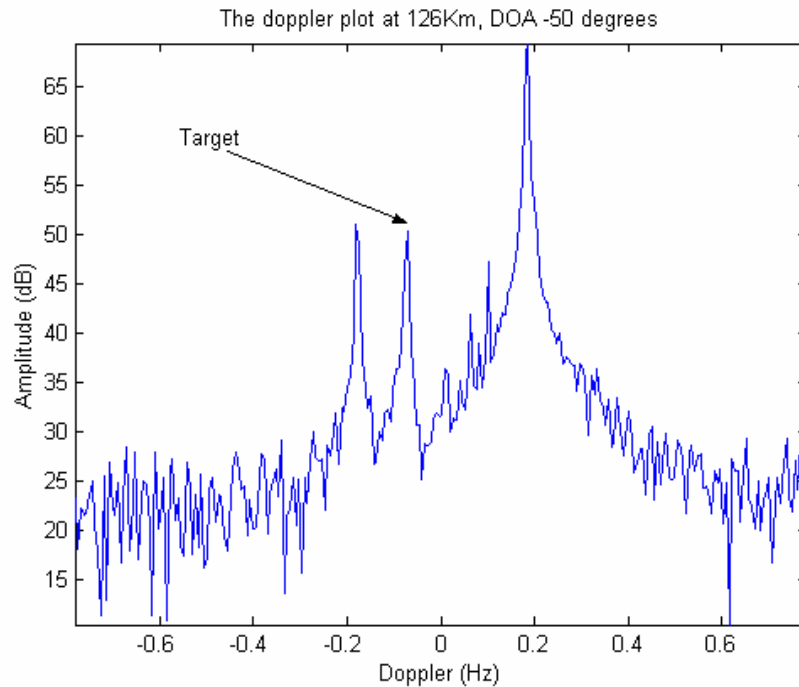


Figure 5-9 Beamformed Doppler spectrum at DOA -50 and range 126 km.

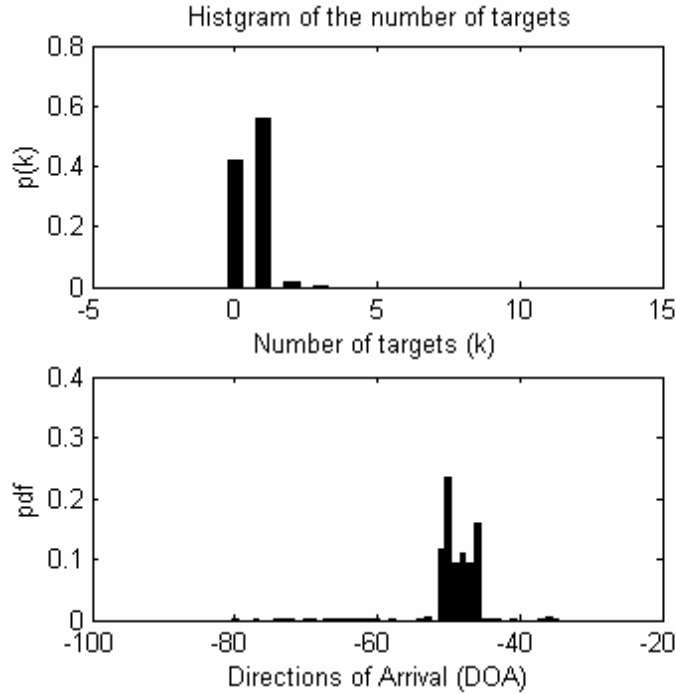


Figure 5-10 Histograms of the number of targets and DOA for 10000 iterations for real data with sea clutter after pre-whitening. Estimated DOA is -50 degrees.

Experiment Two: In this experiment, we simulate a target at range 180 km, DOA 30 degrees, and Doppler frequency 0.4028 Hz with sea clutter background. We define SNR as the power of the signal to the power of the largest Bragg line. The traditional beamforming method (Figure 5-11) is presented to compare with the RJMCMC at different SNR values.

We also study the robustness of the estimated DOA under variable SNRs by running the program 50 times. The MSE versus SNR is shown in Table 5-1 for RJMCMC. The MSE increases with the decrease of SNR as expected. We must point out that we only consider the first 5000 iterations after burn-in in order to lower the computation intensity. More iteration will increase the robustness and estimation accuracy.

Table 5-1 The Mean Squared Error of the estimated DOA versus SNR for RJMCMC

Test Case	1	2	3	4	5
SNR(dB)	16.3	12.4	8.8	-0.21	-2.7
MSE(degree ²)	2.2	2.05	8.1	9.03	15.1

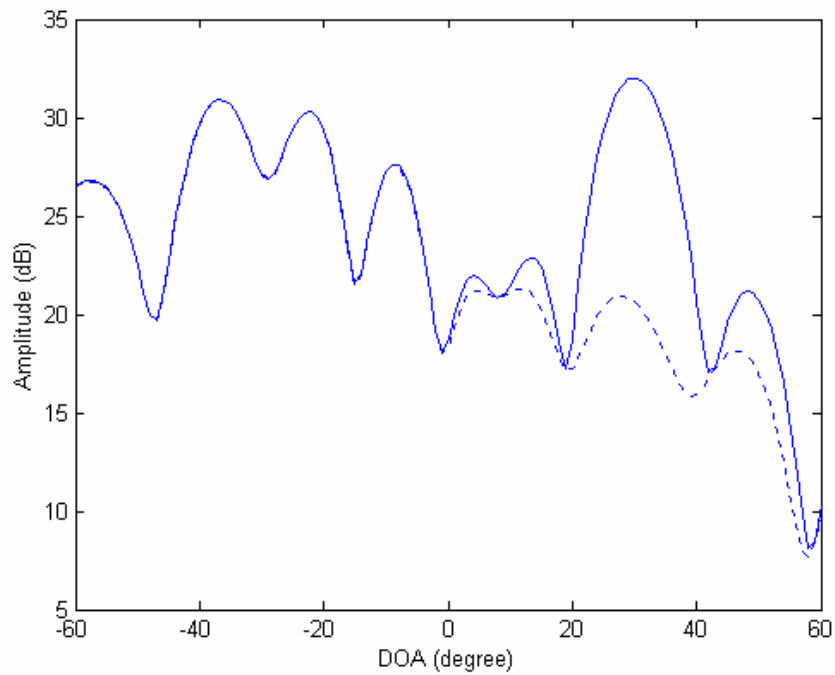


Figure 5-11 Traditional beamforming spatial spectrums with 16.2651 dB (solid trace) and 12.3547 dB (dashed trace).

Figure 5-11 shows the results from the traditional beamforming method. When SNR=16.2651 dB, we can obtain the correct DOA while the method fails when SNR=12.3547 dB or lower. However the RJMCMC clearly converges to the global maximum at this 12.3547 SNR.

5.3.4 Discussion and Summary

In this section we propose the pre-whitened RJMCMC to jointly estimate the DOAs and target number. The first and higher order sea clutter spectrums are strong enough to result in the failure of the original RJMCMC. An extended GSC-like procedure is used to suppress the Bragg lines to make the original RJMCMC applicable to the detection in sea clutter. Experimental results show that the pre-processed RJMCMC can extract targets from clutter background in HF radar. In conclusion the distinctive properties of RJMCMC methods are:

- (1) RJMCMC is non-sensitive to initial values, but sensitive to hyperparameters;
- (2) RJMCMC is computationally intensive;
- (3) RJMCMC is able to converge to the optimal resolution for a data set that is small compared with information theoretic criteria;
- (4) RJMCMC has potential to converge to local optimal solution due to its random sampling;
- (5) RJMCMC has low SNR threshold compared with traditional beamforming.

5.4 Particle Filter

The original sequential Monte Carlo (SMC) method [99][100][109] based on the sequential important sampling has been introduced and developed since the 1950s, but its application is limited by the computation complexity and the degeneration problem. The inclusion of the resampling step, in addition to much improved computational speeds, makes the SMC method more practical and attracts lots of research interests in both

theoretical and applicable aspects [105][106][107][108]. Particle filtering is a numerical approach that recursively computes the relevant probability distributions through important sampling, which approximates the probability distributions with discrete random measurements.

5.4.1 Basic Principle of the Particle Filter

The posterior distribution of interest for the state model can be written as a recursive formula to update $p(\mathbf{x}_{l:t+1} | \mathbf{y}_{l:t+1})$ from $p(\mathbf{x}_{l:t} | \mathbf{y}_{l:t})$

$$p(\mathbf{x}_{l:t+1} | \mathbf{y}_{l:t+1}) = p(\mathbf{x}_{l:t} | \mathbf{y}_{l:t}) \frac{p(\mathbf{y}_{t+1} | \mathbf{x}_{t+1})p(\mathbf{x}_{t+1} | \mathbf{x}_t)}{p(\mathbf{y}_{t+1} | \mathbf{y}_t)} \quad (5.28)$$

In fact the equation (5.28) is not practical. Firstly in most cases it is impossible to generate samples directly from the posterior distribution $p(\mathbf{x}_{l:t} | \mathbf{y}_{l:t})$. Secondly computing $p(\mathbf{y}_{t+1} | \mathbf{y}_t)$ requires the evaluation of a complex, multi-dimensional integral. The important sampling procedure is incorporated to avoid these problems. The idea is to generate particles $\{\mathbf{x}_{t+1}^{(j)}\}$ from an appropriate important function $q(\mathbf{x}_{l:t+1} | \mathbf{y}_{l:t+1})$ and then estimate the corresponding normalized important weights $\{w_{t+1}^{(j)}\}$ as

$$w_{t+1}^{(j)} = \frac{p(\mathbf{x}_{l:t+1}^{(j)} | \mathbf{y}_{l:t+1}^{(j)}) / q(\mathbf{x}_{l:t+1}^{(j)} | \mathbf{y}_{l:t+1}^{(j)})}{\sum_{j=1}^N p(\mathbf{x}_{l:t+1}^{(j)} | \mathbf{y}_{l:t+1}^{(j)}) / q(\mathbf{x}_{l:t+1}^{(j)} | \mathbf{y}_{l:t+1}^{(j)})} \quad j = 1, 2, \dots, N \quad (5.29)$$

The equation (5.29) can be rewritten as the recursive formation to satisfy the sequential computation. Therefore the posterior distribution can be discretely approximated by N weighted particles from the important function as

$$\hat{p}_N(\mathbf{x}_{l:t+1} | \mathbf{y}_{l:t+1}) = \sum_{j=1}^N w_{l:t+1}^{(j)} \delta(\mathbf{x}_{l:t+1} - \mathbf{x}_{l:t+1}^{(j)}) \quad (5.30)$$

where $\delta(\bullet)$ is the Dirac delta function. So the performance of the particle filtering is closely related with the selection of the important function. The closer the important function to that posterior distribution, the better the approximation is. Generally the prior important function [112] and the optimal important function [100] (minimizes the variance of important weights) are two frequently used ones.

If the important function is poorly selected (Normally it is hard to find a good important function especially in high-dimensional space), one serious problem exists in the particle filtering that most particles are assigned with negligible weights after certain updating iterations, which called degeneracy phenomenon. In other words the variance of the important weights increases over time. The weight degeneracy of the algorithm can be measured by the effective sample size N_{eff} [101], which is estimated at time step t as

$$N_{eff} = \frac{1}{\sum_{j=1}^N (w_t^{(j)})^2} \quad (5.31)$$

It is clear that $N_{eff} = 1$ when $w_t^{(j)} = 1$ and $w_t^{(j)} = 0$ ($j \neq j'$) while $N_{eff} = N$ when $w_t^{(j)} = \frac{1}{N}$ for all particles. So this parameter is a scalar between 1 and N and the smaller the parameter, the severer the degeneracy degree.

Resampling is a scheme that eliminates the trajectories with weak normalized important weights and multiplies (enhances) trajectories with strong important weights. To degrade the weight degeneracy in sequential important sampling (SIS) filter, the new particle set is resampled from the approximate discrete posterior distribution $\hat{P}_N(\mathbf{x}_{1:t+1} | \mathbf{y}_{1:t+1})$ if N_{eff} is below a preset threshold at time $t+1$ and then the associated

weights are renewed as $\frac{1}{N}$ uniformly. However the resampling step is applied in each iteration for the sampling important resampling filter [102].

Although the resampling step reduces the effect of degeneracy, it introduces the problem of loss of diversity called sample impoverishment in that the resultant sample set contains many repeated points because the samples are drawn from a discrete approximation rather than a continuous posterior distribution in the resampling stage. It is severe in the case where process noise in state dynamics is very small. Some techniques have been proposed to solve the problem of sample impoverishment such as the resample-move algorithm (involving MCMC step) [103] and regularized step included algorithm [104].

Based on its non-strict suitable condition, particle filtering has been widely utilized in many research regions such as communication, tracking, detection, biology, economics and so on [105][106][109]. In this section, we concentrate on applying this methodology for target detection in radar system.

5.4.2 Target Detection in White Noise

5.4.2.1 Theorem Part

Larocque presented the modified particle filter to sequentially detect the number of targets and the corresponding DOAs in [107][108]. The new form of RJMCMC with four jumping moves has been presented to enhance the original resampling's performance in the loss of statistical diversity. The basic principle has been shown in the following part.

Assuming a complex echo data vector \mathbf{y} , received by a uniform linear array of M sensors at time t where the distance between two adjunct sensors is d . Every element of

the data vector \mathbf{y}_t is composed of impinging plane wave signals from k non-coherent sinusoidal targets whose distinct center frequencies are $\omega_1, \omega_2, \dots, \omega_k$ and DOAs are $\boldsymbol{\theta} = \{\theta_1, \theta_2, \dots, \theta_k\}$ embedded in background compound noise. Then the received vector at time t can be written as

$$\mathbf{y}_t = \mathbf{A}(\boldsymbol{\theta}_t) \mathbf{s}_t + \mathbf{u}_t \quad (5.32)$$

where the k -by-1 vector \mathbf{s}_t involves the amplitude and center frequency information of the k targets that is assumed as IID Gaussian distribution with zero mean and σ_s^2 variance. The background noise \mathbf{u}_t is IID Gaussian distribution with zero mean and σ_u^2 variance as $N(0, \sigma_u^2 \mathbf{I}_{k(t)})$. The M -by- k matrix $\mathbf{A}(\boldsymbol{\theta}_t) = [\mathbf{a}(\theta_1(t)) \quad \mathbf{a}(\theta_2(t)) \quad \dots \quad \mathbf{a}(\theta_k(t))]$ contains the steering vectors of the impinging sources with the i^{th} column as

$$\mathbf{a}(\theta_i(t)) = \begin{bmatrix} 1 & e^{-j2\pi \frac{d \sin(\theta_i(t))}{\lambda}} & \dots & e^{-j2\pi(M-1) \frac{d \sin(\theta_i(t))}{\lambda}} \end{bmatrix}^T$$

where λ is the radar carrier wavelength, $[\cdot]^T$ is vector transpose.

Moreover the interested DOAs $\boldsymbol{\theta} = \{\theta_1, \theta_2, \dots, \theta_k\}$ are first-order AR model as $\boldsymbol{\theta}_t = \boldsymbol{\theta}_{t-1} + \mathbf{v}_t$ with $\mathbf{v}_t \sim N(0, \sigma_v^2 \mathbf{I}_{k_t})$. The target number k_t is assumed to change less than two in each step and described as first-order AR model too.

$$k_t = k_{t-1} + \varepsilon_t$$

where the three-state random variable ε_t has the following stochastic function

$$\begin{aligned} P(\varepsilon_t = 1) &= 0.5h \\ P(\varepsilon_t = -1) &= 0.5h \\ P(\varepsilon_t = 0) &= 1 - h \end{aligned}$$

where h is the hyperparameter between 0 and 1.

Using Bayesian theorem, the posterior distribution with all the parameters

$\mathbf{x}_{1:t} = \{\boldsymbol{\theta}_{1:t}, \mathbf{s}_{1:t}, \sigma_{u(1:t)}^2, \sigma_{v(1:t)}^2, k_{1:t}\}$ is given as

$$\begin{aligned}
 p(\boldsymbol{\theta}_{1:t}, \mathbf{s}_{1:t}, \sigma_{u(1:t)}^2, \sigma_{v(1:t)}^2, k_{1:t} | \mathbf{y}_{1:t}) &= \frac{p(\mathbf{y}_{1:t} | \boldsymbol{\theta}_{1:t}, \mathbf{s}_{1:t}, \sigma_{u(1:t)}^2, \sigma_{v(1:t)}^2, k_{1:t}) p(\boldsymbol{\theta}_{1:t}, \mathbf{s}_{1:t}, \sigma_{u(1:t)}^2, \sigma_{v(1:t)}^2, k_{1:t})}{p(\mathbf{y}_{1:t})} \\
 &\propto p(\mathbf{y}_{1:t} | \boldsymbol{\theta}_{1:t}, \mathbf{s}_{1:t}, \sigma_{u(1:t)}^2, \sigma_{v(1:t)}^2, k_{1:t}) p(\mathbf{s}_{1:t} | \boldsymbol{\theta}_{1:t}, \sigma_{u(1:t)}^2, k_{1:t}) \\
 &\quad \times p(\boldsymbol{\theta}_{1:t} | \sigma_{v(1:t)}^2, k_{1:t}) p(\sigma_{u(1:t)}^2) p(\sigma_{v(1:t)}^2) p(k_{1:t})
 \end{aligned} \tag{5.33}$$

where $p(\mathbf{y}_{1:t})$ is one constant at each step through the high-dimensional integral. The prior distribution can be expanded based on the parameter correlation. The corresponding likelihood function and prior distributions are defined as

$$\begin{aligned}
 p(\mathbf{y}_{1:t} | \boldsymbol{\theta}_{1:t}, \mathbf{s}_{1:t}, \sigma_{u(1:t)}^2, \sigma_{v(1:t)}^2, k_{1:t}) &= \prod_{i=1}^t N(\mathbf{A}(\boldsymbol{\theta}_i) \mathbf{s}_i, \sigma_{u(i)}^2 \mathbf{I}_M) \\
 p(\mathbf{s}_{1:t} | \boldsymbol{\theta}_{1:t}, \sigma_{u(1:t)}^2, k_{1:t}) &= \prod_{i=1}^t N(0, \delta^2 \sigma_{u(i)}^2 (\mathbf{A}'(\boldsymbol{\theta}_i) \mathbf{A}(\boldsymbol{\theta}_i))^{-1}) \\
 p(\boldsymbol{\theta}_{1:t} | \sigma_{v(1:t)}^2, k_{1:t}) &= \prod_{i=1}^t N(\boldsymbol{\theta}_{i-1}, \sigma_{v(i)}^2 \mathbf{I}_{k_i}) \\
 p(\sigma_{u(1:t)}^2) &= \prod_{i=1}^t IG(\nu_1, \gamma_1) \\
 p(\sigma_{v(1:t)}^2) &= \prod_{i=1}^t IG(0.5\nu_0, 0.5\gamma_0) \\
 p(k_{1:t}) &= \prod_{i=1}^t P(\varepsilon(i))
 \end{aligned} \tag{5.34}$$

where $IG(\nu, \gamma)$ is inverse Gamma distribution with PDF:

$$p(x) \propto \begin{cases} x^{-(\nu+1)} e^{-\gamma/x} & \text{when } x \geq 0 \\ 0 & \text{others} \end{cases}$$

The prior distribution for parameter $\mathbf{s}_{1:t}$ is the maximum entropy prior with hyperparameter δ^2 expressing the signal to noise ratio. Those nuisance parameters

$\{\mathbf{s}_{1:t}, \sigma_{u(1:t)}^2, \sigma_{v(1:t)}^2\}$ can be integrated out from the posterior distribution through maximum

entropy method in each iteration and then the simplified posterior distribution is only associated with the DOAs and target number as

$$\begin{aligned}
p(\boldsymbol{\theta}_{1:t}, k_{1:t} | \mathbf{y}_{1:t}) &\propto \prod_{i=1}^t \frac{1}{\sigma_u^{2M} (1 + \delta^2)^{k_i}} \exp \left[\frac{-1}{\sigma_u^2} \mathbf{y}_i' P_A^\perp(\boldsymbol{\theta}_i) \mathbf{y}_i \right] \\
&\times \prod_{i=1}^t \frac{1}{(\sigma_v^2 \cdot 2\pi)^{0.5k_i}} \exp \left[\frac{-1}{2\sigma_v^2} (\boldsymbol{\theta}_i - \boldsymbol{\theta}_{i-1})' (\boldsymbol{\theta}_i - \boldsymbol{\theta}_{i-1}) \right] \\
&\times \sigma_{v(i)}^{2(-0.5\nu_0-1)} \exp \left[-\frac{\gamma_0}{2\sigma_{v(i)}^2} \right] \times \sigma_{u(i)}^{2(-\nu_1-1)} \exp \left[-\frac{\gamma_1}{\sigma_{u(i)}^2} \right] \times \prod_{i=1}^t p(k_i | k_{i-1})
\end{aligned} \tag{5.35}$$

where

$$\begin{aligned}
\mathbf{s}_i &= \left(A'(\boldsymbol{\theta}_i) A(\boldsymbol{\theta}_i) (1 + \delta^{-2}) \right)^{-1} A'(\boldsymbol{\theta}_i) \mathbf{y}_i \\
P_A^\perp(\boldsymbol{\theta}_i) &= \mathbf{I}_M - \frac{A(\boldsymbol{\theta}_i) (A'(\boldsymbol{\theta}_i) A(\boldsymbol{\theta}_i))^{-1} A'(\boldsymbol{\theta}_i)}{1 + \delta^{-2}} \\
\sigma_{v(i)}^2 &= \frac{0.5\gamma_0 + 0.5 \sum_{i=1}^t (\boldsymbol{\theta}_i - \boldsymbol{\theta}_{i-1})' (\boldsymbol{\theta}_i - \boldsymbol{\theta}_{i-1})}{0.5\nu_0 + 0.5 \sum_{i=1}^t k_i + 1} \\
\sigma_{u(i)}^2 &= \frac{\gamma_1 + \sum_{i=1}^t (\mathbf{y}_i' P_A^\perp(\boldsymbol{\theta}_i) \mathbf{y}_i)}{\nu_1 + Mt + 1}
\end{aligned} \tag{5.36}$$

It is hard to sample directly from the posterior distribution because the simplified posterior distribution is not standard form and known only up to a normalizing constant.

As the important sampling paradigm, the particles $\{j=1, \dots, N\}$ in each step are drawn from the optimal important distribution $q(\boldsymbol{\theta}_{1:t}, k_{1:t} | \mathbf{y}_{1:t})$ which is expanded as

$$q(\boldsymbol{\theta}_{1:t}, k_{1:t} | \mathbf{y}_{1:t}) = q(\boldsymbol{\theta}_{1:t-1}, k_{1:t-1} | \mathbf{y}_{1:t-1}) q(\boldsymbol{\theta}_t, k_t | \boldsymbol{\theta}_{1:t-1}, k_{1:t-1}, \mathbf{y}_{1:t}).$$

The conditional distribution $q(\boldsymbol{\theta}_t, k_t | \boldsymbol{\theta}_{1:t-1}, k_{1:t-1}, \mathbf{y}_{1:t})$ is not easy to evaluate here and from equation $\boldsymbol{\theta}_t = \boldsymbol{\theta}_{t-1} + \mathbf{v}_t$ and the first order Taylor expansion of Eq (5.32) we have:

$$\begin{aligned}
\mathbf{y}_t &= A(\boldsymbol{\theta}_t)\mathbf{s}_t + \mathbf{u}_t \\
&\approx A(\boldsymbol{\theta}_{t-1})\mathbf{s}_t + \frac{\partial A(\boldsymbol{\theta}_t)\mathbf{s}_t}{\partial \boldsymbol{\theta}_t} \times (\boldsymbol{\theta}_t - \boldsymbol{\theta}_{t-1}) + \mathbf{u}_t \\
&\approx A(\boldsymbol{\theta}_{t-1})\mathbf{s}_{t-1} + \frac{\partial A(\boldsymbol{\theta}_{t-1})\mathbf{s}_{t-1}}{\partial \boldsymbol{\theta}_{t-1}} \times (\boldsymbol{\theta}_t - \boldsymbol{\theta}_{t-1}) + \mathbf{u}_t
\end{aligned} \tag{5.37}$$

the suboptimal approximation can be formulated into Gaussian distribution as

$$q(\boldsymbol{\theta}_t^{(j)} | \boldsymbol{\theta}_{t-1}^{(j)}, \mathbf{y}_t) \sim N(m_t^{(j)}, \Sigma_t^{(j)}) \tag{5.38}$$

where

$$\begin{aligned}
m_t^{(j)} &= \Sigma_t^{(j)} \left(\sigma_{v(t)}^{-2(j)} \mathbf{I}_{k_t(j)} \boldsymbol{\theta}_{t-1}^{(j)} + G'(\sigma_{u(t)}^{-2(j)} \mathbf{I}_M) (\mathbf{y}_t - A(\boldsymbol{\theta}_{t-1}^{(j)})\mathbf{s}_{t-1}^{(j)} + G\boldsymbol{\theta}_{t-1}^{(j)}) \right) \\
\Sigma_t^{(j)} &= \left(\sigma_{v(t)}^{-2(j)} \mathbf{I}_{k_t(j)} + G'(\sigma_{u(t)}^{-2(j)} \mathbf{I}_M) G \right)^{-1} \\
G &= \frac{\partial A(\boldsymbol{\theta}_{t-1}^{(j)})\mathbf{s}_{t-1}^{(j)}}{\partial \boldsymbol{\theta}_{t-1}^{(j)}}
\end{aligned} \tag{5.39}$$

Then the recursive expression of the important weights $w_t^{(j)}$ can be written as

$$\begin{aligned}
w_t^{(j)} &= w_{t-1}^{(j)} \frac{p(\mathbf{y}_t | \boldsymbol{\theta}_t^{(j)}, k_t^{(j)}) p(\boldsymbol{\theta}_t^{(j)}, k_t^{(j)} | \boldsymbol{\theta}_{t-1}^{(j)}, k_{t-1}^{(j)})}{q(\boldsymbol{\theta}_t^{(j)}, k_t^{(j)} | \boldsymbol{\theta}_{t-1}^{(j)}, k_{t-1}^{(j)}, \mathbf{y}_t)} \\
&= w_{t-1}^{(j)} \frac{p(\mathbf{y}_t | \boldsymbol{\theta}_t^{(j)}, k_t^{(j)}) p(\boldsymbol{\theta}_t^{(j)} | \boldsymbol{\theta}_{t-1}^{(j)}, k_{t-1}^{(j)}) p(k_t^{(j)} | k_{t-1}^{(j)})}{q(\boldsymbol{\theta}_t^{(j)} | \boldsymbol{\theta}_{t-1}^{(j)}, \mathbf{y}_t) p(k_t^{(j)} | k_{t-1}^{(j)})} \\
&= w_{t-1}^{(j)} \frac{p(\mathbf{y}_t | \boldsymbol{\theta}_t^{(j)}, k_t^{(j)}) p(\boldsymbol{\theta}_t^{(j)} | \boldsymbol{\theta}_{t-1}^{(j)}, k_{t-1}^{(j)})}{q(\boldsymbol{\theta}_t^{(j)} | \boldsymbol{\theta}_{t-1}^{(j)}, \mathbf{y}_t)}
\end{aligned} \tag{5.40}$$

So the particles $\{j = 1, \dots, N\}$ sampled from (5.38) are applied into the first two equations of (5.34) to evaluate $p(\mathbf{y}_t | \boldsymbol{\theta}_t^{(j)}, k_t^{(j)})$ and $p(\boldsymbol{\theta}_t^{(j)} | \boldsymbol{\theta}_{t-1}^{(j)}, k_{t-1}^{(j)})$ in order to updating the important weights as (5.40).

Reversible Jump MCMC has been involved to enhance diversity amongst the particles and facilitate detection of model order. Reversible Jump MCMC is one approach to sample directly from the joint distribution over all model orders of interest. The samples are chosen from a set of proposal distributions, which are randomly

accepted according to an acceptance ratio that ensures reversibility, and therefore the invariance of the Markov chain with respect to the desired posterior distribution.

Several moves have been included in the jumping process. The birth move, a new target proposed randomly, is chosen with probability p_{birth} ; the death move, one existed target proposed to be removed, is chosen with probability p_{death} ; the split move, one existed target proposed to be split into two targets, is chosen with probability p_{split} ; the merge move, two nearby targets proposed to be merged into one, is chosen with probability p_{merge} ; the update move, the existing target parameters proposed to be updated, is chosen with probability $1 - p_{birth} - p_{death} - p_{split} - p_{merge}$. In each move, the candidate sample $\{\theta_t^{*(j)}, k_t^{*(j)}\}$ can be accepted to replace the original sample $\{\theta_t^{(j)}, k_t^{(j)}\}$ with acceptance ratio as

$$\alpha((\theta_t^{*(j)}, k_t^{*(j)}), (\theta_t^{(j)}, k_t^{(j)})) = \min \left\{ \frac{p(\theta_t^{*(j)}, k_t^{*(j)} | \mathbf{y}_t) q_m(\theta_t^{*(j)}, k_t^{*(j)} | \mathbf{y}_t)}{p(\theta_t^{(j)}, k_t^{(j)} | \mathbf{y}_t) q_m(\theta_t^{(j)}, k_t^{(j)} | \mathbf{y}_t)} \cdot \left| \frac{\partial \theta_t^{*(j)}}{\partial \theta_t^{(j)}} \right|, 1 \right\} \quad (5.41)$$

In summary, the basic steps for target detection using particle filter are:

Step 1: At $t=1$, initialize the target number $k_1^{(j)}$ and DOAs $\theta_1^{(j)}$. Then the weights $w_1^{(j)}$ are estimated from $w_1^{(j)} = \frac{p(\theta_1^{(j)}, k_1^{(j)} | \mathbf{y}_1)}{q(\theta_1^{(j)}, k_1^{(j)} | \mathbf{y}_1)}$ for $j=1, \dots, N$. Update $t = t + 1$.

Step 2: When $t > 1$, update the mean and variance of the important distribution and draw N particles from this Gaussian distribution (5.38) with new parameters. For each particle, update the amplitude and variances $\{s_t^{(j)}, \sigma_{u(t)}^{2(j)}, \sigma_{v(t)}^{2(j)}\}$ from (5.36) and then calculate its important weight using (5.40). Normalize all weights by dividing with their sum $\sum_{j=1}^N w_t^{(j)}$.

Step 3: At resampling step, sample a vector of index l with distribution as $P(l(r) = j) = w_t^{(j)}$. Resample the particles with the index vector $\boldsymbol{\theta}_t^{(j)} = \boldsymbol{\theta}_t^{(l(j))}$. And reassign all the weights to

$$w_t^{(j)} = \frac{1}{N}.$$

Step 4: In RJMCMC step, for each particle sample the pointing parameter β from uniform distribution between 0 and 1.

If $\beta < p_{birth}$, Do birth move

Produce $\{\boldsymbol{\theta}_t^{*(j)}, k_t^{*(j)}\}$ where $\boldsymbol{\theta}_t^{*(j)} = \{\boldsymbol{\theta}_t^{(j)}, \theta_{new}^{(j)}\}$, $k_t^{*(j)} = k_t^{(j)} + 1$

if $\alpha((\boldsymbol{\theta}_t^{*(j)}, k_t^{*(j)}), (\boldsymbol{\theta}_t^{(j)}, k_t^{(j)})) > \chi \sim U(0,1)$

$$\{\boldsymbol{\theta}_t^{(j)}, k_t^{(j)}\} = \{\boldsymbol{\theta}_t^{*(j)}, k_t^{*(j)}\}$$

end

elseif $\beta < p_{birth} + p_{death}$, Do death move

Produce $\{\boldsymbol{\theta}_t^{*(j)}, k_t^{*(j)}\}$ where $\boldsymbol{\theta}^{*(j)} = \{\theta_1^{(j)}, \dots, \theta_{i-1}^{(j)}, \theta_{i+1}^{(j)}, \dots, \theta_k^{(j)}\}$, $k_t^{*(j)} = k_t^{(j)} - 1$

($\theta_i^{(j)}$ is any existed DOA for particle j at step t)

if $\alpha((\boldsymbol{\theta}_t^{*(j)}, k_t^{*(j)}), (\boldsymbol{\theta}_t^{(j)}, k_t^{(j)})) > \chi \sim U(0,1)$

$$\{\boldsymbol{\theta}_t^{(j)}, k_t^{(j)}\} = \{\boldsymbol{\theta}_t^{*(j)}, k_t^{*(j)}\}$$

End

elseif $\beta < p_{birth} + p_{death} + p_{split}$, Do split move

Produce $\{\boldsymbol{\theta}_t^{*(j)}, k_t^{*(j)}\}$ where $\boldsymbol{\theta}^{*(j)} = \{\theta_1^{(j)}, \dots, \theta_{i-1}^{(j)}, \theta_i^{(j)} - \Delta\theta, \theta_i^{(j)} + \Delta\theta, \theta_{i+1}^{(j)}, \dots, \theta_k^{(j)}\}$,

$k_t^{*(j)} = k_t^{(j)} + 1$. ($\theta_i^{(j)}$ is any existed DOA for particle j at step t)

if $\alpha((\boldsymbol{\theta}_t^{*(j)}, k_t^{*(j)}), (\boldsymbol{\theta}_t^{(j)}, k_t^{(j)})) > \chi \sim U(0,1)$

$$\{\boldsymbol{\theta}_t^{(j)}, k_t^{(j)}\} = \{\boldsymbol{\theta}_t^{*(j)}, k_t^{*(j)}\}$$

end

elseif $\beta < p_{birth} + p_{death} + p_{split} + p_{merge}$, Do merge move

Produce $\{\boldsymbol{\theta}_t^{*(j)}, k_t^{*(j)}\}$ where $\boldsymbol{\theta}^{*(j)} = \{\theta_1^{(j)}, \dots, \theta_{i-1}^{(j)}, 0.5 \times \theta_i^{(j)} + 0.5 \times \theta_{i+1}^{(j)}, \dots, \theta_k^{(j)}\}$,

$k_t^{*(j)} = k_t^{(j)} - 1$. ($\theta_t^{(j)}$ is any existed DOA for particle j at step t)

if $\alpha((\theta_t^{*(j)}, k_t^{*(j)}), (\theta_t^{(j)}, k_t^{(j)})) > \chi \sim U(0,1)$

$$\{\theta_t^{(j)}, k_t^{(j)}\} = \{\theta_t^{*(j)}, k_t^{*(j)}\}$$

end

else, Do update move.

Produce $\{\theta_t^{*(j)}, k_t^{*(j)}\}$ where $\theta_t^{*(j)} \sim N(\theta_t^{(j)}, \sigma_{v(t)}^2 \mathbf{I}_{k_t^{(j)}})$, $k_t^{*(j)} = k_t^{(j)}$.

if $\alpha((\theta_t^{*(j)}, k_t^{*(j)}), (\theta_t^{(j)}, k_t^{(j)})) > \chi \sim U(0,1)$

$$\{\theta_t^{(j)}, k_t^{(j)}\} = \{\theta_t^{*(j)}, k_t^{*(j)}\}$$

end

$t = t + 1$, go back Step 2.

5.4.2.2 Simulation Part

Simulation One

The data is assumed to be received from uniform linear array with 16 sensors. The data length is 100 and one simulated target is injected in the white noise. The simulated parameters are $\sigma_v^2 = 1 \text{deg}^2$, $\sigma_u^2 = 0.15$, $\theta_0 = [70^\circ]$ and $\sigma_s^2 = 0.0707$. The initial parameters for Particle Filter are $\delta^2 = 100$, $\nu_0 = \nu_1 = \gamma_0 = \gamma_1 = 0$, $k_0 = 1$ and $N = 300$. The DOA estimation is shown in Figure 5-12. It can be observed that after around 30 scans, the result converges to the correct DOA of 70 degrees.

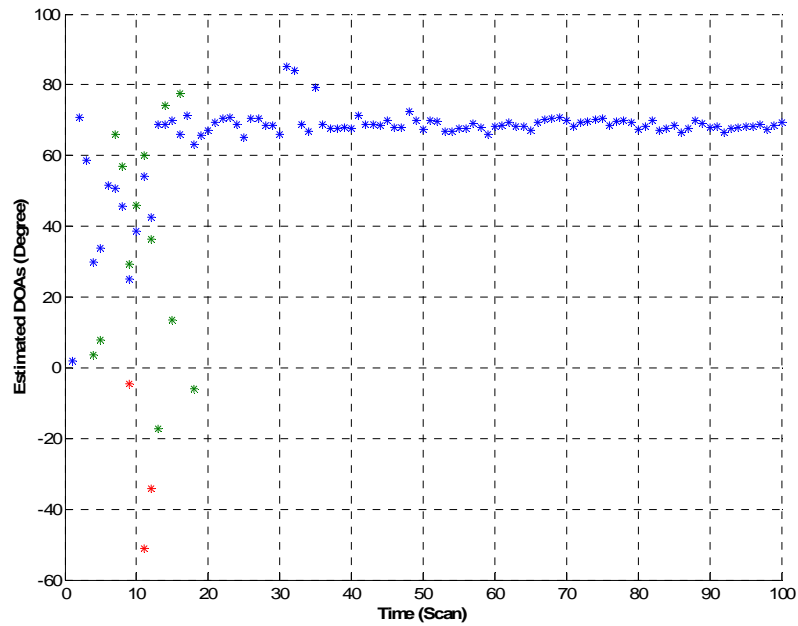


Figure 5-12 Particle Filter Estimated DOAs for simulation one

Simulation Two

The parameters are similar as those in simulation one except that there are two targets in the first 50 scans and one target disappears after that. The simulated parameters are $\sigma_v^2 = 5 \text{ deg}^2$, $\sigma_u^2 = 0.15$, $\theta_0 = [70^\circ, -40^\circ]$. The simulation results are shown in Figure 5-13. It is observed that the particle filter updates the targets status every scan based on the coming signal echoes but which is not the case in the RJMCMC as discussed in Section 5.3.

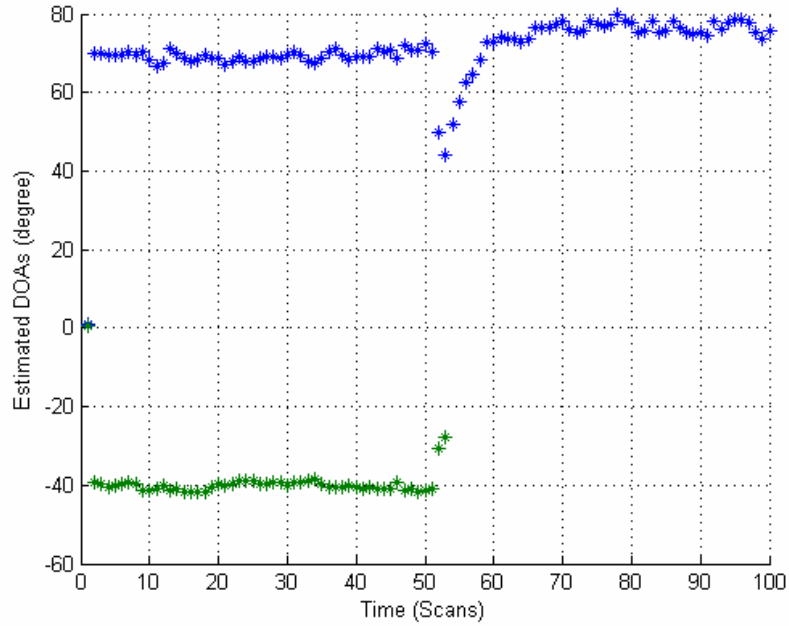


Figure 5-13 Particle Filter Estimated DOAs for simulation two

5.4.3 Further Discussion

In HF radar, the background noise is white noise plus sea clutter. The sea clutter is the dominant noise power contributor in near range. So the original received signal model will be modified to the following formula:

$$\mathbf{y}_t = \mathbf{A}(\boldsymbol{\theta}_t)\mathbf{s}_t + \mathbf{c}_t$$

where \mathbf{c}_t is the sea clutter component and can be approximately written as second-order linear prediction:

$$\mathbf{c}_t = \boldsymbol{\mu}_1\mathbf{c}_{t-1} + \boldsymbol{\mu}_2\mathbf{c}_{t-2} + \mathbf{z}_t$$

where parameters $\boldsymbol{\mu}_1$ and $\boldsymbol{\mu}_2$ are assumed to be constant and \mathbf{z}_t is white noise with zero mean and $\sigma_{z(t)}^2$ variance. Here the sea clutter is approximately presented by second order AR model based on its two Bragg lines characteristics.

The posterior distribution with all the parameters $\{\boldsymbol{\theta}_{1:t}, \mathbf{s}_{1:t}, \mathbf{c}_{1:t}, \sigma_{v(1:t)}^2, \sigma_{z(1:t)}^2, k_{1:t}\}$ is given as

$$\begin{aligned}
 & p(\boldsymbol{\theta}_{1:t}, \mathbf{s}_{1:t}, \mathbf{c}_{1:t}, \sigma_{v(1:t)}^2, \sigma_{z(1:t)}^2, k_{1:t} | \mathbf{y}_{1:t}) \\
 &= \frac{p(\mathbf{y}_{1:t} | \boldsymbol{\theta}_{1:t}, \mathbf{s}_{1:t}, \mathbf{c}_{1:t}, \sigma_{v(1:t)}^2, \sigma_{z(1:t)}^2, k_{1:t}) p(\boldsymbol{\theta}_{1:t}, \mathbf{s}_{1:t}, \mathbf{c}_{1:t}, \sigma_{v(1:t)}^2, \sigma_{z(1:t)}^2, k_{1:t})}{p(\mathbf{y}_{1:t})} \\
 &\propto p(\mathbf{y}_{1:t} | \boldsymbol{\theta}_{1:t}, \mathbf{s}_{1:t}, \mathbf{c}_{1:t}, \sigma_{v(1:t)}^2, \sigma_{z(1:t)}^2, k_{1:t}) p(\mathbf{s}_{1:t} | \boldsymbol{\theta}_{1:t}, \mathbf{c}_{1:t}, k_{1:t}) \\
 &\quad \times p(\boldsymbol{\theta}_{1:t} | \sigma_{v(1:t)}^2, k_{1:t}) p(\mathbf{c}_{1:t} | \sigma_{z(1:t)}^2) p(\sigma_{v(1:t)}^2) p(\sigma_{z(1:t)}^2) p(k_{1:t})
 \end{aligned}$$

How to simplify the posterior distribution based on DOA and target number and build up the important function is the open problem for further study.

Chapter 6 – Conclusions and Future Research

6.1 Summary

We have presented several novel signal processing techniques in this thesis to improve the performance of the existing HFSWR system. Impulsive noise, an additive external interference in HF radar, has been studied for effective excision solution in Chapter two. The legacy method implemented in the system uses an FIR notch filter to bandstop the Doppler spectrum of the radar signal around the Bragg line frequency. The pulse whose average power along the range dimension is larger than a given threshold is judged to be impulsive noise. The corrupted pulses are reset to zero. This method has several issues, notch filter design, preset threshold selection and pulse blanking, which make the optimal solution impossible. The traditional linear prediction method and its modifications, forward-backward prediction and block prediction, are presented in section 2.2. With a modified version of linear prediction, the impulsive noise excision algorithm can detect and reconstruct the spike pulses smoothly even with unpredicted frequency distortion in

sea clutter. The performance of the novel impulse noise excision is verified in section 2.2.5 by the simulated weak target extraction from real impulsive noise overwhelmed sea clutter background. The theoretical performance analyses of those linear predictions are presented in section 2.3, and these confirm that the modified methods have less minimum error variance compared with that of the traditional predictors. In section 2.4 the signal property mapping has been applied to the estimated covariance matrix to further improve the prediction performance. A novel interpretation of the performance is presented based on the Gaussian multiple mixture model.

Although a beampattern would be free of high sidelobes when computed using the true covariance matrix, sidelobes are definitely an issue when any sample covariance matrix is applied; this is the topic studied in Chapter three. We present the snapshot model for a uniform linear array and then discuss the conventional adaptive beamforming processing technique in section 3.2. In the following section we review several existing sidelobe control approaches: diagonal loading, penalty function and PT-DQC. Moreover the new approach OT-DQC is proposed to provide a feasible and optimal solution. All the sidelobe control approaches are unified with a second order cone formation in section 3.3, which can be solved efficiently via primal-dual interior point methods. In section 3.4 it is shown that solution from OT-DQC is not sensitive to the weight factor and OT-DQC has the best sidelobe control performance with little SINR scarified.

The target detection in range-Doppler map is accomplished through CFAR technique in HFSWR system. In Chapter four we propose a hybrid CFAR method to improve the detection performance in mixed environments include domination by either external noise sea clutter or ionospheric clutter. The basic CFAR detection theory is overviewed

in section 4.2. Two switching schemes, Standard deviation and information-based clustering, have been introduced to discriminate the non-homogeneous from the homogeneous in section 4.3. Since Sea clutter distributes along range while the ionosphere clutter generally distributes along Doppler, an adaptive window is proposed and integrated into the switching CFAR. The performances analysis for CA-CFAR and OS-CFAR in homogeneous and non-homogenous background are presented in section 4.4. As shown in section 4.5, with the real experiments the new adaptive switching CFAR produces approximately 14 % more associated plots at the output of the tracker than that of the original OS-CFAR. At the same time a much lower false alarm rate has been achieved by AS-CFAR compared to the original CFAR.

The common detection method in HF radar is based on Doppler processing with a long dwell time to discriminate the ships from the background sea clutter and noise in the frequency spectrum. In Chapter five, the time-domain characteristics of the received signal are investigated to improve the probability of the target detection in HF radar. In section 5.1 several potential effective sea clutter models are reviewed. In section 5.2 we propose a detector based on extended Kalman filter to resolve co-located targets with similar Doppler frequencies. The separability ability is a function of the initial phases, the relative bandwidths or variances of the phase modulation processes and amplitude difference. The pre-whitened RJMCMC method is applied for target DOA estimation in section 5.3. The pre-processing is an extended generalized sidelobe canceller-like procedure. The approach's effectiveness is verified through simulation results.

6.2 Suggestion for Future Work

We hope the research topics addressed in this thesis contribute to better detection and tracking of targets in ocean surveillance surroundings. At the same time we suggest the following directions as future research works:

- The optimization of adaptive switching CFAR on switching threshold and window parameters is worth further studying and testing with real data.
- Particle filtering, a sub-optimal solution for nonlinear and non-Gaussian problems, is worth studying for the potential application to target detection in sea clutter situation.

Bibliography

- [1] L. Sevgi, A. M. Ponsford, H. C. Chan, "An Integrated Maritime Surveillance System Based on High-Frequency Surface-wave Radars, 1.Theoretical Background and Numerical Simulations", IEEE Antennas and Propagation Magazine, Vol. 43, No. 4, pp. 28-43, 2001.
- [2] A. M. Ponsford, L. Sevgi and H. C. Chan, "An integrated maritime surveillance system based on high-frequency surface-wave radars. 2. Operational status and system performance", IEEE Antennas and Propagation Magazine , Vol. 43, No. 5, pp. 52-63, Oct. 2001.
- [3] J. Barnum, "Ship detection with high resolution skywave radar", IEEE J. of Oceanic Eng., Vol. 11, pp 196-209, 1986.
- [4] B. J. Lipa, D.E. Barrick, J. Isaacson and P.M. Lilleboe, "CODAR wave measurements from a North Sea semisubmersible", IEEE Journal of Ocean Engineering, Vol.15, pp: 119-125, April, 1990.
- [5] J. R. Wait, "Theory of HF Ground Wave Backscatter from Sea Waves", J. Geophys. Res. 71, 4839-4842, 1966.
- [6] D. E. Barrick, "First-order Theory and Analysis of MF/HF/VHF Scatter from the Sea", IEEE Trans. on Antennas and Propagation, AP20, pp.2-10, 1972.
- [7] D. E. Barrick, J. M. Headrick, R. W. Bogle and D. D. Crobie, "Sea Backscatter at HF: Interpretation and Utilization of the Echo", Proc. IEEE, 62, pp: 673-680, 1974.
- [8] D. E. Barrick, "HF Radio Oceanography-A Review", Boundary-Layer Meteorology, Vol. 13, pp. 23-43, 1978.
- [9] E. D. R. Shearman, "Radio Science and Oceanography", Radio Science, Vol. 18, No. 3, pp 299-320, May, 1983.
- [10] J.R. Barnum and E.E. Simpson, "Over-the-Horizon Radar Sensitivity Enhancement by Impulsive Noise Excision", IEEE National Radar Conference, pp: 252-256, 1997.
- [11] F. Yu, Y. Shen, and Y. Liu, "An Effective Method of Anti-impulsive-disturbance for Ship-target Detection in HF Radar", CIE International Conference on Radar, Proceedings, pp. 372-375, 2001.
- [12] J.-J. Hsue and A.E. Yagle, "Similarities and Differences between One-Sided and Two-Sided Linear Prediction," IEEE Trans. Sig. Proc. 43(1), 345-349, January 1995.

- [13] J. Makhoul, "Linear prediction: A tutorial review," Proc. IEEE, Vol 63, pp: 561-580, 1975.
- [14] J-J. Hsue and A. E. Yagle, "Fast algorithms for close-to-Toeplitz-plus-Hankel systems and two-sided linear prediction," IEEE Trans. Signal Processing, Vol. 41, No.7, pp 2349-2361, 1993.
- [15] B. D. Van Veen and K. M. Buckley, "Beamforming: A Versatile Approach to Spatial Filtering", IEEE ASSP Magazine, pp. 4-24, 1988.
- [16] R. L. Kirilin and W. J. Done, "Covariance Analysis for Seismic Signal Processing", Society of Exploration Geophysicists, Tulsa, OK, 1999.
- [17] H. Krim and M. Viberg, "Two Decades of Array Signal Processing Research", IEEE ASSP Magazine, pp: 67-94, July 1996.
- [18] R. B. Ertel, P. Cardieri, K. Sowerby, T. Rappaport and J. Reed, "Overview of Spatial Channel Models for Antenna Array Communication Systems", IEEE Personal Communication, pp: 10-22, 1998.
- [19] S. Haykin, *Array Signal Processing*, Prentice-Hall, Inc., Englewood Cliffs, NJ, 1985.
- [20] C. A. Speirs, D. T. Hughes, J. L. Mather and A. R. Green, "Practical Considerations of Using Adaptive Beamforming with Real Sonar Data", Seventh International Conference on Electronic Engineering in Oceanography, pp: 23-25, 1997.
- [21] A. M. Haimovich and Y. Bar-Ness, "An Eigenanalysis Interference Canceller", IEEE Trans. on Signal Processing, Vol. 39, No. 1, pp: 76-84, 1991.
- [22] J. Capon, "High-Resolution Frequency-Wave number Spectrum Analysis", Proc. IEEE, Vol. 57, No. 8, pp: 2408-2418, 1969.
- [23] B. D. Carlson, "Covariance Matrix Estimation Errors and Diagonal Loading in Adaptive Arrays", IEEE Trans. on Aerospace and Electronic Systems, Vol. 24, No. 4, pp: 397-401, July 1988.
- [24] K. Gerlach, "Adaptive Array Transient Sidelobe Levels and Remedies", IEEE Trans. on Aerospace and Electronic Systems, Vol. 26, No. 3, pp: 560 -568, May 1990.
- [25] L. B. Fertig, "Statistical Performance of the MVDR Beamformer in the Presence of Diagonal Loading", Proc. of IEEE Sensor Array and Multichannel Signal Processing Workshop, pp: 77-81, 2000.

- [26] Z. Tian, K. L. Bell and H. L. Van Trees, "A Recursive Least Square Implementation for LCMP Beamforming under Quadratic Constraint", *IEEE Trans. on Signal Processing*, Vol. 49, No. 6, pp: 1138-1145, 2001.
- [27] H. L. Van Trees, *Optimum Array Processing, Part IV of Detection, Estimation, and Modulation Theory*, John Wiley & Sons, New York, 2002.
- [28] D. T. Hughes and J. G. McWhirter, "Sidelobe Control in Adaptive Beamforming Using a Penalty Function", *Proc. of International Symposium on Signal Processing and its Applications*, pp. 200-203, Gold Coast, Australia, 1996.
- [29] D. T. Hughes and J. G. McWhirter, "Using the Penalty Function Method to Cope With Mainbeam Jammers", *3rd International Conference on Signal Processing*, Vol. 1, pp. 461-464, Oct 1996.
- [30] J. G. McWhirter, Data-domain Penalty Function Algorithm for Stabilised Adaptive Beamforming, *IEE Proc. of Radar, Sonar and Navigation*, Vol. 147, No.6, pp. 265-269, 2000.
- [31] D. H. Brandwood and J. D. Baker, "Stabilization of Adaptive Array Patterns Using Signal Space Projection", *Sixth International Conference on Antennas and Propagation*, Vol. 1, pp. 289 -294, Apr 1989.
- [32] G. M. Herbert, "A New Projection Based Algorithm for Low Sidelobe Pattern Synthesis in Adaptive Arrays", *Conference on Radar 97*, pp. 396-400, Oct 1997.
- [33] Y. Luo, T. Zhang and S. Zhang, "A novel Algorithm for Adaptive Beamforming Based on Projection Transformation", *Proc. of 2001 CIE International Conference on Radar*, pp. 552 -556, 2001.
- [34] J. Liu, A. B. Gershman, Z. Luo and K. M. Wong, "Adaptive Beamforming with Sidelobe Control Using Second-order Cone Programming", *Proc. of IEEE Sensor Array and Multichannel Signal Processing Workshop*, Rosslyn, VA, pp. 461-464, 2002.
- [35] J. F. Sturm, "Using SeDuMi 1.02, a MATLAB Toolbox for Optimization over Symmetric Cones", *Optim. Meth. Software*, Vol. 11-12, pp. 625-653, 1999.
- [36] M. S. Lobo, L. Vandenberghe, S. Boyd and H. Lebret, "Application of Second-order Cone Programming", *Linear Algebra and Applications*, pp. 193-228, Nov. 1998.
- [37] S. Boyd and L. Vandenberghe, *Convex Optimization*, Cambridge University Press, 2003.
- [38] M. Skolnik, *Radar Handbook*, McGraw-Hill publishing company, 1990.

- [39] V.G., Hansen, "Constant false alarm rate processing in search radars", Proceedings of the IEEE International Radar Conference, pp: 325-332, 1973, London.
- [40] E.K. Al-Hussaini, "Performance of the greater-of and censored greater-of detectors in multiple target environments", IEE Proceedings F, Vol. 135, Issue: 3, pp: 193-198, 1988.
- [41] S.D. Himonas, "Adaptive censored greatest-of CFAR detection", IEE Proceedings F, Vol: 139, Issue: 3, pp: 247-255, 1992.
- [42] M. Barkat, S. D. Himonas and P. K. Varshney, "CFAR detection for multiple target situations", IEE Proceedings, F. Vol: 136, Issue 5, 1989.
- [43] G.V. Trunk, "Range resolution of targets using automatic detectors", IEEE Trans on Aerospace and Electronic Systems, Vol.14, pp 750-755, 1978.
- [44] H. Goldman and I. Bar-David, "Analysis and application of the excision CFAR detector", Radar and Signal Processing, IEE Proceedings F, Vol: 135, Issue.6, pp: 563-575, Dec. 1988.
- [45] E. Conte, M. Longo and M. Lops, "Analysis of the excision CFAR detector in the presence of fluctuating targets," IEE Proceedings F, Vol: 136, Issue: 6, pp: 290 -292, 1989.
- [46] H., Rohling, "Radar CFAR thresholding in clutter and multiple target situations", IEEE trans on Aerospace and Electronic Systems, Vol. 19, pp: 608-621, 1983.
- [47] H., Rohling, "New CFAR processor based on ordered statistic", International Radar Conference of IEEE, pp: 38-42, 1984, Paris.
- [48] M. Shor and N. Levanon, "Performances of order statistics CFAR", Aerospace and Electronic Systems, IEEE Transactions on, Vol. 27 Issue: 2, pp:214-224, 1991.
- [49] C.-M. Cho and M. Barkat, "Moving ordered statistics CFAR detection for nonhomogeneous backgrounds", IEE Proceedings F, Vol: 140 Issue: 5, pp: 284 -290, 1993.
- [50] M. B. EL Mashade, "Analysis of the censored-mean level CFAR processor in multiple target and nonuniform clutter" Radar, Sonar and Navigation, IEE Proceedings, Vol: 142 Issue: 5, pp: 259 -266, 1995.
- [51] B. C. Armstrong and H.D.Griffiths, "False alarm control in spiky clutter by multi-burst range-Doppler processing", International Radar Conference, pp: 94-97, 1992.
- [52] M. D. E. Turley, "Hybrid CFAR techniques for HF radar", Radar 97, pp: 36-40, 1997.

- [53] Y. Qiang, L. Jiao and Z. Bao, "An approach to detecting the targets of aircraft and ship together by over-the-horizon radar", Radar, 2001 CIE International Conference on, pp: 95-99, 2001.
- [54] X. Meng, J. Guan and Y. He, "Performance analysis of the weighted window CFAR algorithms", Proceedings of the IEEE international Radar Conference, pp: 354-357, 2003.
- [55] R. Nitzberg, "Clutter map CFAR analysis", IEEE trans on Aerospace and Electronic Systems, Vol. 22, pp: 419-421, 1986.
- [56] M. Lops and M. Orsini, "Scan-by-scan averaging CFAR", Radar, Sonar and Navigation, IEE Proceedings, Vol. 136 Issue: 6, pp: 249-254, 1989.
- [57] E. Conte and M. Lops, "Clutter-map CFAR detection for range-spread Targets in non-Gaussian clutter. Part I: system Design", IEEE Trans on Aerospace and Electronic Systems, Vol. 33, pp: 432-443, 1997.
- [58] E. Conte, M. Di Bisceglie and M. Lops, "Clutter-map CFAR detection for range-spread Targets in non-Gaussian clutter. Part II: performance assessment", IEEE Trans on Aerospace and Electronic Systems, Vol. 33, pp: 444-455, 1997.
- [59] T. Shan, R. Tao, Y. Wang and S. Zhou, "Performance of order statistic clutter map CFAR", 2002 6th International Conference on Signal Processing, Vol. 2, pp: 1572 -1575, 2002.
- [60] E. Conte, M. Lops and A.M. Tulino, "Hybrid procedure for CFAR in non-Gaussian clutter", Radar, Sonar and Navigation, IEE Proceedings, Vol. 144 Issue: 6, pp: 361 -369, 1997.
- [61] R. Nitzberg, "Composite CFAR techniques", Signals, Systems and Computers, Conference Record of The Twenty-Seventh Asilomar Conference on, pp: 1133 -1137, 1993.
- [62] P. B. Kenneth and R. A. David, *Model selection and inference-a practical information-theoretic approach*, Springer, 1998.
- [63] L. P. Heck and K. C. Chou, "Gaussian mixture model classifiers for machine monitoring", Proceedings ICASSP, V. 6, pp: 133-136, 1994.
- [64] G. Schwarz, "Estimating the dimension of a model", Annals of statistics 6, 461-464, 1978.
- [65] C. Fraley and A. E. Raftery, "How many clusters? Which clustering method? Answers via model-based cluster analysis", The Computer Journal, Vol. 41, No. 8, 578-588, 1998.

[66] J. T. Tou, and R. C. Gonzalez, *Pattern Recognition Principles*, Addison-Wesley, New York, 1974.

[67] Z. Peyton and J. R. Peebles, *Probability, random variables and random signal principles*, 4th edition, McGraw-Hill, New York, 2000.

[68] P. P. Gandhi and S. A. Kassam, "Analysis of CFAR Processors in nonhomogeneous background", *IEEE Trans on Aerospace and Electronic Systems*, Vol. 24, pp: 427-445, 1988.

[69] M. L. Skolnik, *Introduction to Radar Systems*, second edition, McGraw-Hill, 1982.

[70] H. Goldstein, "Sea Echo" in *Propagation of Short Radio Waves*, D. E. Kerr, ed. MCGraw-Hill, pp. 481-527, 1951.

[71] G. V. Trunk and S. F. George, "Detection of Targets in Non-Gaussian Sea Clutter", *IEEE Trans. on Aerospace and Electronic Systems*, AES-6, pp. 620-628, 1970.

[72] F. A. Fay, J. Clarke and R. S. Peters, "Weibull distribution applied to sea clutter", *Radar'77*, IEE Conf. Vol. 155, pp: 101-103, 1977.

[73] E. Jakeman and P. N. Pusey, "A Model for Non-Rayleigh Sea Echo", *IEEE Trans. on Ant. and Prop.*, Vol. 24, No. 6, pp. 806-814, 1976.

[74] K. D. Ward, "Compound Representation of High Resolution Sea Clutter", *Electronic Letters*, Vol. 17, pp. 561-565, 1981.

[75] S. Watts, "Radar Detection Prediction in Sea Clutter Using the Compound K-distribution Model", *IEE Proceedings F*, Vol. 132, pp. 613-620, 1985.

[76] E. Conte, M. Longo, M. Lops and S. L. Ullo, "Radar Detection of Signals with Unknown Parameters in K-Distributed Clutter", *IEE Proceedings-F*, Vol. 138, No. 2, pp. 131-138, 1991.

[77] A. M. Zoubir, "Statistical Signal Processing for Application to Over-the-Horizon Radar", *ICASSP'94*, Vol. 6, pp. 113-116, 1994.

[78] H. Leung and T. Lo, "Chaotic radar signal processing over the sea", *IEEE Journal of Oceanic Engineering*, Vol. 18, No. 3, pp. 287-295, 1993.

[79] S. Haykin and S. Puthusserypady, "Chaotic dynamics of sea clutter: an experimental study", *Proceedings of IEE conference on Radar*, pp. 75-79, 1997.

[80] S. Haykin and X. Li., "Detection of signals in chaos", *Proceedings of the IEEE*, Vol. 83, No 1, pp. 95-122, 1995.

- [81] M. Davies, "Looking for non-linearities in sea clutter", RSSP 98, Peebles, Scotland.
- [82] C. P. Unsworth, M. R. Cowper, S. McLaughlin, and B. Mulgrew, "Re-examining the nature of radar sea clutter", Radar, Sonar and Navigation, IEE Proceedings - , Vol. 149, pp. 105-114, June 2002.
- [83] S. Haykin , R. Bakker, and B. W. Currie, "Uncovering nonlinear dynamics—the case study of sea clutter", Proceedings of the IEEE, Vol. 90, No. 5, pp. 860-881, 2002.
- [84] R. H. Khan, "Ocean-Clutter Model for High-Frequency Radar", IEEE Journal of Oceanic Engineering, Vol. 16, No. 2, pp. 181-188, April 1991.
- [85] M. W. Y. Poon, R. H. Khan and S. Le-Ngoc, "A Singular Value Decomposition (SVD) Based Method for Suppressing Ocean Clutter in High Frequency Radar", IEEE Transactions on Signal Processing, Vol. 41, No. 3, pp. 1421-1425, March 1993.
- [86] K. Hickey, R. H. Khan and J. Walsh, "Parametric Estimation of Ocean Surface Currents with HF Radar", IEEE Journal of Oceanic Engineering, Vol. 20, No. 2, pp.139-144, April 1995.
- [87] R. H. Khan and J. Walsh, "Ocean Clutter Suppression for an HF Ground Wave Radar", CCECE'97, pp512-515, 1997.
- [88] D. W. Tufts and R. Kumaresan, "Estimation of Frequencies of Multiple Sinusoids: Making Linear Prediction Perform Like Maximum Likelihood", Proceedings of IEEE, Vol. 70, pp. 975-989, 1982.
- [89] C. L. Dimonte and K. S. Arun, "Tracking the Frequencies of Superimposed Time-Varying Harmonics", Proc. ICASSP'90, pp. 2539-2542, 1990.
- [90] C. Bouvier, L. Martinet, G. Favier and M. Artaud, "Simulation of Radar Sea Clutter Using Autoregressive Modeling and K-Distribution", IEEE International Radar Conference'95, pp. 425-430, 1995.
- [91] R. J. Martin and M. J. Kearney, "Remote Sea Current Sensing Using HF Radar: An autoregressive approach", IEEE Journal of Oceanic Engineering, Vol. 22, No. 1, pp. 151-155, 1997.
- [92] S. Haykin, A. H. Sayed, J. Zeidler, P. Yee and P. Wei, "Adaptive Tracking of Linear Time-Variant Systems by Extended RLS Algorithms", IEEE Transactions on Signal Processing, Vol. 45, No. 5, pp.1118-1128, May 1997.
- [93] S. Richardson and P. Green, "On Bayesian analysis of mixtures with an unknown number of components," Journal of the Royal Statistical Society, Series B, 59, pp. 731-792, 1997.

- [94] M. Stephens, "Bayesian analysis of mixture models with an unknown number of components - an alternative to reversible jump methods", *Ann. Statist.*, Vol. 28, pp. 40-74, 2000.
- [95] J.-R. Larocque and J. P. Reilly, "Reversible Jump MCMC for Joint Detection and Estimation of Directions of Arrival in Colored Noise", *IEEE Transactions on Signal Processing*, V. 50, No. 2, pp. 231-240, 2002.
- [96] M. NG, "Advances in wideband array signal processing using numerical Bayesian methods", Ph.D thesis, McMaster University, 2003.
- [97] MCMC Preprint Service, <http://www.statslab.cam.ac.uk/~mcmc/>
- [98] W. R. Gilks, S. Richardson and D. J. Spiegelhalter, *Markov Chain Monte Carlo in practice*, London: Chapman & Hall, 1996.
- [99] A. Doucet, N. de Freieas and N. Gordon, *Sequential Monte Carlo in practice*, Springer-Verlag, 2001.
- [100] A. Doucet, S. Godsill, and C. Andrieu, "On sequential Monte Carlo sampling methods for Bayesian filtering", *Statistics and Computing*, Vol.10, pp: 197-208, 2002.
- [101] A. Kong, J. S. Liu and W. H. Wong, "Sequential imputations and Bayesian missing data problems", *Journal of the American Statistical Association*, Vol. 93, pp: 1032-1044, 1998.
- [102] N. J. Gordon, D. J. Salmond, and A.F.M. Smith, "Novel approach to nonlinear/non-Gaussian Bayesian state estimation", *IEEE Proc.-F*, Vol. 140, No. 2, pp: 107-113, 1993.
- [103] W.R. Gilks and C. Berzuini, "Following a moving target—Monte Carlo inference for dynamic Bayesian models", *Journal of the Royal Statistical Society, B*. Vol. 63, pp: 127-146, 2001.
- [104] C. Musso, N. Oudjane, and F. LeGland, "Improving regularized particle filters", in *Sequential Monte Carlo Methods in Practice* (A. Doucet, N. de Freitas, and N. J. Gordon, eds.), New York: Springer, 2001.
- [105] B. Ristic, S. Arulampalam, and N. Gordon, "Beyond the Kalman filter—particle filters for tracking application", Artech House, 2004.
- [106] P. M. Djuric, J. H. Kotecha, J. Zhang, Y. Huang, T. Ghirmai, M.F. Bugallo, and J. Miguez, "Particle filtering—a review of the theory and how it can be used for solving problems in wireless communications", *IEEE Signal Processing Magazine*, pp: 19-38 , Sep 2003.

- [107] J.-R. Larocque, “Advanced Bayesian methods for array signal processing”, Ph.D thesis, McMaster University, 2001.
- [108] J.-R. Larocque, J.P. Reilly and W. Ng, “ Particle Filters for Tracking an Unknown Number of Sources”, IEEE trans on Signal Processing, Vol. 50, No 12, pp 2926-2937, 2002.
- [109] Sequential Monte Carlo Methods (Particle filter) Homepage, <http://www-sigproc.eng.cam.ac.uk/smc/>
- [110] X. Lu, R. L. Kirlin and J. Wang “Joint Estimation of Targets Number and DOA Using Reversible Jump MCMC in Sea Clutter”, Sensor Array and Multichannel Signal processing Workshop Processing, pp: 346-349, USA, 2002.
- [111] J. Wang, R. L. Kirlin, X. Lu and R. Dizaji, “Small Ship Detection with High Frequency Radar Using an Adaptive Ocean Clutter Pre-whitened Subspace Method”, *SAM 2002*.
- [112] H. Tanizaki and R.S. Mariano, “Nonlinear and non-Gaussian statespace modeling with Monte-Carlo simulations”, *Journal of Econometrics*, Vol. 83, pp 263-290, 1998.
- [113] H. Dong, C. Zong and T. Quan, “Chaotic characteristics in HF radar backscatter from the ocean surface”, *ACTA Electronic SINCA*, pp 25-28, Vol. 3, 2000.
- [114] G. Zhou, H. Dong and T. Quan, “HF ground wave radar sea clutter cancellation based on chaotic prediction”, *ICSP 7th Internal Conference on*, Vol. 3, pp. 2136-2139, 2004.
- [115] J. R. Zeidler, E. H. Satorius, D. M. Chabries and H. T. Wexler, “Adaptive Enhancement of Multiple Sinusoids in Uncorrelated Noise”, *IEEE Trans on ASSP*, Vol. 26, pp 240-254, 1978.
- [116] J-C. Lee, “Comparative performance of forward /backward and symmetric linear prediction”, *Electrics Letters*, Vol. 39, No. 2, pp 250-251, 2003.
- [117] L. L. Scharf, *Statistical Signal Processing—Detection, Estimation, and Time Series Analysis*, Addison-Wesley Publishing Company.
- [118] J. A. Cadzow, “Signal Enhancement-A Composite Property Mapping Algorithm”, *IEEE Trans on ASSP*, Vol. 36, No. 1, pp: 49-62, 1988.
- [119] K. Hermus, P. Wambacq and H. Van Hamme, “A Review of Signal Subspace Speech Enhancement and Its Application to Noise Robust Speech Recognition”, *EURASIP Journal on Advances in Signal Processing*, 2007.

- [120] B. Hedstrom, R. L. Kirlin, "Co-channel Signal Separation Using Coupled Digital Phase-locked Loops", IEEE Trans. on Communications, pp. 1373-1384, Vol. 44, No. 10, 1996.
- [121] B. Hedstrom, R. L. Kirlin, "Performance Measures for Coupled Digital Phase-Locked Loops for the Separation of Co-channel Signals", Proc. Vehic. Technol. Soc. 42nd VTS Conf., Denver, CO, pp. 279-282, May 1992.
- [122] A. Gelb, *Applied Optimal Estimation*, Cambridge, MA: MIT Press, 1974.
- [123] A. P. Sage, J. L. Melsa, *Estimation Theory with Applications to Communications and Control*, New York: McGraw-Hill, 1971.
- [124] C. L. Dimonte, K. S. Arun, "Tracking the Frequencies of Superimposed Time-Varying Harmonics", Proc. ICASSP'90, pp. 2539-2542, 1990.
- [125] L. J. Griffiths, C. W. Jim, "An Alternative Approach to Linearly Constrained Adaptive Beamforming", IEEE Trans. Antennas Propagation, Vol. 30, No. 1, pp. 27-34, 1982.
- [126] K. M. Wong, J.P. Reilly, Q. Wu, and S. Qiao, "Estimation of the direction of arrival of signals in unknown correlated noise, Part 1: The MAP approach and its implementation," IEEE Trans. Signal Processing, V.44, No. 40, pp. 2007-2017, 1992.
- [127] W. K. Hastings, "Monte Carlo sampling methods using Markov chain and its applications", Biometrika, V. 57, No. 1, pp 97-109, 1970.
- [128] D. D. Crombie, "Doppler Spectrum of Sea Echo at 13.56Mc/s", Nature, 175, pp. 681-682, 1955.
- [129] W. Du and R. L. Kirlin, "Enhancement of Covariance Matrix for Array Processing", IEEE Trans. Signal Processing, V.40, No.10, pp. 2602-2606, 1992.
- [130] A. C. Lee, "A new autoregressive method for high-performance spectrum analysis", J. Acoust. Soc. Amer. Vol 86, pp. 150-157, 1989.

VITA

Surname: Lu

Given Names: Xiaoli

Place of Birth: HeFei, People's Republic of China

Educational Institutions Attended:

Anhui Normal University	1993 to 1997
University of Victoria	2000 to 2002

Degree Awarded:

B.Sc	Anhui Normal University	1997
M.A.Sc	University of Victoria	2002

Honours and Awards:

National Sciences and Engineering Research Council of Canada (NSERC) Industrial Postgraduate Scholarship	2002 to 2004
University of Victoria President Award	2002 to 2004
Petch Research Scholarship	2004
The Charles S. Humphrey Graduate Student Award	2003

Publications

Contributions to Book

- J. Wang, R. L. Kirlin, X. Lu, "Sidelobe Control Using Optimization Methods in Adaptive Beamforming", in S. Chandran (ed.), *Adaptive Antenna Arrays*, Berlin, Germany: Springer-Verlag, June 2004.
- J. Wang, R. L. Kirlin, X. Lu, "A New DOA Estimation Method for Pulsed Doppler Radar", in *Advanced in Detection-of-Arrival Estimation*, Artech House, 2006.

Conference Publications

- R. L. Kirlin, X. Lu, J.M. Preston, A.C. Christney W.T. Collins and R.A. McConnaughey, "Quantitative Measures of Acoustic Diversity Based on Information Theory", presented in ICES Symposium, August 2001.

- X. Lu, R. L. Kirlin, J. M. Preston, A. C. Christney, W. T. Collins, and R. A. McConnaughey, “Quantitative Measures of Acoustic Diversity Based on Information Theory” presented in the ICES Symposium, June 2002.
- R. L. Kirlin, J. Wang, R. M. Dizaji, and X. Lu, “Detection of Small Targets Embedded in Ocean Clutter”, IGARSS 2002, Canada, June 2002.
- J. Wang, R. L. Kirlin, X. Lu, and R. M. Dizaji, “Small Ship Detection with High Frequency Radar Using an Adaptive Ocean Clutter Pre-whitened Subspace Method”, SAM 2002, USA.
- X. Lu, R. L. Kirlin, J. Wang, “Joint Estimation of Target Number and DOA Using Reversible Jump MCMC in Sea Clutter”, SAM 2002, USA.
- X. Lu, R. L. Kirlin, J. Wang, “Temporal Impulsive Noise Excision in the range-doppler Map of HF Radar”, International Conf. on Image Processing (ICIP) 2003, Spain.
- X. Lu, J. Wang, R. L. Kirlin, “An Optimal Threshold for Sidelobe Control in Adaptive Beamforming Using Second-Order Cone Programming”, Asilomar 2003, Pacific Cove, CA, USA.
- Y. Yu, X. Lu and X. Wang, “Image Processing in Seawater Based on Measured Modulation Transfer Function”, IEEE Pacific Rim Conference on Communications, Computers and signal processing, Canada, 2003.
- X. Lu, J. Wang, R. Dizaji, Z. Ding, A.M. Ponsford, “A Switching Constant False Alarm Rate (CFAR) Technique for High Frequency Surface Wave Radar”, CCECE 2004, Canada.
- X. Lu, J. Wang and R. L. Kirlin, “A Co-channel Signal Detector Based on Phase Tracking for Pulsed Doppler Radar”, IEEE Radar Conference 2007, USA.

Publications in Submission

- X. Lu, R. L. Kirlin, J. Wang and A. M. Ponsford, “Methods of Impulsive Noise Excision and Performance Analysis”, waiting for permission to submit to IEEE Transactions on Aerospace and Electronic Systems.
- X. Lu, J. Wang, A. M. Ponsford and R. L. Kirlin, “Impulsive Noise Excision and Performance Analysis”, IEEE Radar Conference 2010, USA.

PARTIAL COPYRIGHT LICENSE

I hereby grant the right to lend my thesis to users of the University of Victoria Library, and to make single copies only for such users or in response to a request from the Library of any other university, or similar institution, on its behalf or for one of its users. I further agree that permission for extensive copying of this thesis for scholarly purposes may be granted by me or a member of the University designated by me. It is understood that copying or publication of this thesis for financial gain shall not be allowed without my written permission.

Title of Thesis:

“Enhanced Detection of Small Targets in Ocean Clutter for High Frequency Surface Wave Radar”

Author _____

Xiaoli Lu

Dec, 2009